SYNCYTIAL MODEL OF HUMAN PLURIPOTENT STEM CELL-DERIVED CARDIOMYOCYTES FOR ELECTROPHYSIOLOGY STUDIES

by
Renjun Zhu

A dissertation submitted to Johns Hopkins University in conformity with the requirements for the degree of Doctor of Philosophy

Baltimore, Maryland
August 2017

Abstract

Human pluripotent stem cells (hPSCs) are a valuable resource for generating human cardiomyocytes and modeling human cardiac physiology *in vitro*. In this thesis, the electrophysiology of hPSC derived cardiomyocytes was studied in large populations of cells in syncytial models. It was found that heterogeneity in electrophysiology, as represented by action potential variability, is common in small clusters of hPSC-derived cardiomyocytes. A waveform-based automated algorithm was used to identify groups of cardiomyocytes based on similarity of their action potentials. It was found that, unlike in small cell clusters, action potential variability in monolayer culture was relatively low, resembling mainly a single electrophysiological phenotype. The utility of a monolayer hPSC-CM model was explored in two applications: 1) modeling the monogenic disease, type 2 Long QT syndrome (**LQT2**), using a human induced pluripotent stem cell (**hiPSC**) line carrying a hERG-A422T mutation, and 2) studying responses to cardioactive drugs using hiPSC-derived cardiomyocytes. The monolayer model with LQT2 hiPSC-derived cardiomyocytes had prolonged action potentials and an increased sensitivity to I_{Kr} block compared to that of non-disease cardiomyocytes, consistent with the expected LQT2

phenotype. The prolonged action potentials could be normalized by activation of I_{Kr} with ML-T531, a compound that delays the inactivation of the hERG channel. However, ectopic activity, such as early-afterdepolarizations (EADs), were mostly absent in LQT2 monolayers, in contrast to the frequent occurrence reported in smaller cell cultures or single cells. For drug testing, monolayers of hiPSC-derived cardiomyocytes responded to a panel of eight cardioactive drugs in a manner consistent with the mechanism of the drugs: blockers of repolarizing currents prolonged the action potentials, while blockers of depolarizing currents shortened them. At a tissue level, blockers of excitatory I_{Na} slowed propagation of action potentials. Computational modeling showed that a drug can alter the repolarization gradient, a proarrhythmia biomarker, in monolayers having a defined electrophysiological gradient.

Primary Reader: Leslie Tung, PhD

Secondary Reader: Kenneth R. Boheler, PhD

In memory of my grandmother, who was my first inspiration to pursue knowledge of the human heart.

Acknowledgements

First and foremost, I would like to sincerely thank my thesis advisor, Dr. Leslie Tung, for his continuous support throughout my Ph.D. study, for his patient guidance and immense knowledge. I also thank my thesis committee members for all the time and advice they provided throughout the years. I thank Dr. Gordon Tomaselli for the valuable discussions, especially on disease models and his clinical insights. I also thank Dr. Kenneth Boheler for his hands-on introduction of stem cell techniques to me, as well as accommodating many meetings remotely. The work of this thesis would not have been possible without the help from my collaborators. I thank Dr. Elias Zambidis and Dr. Michal Millrod for their contribution in the hEB project, Dr. René Vidal and Giann Gorospe for their expertise in machine learning, Dr. Natalia Trayanova, Dr. Patrick Boyle and Joseph Yu for their immense knowledge in computational modeling.

This work would not have been possible without the support from members of the Cardiac Bioelectric Systems Lab. I thank Dr. Seth Weinberg and Dr. Susan Thompson for their help during the early years of my graduate study. Special thanks to Dr. Adriana Blazeski, Dr. David Hunter and Geran Kostecki for their inspirations during countless

discussions throughout all the years and making the lab an enjoyable place to work in. I am grateful for Dr. Yin Wang for bringing rich experience in cell and molecular biology to the lab. I thank Dr. Venkatesh Hariharan for being an inspiration to me. I also thank Justin Lowenthal for bravely taking over the cell culture task as the new member of the lab.

I'm also grateful for members in Dr. Tomaselli's lab, Deborah DiSilvestre and Dr. Federica Farinelli, for their extensive help in the LQT2 project, and especially for those times I had to borrow lab supplies to get research going.

Last but not least, I would like to thank my family for their support. I thank my parents for always being strong support and inspiration, especially during my Ph.D. study. I thank my wife Yujing, for her unwavering love and companion, and the decision to embark on the journey of graduate study together with me. I also thank my son Chenhao, for his patience when I am writing this dissertation.

Table of contents

List of figures

List of tables

Chapter 1

Introduction

1.1 General overview

The heart is the central organ in the cardiovascular system, driving blood throughout the circulatory system 24 hours a day, 365 days a year. Diseases in the cardiovascular system are the leading cause of death globally, responsible for an estimated 17.3 million deaths in 2013 (Benjamin et al., 2017). The mechanical function of the heart is modulated by its electrical activities, known as cardiac electrophysiology.

The electrical activities in the heart originate from the generation of cardiac action potentials within individual cardiomyocytes, which involve the coordinated operation of a large family of current-conducting ion channels. Action potentials then propagate throughout the heart, triggering mechanical contractions of the myocardium to circulate blood throughout the human body. Mechanistic understanding of human cardiac electrophysiology relies on various *ex vivo* and *in vitro* experimental models. Human heart

tissue excised during surgery has been used for electrophysiological studies as isolated muscles (Page et al., 2016; Trautwein et al., 1962), perfused wedge preparation (Boukens et al., 2015), organotypic slices (Kang et al., 2016), or isolated cardiomyocytes (Peeters et al., 1995). However, the scarce availability of human heart tissue has encouraged the development of alternative models, including large and small animals, isolated hearts, isolated cardiac tissues and cell culture models (Sigg et al., 2010). Advances in human genetics and molecular and cell biology also enabled the use of heterologous expression systems, where cardiac ion channels are expressed in non-cardiomyocytes (such as Xenopus oocytes, Chinese hamster ovary cells and human embryonic kidney cells), to study their electrophysiology (Taglialatela, 2003).

However, differences in cross-species cardiac electrophysiology can confound the interpretation of findings in non-human models. Further, the lack of interactions between multiple ion channels limits human non-cardiomyocyte heterologous expression systems to investigations of single channel electrophysiology. Recently, the development of human pluripotent stem cells and their subsequent differentiation into cardiomyocytes has provided a novel platform for *in vitro* cardiac electrophysiology in human cardiomyocyte context.

1.2 Human pluripotent stem cells and cardiac differentiation

Human pluripotent stem cells (**hPSCs**) are cells that are capable of self-renewal and can be differentiated into descendants of all three germ layers. These cells can be derived from human primordial germ cells (Shamblott et al., 1998), human embryos (Thomson et al., 1998) or somatic cells (Takahashi et al., 2007), with the latter two being

most widely used, termed human embryonic stem cells (**hESCs**) and human induced pluripotent stem cells (**hiPSCs**), respectively. Thomson et al. was the first to derive hESC lines in 1998 (Thomson et al., 1998) using a similar methodology that had been developed for mouse ESC lines. The hESCs were derived from the inner cell mass from human embryos, which were donated from the result of *in vitro* fertilization procedures, then established as immortal cell lines under conditions that supported the maintenance of their pluripotency. The resulting cell lines could be passaged indefinitely, and are capable of spontaneously differentiating into all three embryonic germ layers. In 2007, one year after success in mouse cells, Takahashi et al. reported a new method of generating human pluripotent stem cells (Takahashi et al., 2007). By forced expression of four factors: Oct3/4, Sox2, Klf4 and c-Myc, they showed that adult cells can be reprogrammed into an embryonic stem cell-like state. This Nobel Prize-winning discovery completely changed stem cell research and many related fields. The hiPSCs derived from adult human cells share many key properties of their embryonic cell counterparts, including capability of self-renewal, expression of pluripotent markers, and generation of all three germ layer cells. Further, the hiPSC lines preserve the genetic phenotype of their respective donors, enabling *in vitro* modeling of genetic diseases. Since then, the derivation of hiPSCs has been evolving rapidly. New reprogramming methods have been developed using different delivery vectors. More recently, vector-free methods have also been developed, aimed at improving the efficiency of hiPSC reprogramming as well as reducing the footprint of reprogramming (Malik and Rao, 2013). Despite the still relatively low reprogramming efficiency (generally <1%), hiPSCs are now being routinely generated in research labs around the world. For both hESCs and hiPSCs, the maintenance of their pluripotent state

in culture has also moved progressively from feeder-dependent methods (co-culture with mouse embryonic fibroblasts) to feeder-free, chemically defined, and xeno-free methods, improving the consistency of the cells and facilitating their potential clinical applications (Chen et al., 2011; Fan et al., 2014).

Upon removal of factors maintaining their pluripotency, such as mouse embryonic fibroblast (**MEF**) feeder cells, and when cultured in suspension, hPSCs self-aggregate to form clusters, termed embryoid bodies (**hEBs**). These hEBs can spontaneously differentiate into cells from all three germ layers, including mesoderm that later gives rise to the heart. The monumental work by Kehat et al. demonstrated that a small percentage of these hEBs were spontaneously contracting and contained cells positive for cardiomyocyte markers, exhibiting electrogram and calcium transient activities (Kehat et al., 2001). These results showed that hESCs can spontaneously differentiate into human cardiomyocytes (**hESC-CMs**). The self-aggregating hEB method was later successfully applied to hiPSCs (Zhang et al., 2009) to generate cardiomyocytes (**hiPSC-CMs**). Early methods based on self-aggregated hEBs yielded a mixture of different cell types, including cardiomyocytes, and were low in efficiency, typically generating <10% cardiomyocytes. They were also dependent on the stem cell lines and did not transfer well across different hPSC lines. During the last decade, great improvement has been made to improve both the quality and quantity of cardiomyocytes derived from hPSCs (**hPSC-CMs**). By mimicking different stages of embryonic heart development, researchers have developed differentiation protocols that sequentially activate or inhibit known pathways that are involved in cardiogenesis, and have successfully generated cardiomyocytes at near 100% efficiency (Mummery et al., 2012). Overall, there are three major types of methods for cardiac

differentiation of hPSCs. The first type of methods is hEB-based. By utilizing tissue engineering approaches, such as forced aggregation (Burridge et al., 2011), microwells (Mohr et al., 2010) or micropatterned islands (Bauwens et al., 2008), the consistency and throughput of hEB-based differentiation were greatly improved compared to self-aggregated hEBs. The second type of methods is based on feeder-free monolayer culture of hPSCs, and cardiac differentiation was directly carried out in monolayer culture, simplifying the requirements for cell culture (Bhattacharya et al., 2014; Burridge et al., 2015; Lian et al., 2012). The third type of methods is based on co-culture of hPSCs with visceral endoderm-like END2 cells, which has been shown to promote cardiogenesis (Mummery et al., 2003; 2007). Along with the improvement of cardiac differentiation efficiency, significant progress has also been made in developing scalable and robust production strategies for generating hPSC-derived cardiomyocytes in large quantity (Jenkins and Farid, 2015) with emerging commercially available products. Overall, both the quality and availability of hPSC-derived cardiomyocytes have greatly improved over the last decade, further facilitating their applications, including the study of human cardiac electrophysiology.

1.3 Electrophysiology of hPSC-derived cardiomyocytes

The first electrophysiological descriptions of hPSC-derived cardiomyocytes were the extracellular electrograms and intracellular Ca^{2+} transients generated by spontaneously differentiated hEBs (Kehat et al., 2001). The electrograms had a sharp component, corresponding to the rapid depolarization of the cardiomyocytes, followed by a relaxation component, corresponding to the slower repolarization. The Ca^{2+} transients had a rise and

slower decay. Both the electrograms and Ca^{2+} transients shared similar characteristics of native cardiomyocytes. Shortly afterwards, with the use of microelectrode arrays (**MEAs**), the same group demonstrated that electrical activity can spread within hEBs (Kehat et al., 2002), suggesting the formation of a functional syncytium, another important property of human myocardium. These initial observations attracted significant research interest in exploring the electrophysiological properties of these *in vitro* derived human cardiomyocytes and their potential application as a model for electrophysiological studies.

Action potentials are of paramount importance in cardiac electrophysiology, and are therefore extensively studied in hPSC-derived cardiomyocytes. Microelectrode recordings from both hESC- and hiPSC-derived cardiomyocytes demonstrated variable shapes of action potentials, roughly resembling nodal, atrial and ventricular action potentials found in the adult human heart (He et al., 2003; Zhang et al., 2009). These observations led to empirical classifications of hPSC-derived cardiomyocytes into these three phenotypes. However, a consistent set of quantitative criteria for phenotype identification has been difficult to establish (reviewed in (Blazeski et al., 2012a) and (Blazeski et al., 2012b)). This difficulty in classification has led to discussions on how action potential morphologies should be interpreted with regard to phenotype identification (Bett et al., 2016; Du et al., 2015; Giles and Noble, 2016; Kane et al., 2016).

The immaturity of hPSC-derived cardiomyocytes contributes to their variable action potentials. At the transcriptome level, hPSC-CMs demonstrate a profile most closely resembling embryonic or fetal cardiomyocytes (Piccini et al., 2015; Poon et al., 2013). They are also morphologically smaller than adult myocytes, do not have elongated shape, and lack transverse tubules (T-tubules) (Yang et al., 2014). Electrophysiologically, hPSC-

CMs generally display spontaneous activity and have more depolarized membrane potential at rest compared to adult cardiomyocytes (Doss et al., 2012; Ma et al., 2011). Functional Ca^{2+} stores in the sarcoplasmic reticulum (SR) and SR Ca^{2+}-ATPase (SERCA)/Ryanodine receptor (RyR)-mediated calcium handling have been reported in hiPSC-CMs (Itzhaki et al., 2011b). Various strategies have been implemented to promote maturation in hPSC-derived cardiomyocytes (reviewed in (Zhu et al., 2014)), such as in-culture electrical stimulation (Chan et al., 2013; Hirt et al., 2014), forced expression of I_{K1} (Lieu et al., 2013), and electronically hyperpolarized resting potentials in hPSC-CMs (Bett et al., 2013).

1.4 Ion currents associated with action potentials in hPSC-CMs

The cardiac action potential is the change in transmembrane potential ($\boldsymbol{V_m}$) of a cardiomyocyte, which is the result of organized opening and closing of current-conducting ion channels (Fig. 1.1, reviewed in (Baró and Escande, 2008)). In ventricular cardiomyocytes, an action potential begins with the activation of voltage-gated Na^+ channels, which carry an inward current (I_{Na}) and depolarizes V_m. This depolarized V_m further activates several voltage-gated channels that carry both inward Ca^{2+} (I_{CaL}) and outward K^+ (I_{to}, I_{Kr} and I_{Ks}) currents. These currents modulate the shape of the action potential and regulate the mechanical contraction of a cardiomyocyte. With the progressive inactivation of these mid-action potential currents (I_{CaL}, I_{to}, I_{Kr} and I_{Ks}) and the progressive activation of another K^+ current (I_{K1}), the V_m eventually returns to its resting state at a repolarized potential of ~80 mV, marking the end of an action potential. During the action potential, ion pumps and exchangers (mainly Na^+/K^+ pump and Na^+/Ca^{2+} exchanger) also

activate to restore gradients in ion concentrations necessary for generating action potentials, and also carry transmembrane currents that affect V_m.

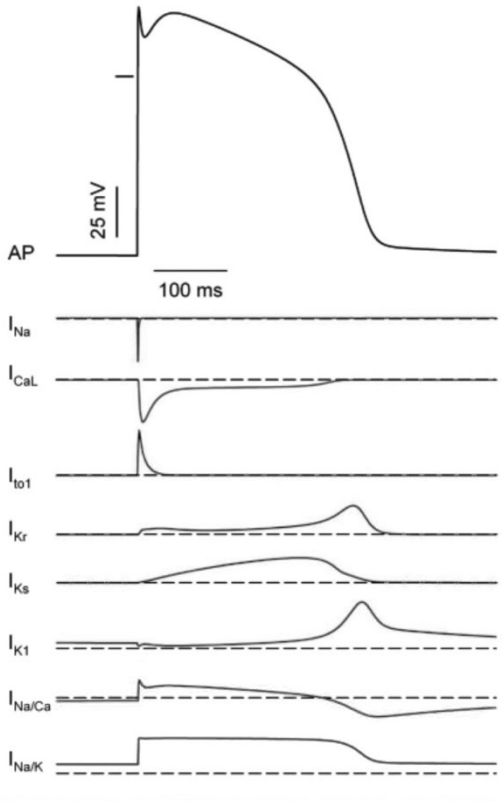

Figure 1.1 Schemes of the cardiac action potential and underlying ion currents. Modified from (Baró and Escande, 2008)

Action potentials in hPSC-CMs are also governed by ion currents that are found in human cardiomyocytes, but significant differences exist, largely associated with the immaturity of hPSC-CMs (reviewed in (Liu et al., 2016; van den Heuvel et al., 2014)). In general, the resting V_m in hPSC-CMs is more depolarized compared to adult cardiomyocytes, which is believed to be because of the low I_{K1} expression level. Forced overexpression of I_{K1}, either cellularly (Lieu et al., 2013) or electronically(Bett et al., 2013) has been shown to improve the AP recorded in hPSC-CMs towards a more mature phenotype. Spontaneous activity is also generally observed in hPSC-CMs, even in those

characterized as having a ventricular-like phenotype. This can be explained by the expression of pacemaker genes in the HCN family in hPSC-CMs, which conduct the funny current (I_f) responsible for spontaneous depolarization in adult pacemaker cells, although a Ca^{2+} clock-based mechanism has also been reported (Kim et al., 2015). The major currents shaping the action potential (I_{CaL}, I_{Kr}, I_{Ks} and I_{to}) have all been recorded in hPSC-CMs, and these currents also respond to their respective blockers in patch clamp studies (Ma et al., 2011). However, the levels of currents, as well as the expression of their corresponding genes, are highly variable among studies (Liu et al., 2016).

The immature electrophysiological phenotype of hPSC-CMs is also affected by various *in vitro* factors. Extended time in culture after initiation of differentiation has been reported to lead to a more mature hPSC-CM phenotype, both structurally and electrophysiologically (Lundy et al., 2013; Robertson et al., 2013). There is also a tendency of hPSC-CMs shift from nodal-like to atrial/ventricular-like phenotypes with prolonged culture (Ben-Ari et al., 2016). Ion currents associated with APs generally increase in intensity with extended time in culture, including I_{Na}, I_{CaL}, I_{Kr}, I_{Ks} and I_{to}, as well as pump current I_{NaCa}, with the important exception of I_{K1}, which remains generally absent even during prolonged culture (Liu et al., 2016). The changes in electrophysiology of hPSC-CMs are associated with physical cues that also promotes cardiomyocyte maturation during heart development. For example, chronic electrical pacing has been shown to improve the maturity of hESC-CMs in terms of reduced spontaneous activity, more hyperpolarized resting potential and increased AP-associated ion channel expression (Chan et al., 2013; Lieu et al., 2013). Further, mechanical stimulation and three-dimensional culture methods

have also been shown to improve the maturity in the electrophysiology of hPSC-CMs (Zhu et al., 2014).

1.5 Disease modeling with human induced pluripotent stem cells

Congenital heart diseases are abnormalities in the function of the heart as a result of genetic disorders. It affects more than 9 per 1000 live births worldwide and is one of the major congenital anomalies (van der Linde et al., 2011). Mechanistic understanding of disease pathogenesis, phenotype and treatment evaluation requires development of *in vitro* disease models. While a limited repository of hESC lines with genetic disorders has been reported (Verlinsky et al., 2005), and mutant hESC lines could be created by genetic modification (Bellin et al., 2013), in practice working with hESC diseased models is very difficult and of limited application due to limited availability of the cell lines and complex procedure of genetic modification. The development of human iPSC-derived cardiomyocytes has provided an exciting platform for mechanistically studying inherited cardiac diseases, since iPSCs can be derived directly from patient somatic cells, preserving the patient-specific genotype in subsequent differentiation into cardiomyocytes. It has promising applications in both monogenic and multifactorial genetic disorders. The first hiPSC disease model was developed from patients with a familial form of amyotrophic lateral sclerosis (ALS), and the authors demonstrated that disease-relevant cells, in this case motor neurons, could be differentiated from the patient-specific hiPSCs (Dimos et al., 2008). In the cardiac field, Carvajal-Vergara et al. was first to report a disease model with cardiac consequences -- the multisystem genetic disorder known as LEOPARD syndrome (Carvajal-Vergara et al., 2010). It was found that cardiomyocytes differentiated from

patient-derived iPSCs had phenotypic characteristics resembling a hypertrophic state, which is a condition common in LEOPARD syndrome patients. The *in vitro* recapitulation of a disease phenotype in hiPSC-CMs demonstrated the promise of patient-derived iPSCs for cardiac disease modeling, and led to the development of many hiPSC-based cardiac disease models (Shaheen et al., 2017).

The major congenital heart diseases that have been studied in hiPSC-derived cardiomyocyte models include cardiac channelopathies and cardiomyopathies (Matsa et al., 2014). In cardiac channelopathies, mutations in cardiac ion channels lead to abnormalities in cardiac electrophysiology and arrhythmia. This mainly includes long-QT syndrome (**LQTS**) (Moretti et al., 2010) and catecholaminergic polymorphic ventricular tachycardia (**CPVT**) (Novak et al., 2012). In cardiomyopathies, genetic mutations lead to myocardial dysfunction such as dilated cardiomyopathy (**DCM**) (Sun et al., 2012), hypertrophic cardiomyopathy (**HCM**) (Lan et al., 2013) and arrhythmogenic right ventricular cardiomyopathy (**ARVC**) (Kim et al., 2013).

The most extensive family of diseases that has been modeled with hiPSC-derived cardiomyocytes is long-QT syndrome, as this is often the result of a single gene mutation (Tester and Ackerman, 2014). Electrophysiological consequences of LQTS include prolonged QT interval and increased risk of developing a specific type of polymorphic ventricular tachycardia known as Torsades de Pointes (**TdP**). Three genes that account for the majority of LQTS are *KCNQ1*, *KCNH2* and *SCN5A*, encoding the alpha subunits of the cardiac ion channels: I_{Ks}, I_{Kr} and I_{Na}, respectively. Multiple mutations have been identified within each gene to be responsible for LQTS and have been modeled with hiPSC-derived cardiomyocytes (reviewed in (Blazeski et al., 2012b; Shaheen et al., 2017; Yang et al.,

2015)). Electrophysiological consequences of LQTS mutations are widely studied by using patch clamp or MEAs in cardiomyocytes derived from patient-specific hiPSCs. These cardiomyocytes have been found to have prolonged action potentials and increased occurrence of ectopic activity such as early afterdepolarizations (**EADs**) (Itzhaki et al., 2011a; Lahti et al., 2012; Matsa et al., 2011; Moretti et al., 2010), which reflect the corresponding abnormal function in ion channels specific to the mutations. Patient-specific hiPSC-CMs also provide a valuable platform to evaluate rescue strategies for LQTS. Some examples include modulation of the hERG channel to compensate for loss of function in I_{Ks} in an LQT1 model (Zhang et al., 2012), pharmacological rescue of a trafficking defect in an LQT2 model (Mehta et al., 2014a) and most recently, genome editing in an LQT15 model (Yamamoto et al., 2017).

1.6 Drug-induced proarrhythmia testing

To successfully bring a lead compound found in drug discovery to the market, it must go through a thorough process of preclinical and clinical evaluations before obtaining approval from the regulatory agency. Once on the market, all drugs are still constantly monitored for potential adverse effects and are subject to withdrawal if adverse effects do arise. This is a process that associates with a cost of hundreds of millions of dollars per drug (DiMasi et al., 2003). Regardless of whether the drug in development is intended for treating cardiac disease, cardiac safety is among the top reasons for the termination of drug development or even withdrawal of drugs already in the market (Fung et al., 2001). The main concerns of cardiac safety are direct cardiomyocyte toxicity which leads to myocardial cell necrosis, and proarrhythmia which leads to increased risk of sudden and

life-threatening arrhythmic events. While effective biomarkers such as serum cardiac troponin has been identified for early detection of cardiomyocyte toxicity (Gaze and Collinson, 2005), the evaluation of drug-induced proarrhythmia has proven to be more difficult, especially in finding a preclinical biomarker or assay that can accurately predict the rare, but potentially lethal, occurrence of drug-induced arrhythmia in clinical use.

The most common drug-induced arrhythmia is TdP, a type of polymorphic ventricular tachycardia which has a distinct appearance in the electrocardiogram (**ECG**) and can degenerate into life-threatening ventricular fibrillation. TdP is well acknowledged to be associated with the prolongation of the QT interval in the ECG (in congenital or acquired LQTS). More than a decade ago, Redfern et al. performed a thorough investigation of the relationships between QT prolongation, occurrence of TdP and preclinical biomarkers for 100 drugs, and concluded that blockade of hERG is associated with most TdP-associated drugs (Redfern et al., 2003). The strong correlation between hERG blockade, QT prolongation and TdP facilitated the development of the preclinical hERG-based assay and the clinical thorough QT study (**TQT**) and eventually led to the establishment of two International Conference on Harmonization (**ICH**) guidelines: S7B on non-clinical evaluation and E14 on clinical evaluation of QT prolongation and drug proarrhythmia. The interactions between a lead compound and the hERG channel can be tested by several different assays, ranging from high throughput non-functional binding assays, to medium throughput flux- or fluorescence-based assays, to low throughput manual or automatic patch clamp assays (Priest et al., 2008). These assays have been used in different phases of drug development.

The electrophysiological basis of hERG-based assays lies in the role of I_{Kr} in the cardiac action potential. I_{Kr}, the rapid component of the delayed outward rectifying current, is a repolarizing current that is conducted through a potassium ion channel with hERG encoding its alpha subunit. Blockade of I_{Kr} leads to a delay in repolarization and increase in duration of the action potential, which manifests as a prolonged QT interval in the ECG. However, cardiac action potentials are the result of delicately balanced ion currents. I_{Kr} is not the only current determining action potential duration and QT interval. Interactions of the drug with multiple ion channels can either augment or weaken the effect of the drug on the action potential beyond the effect on hERG alone.

A delay in repolarization or QT prolongation *per se* is proarrhythmic because it can favor the formation of EADs and ectopic activity in the heart. However, a heterogeneous substrate, which favors wavefront curvature and conduction block, could lead to reentrant arrhythmia under certain conditions (Boukens et al., 2016). For these two reasons, along with others, it is apparent that the hERG assay may be inadequate as a biomarker for drug-induced proarrhythmia. In fact, there are drugs that block hERG current but do not prolong QT interval, such as fluoxetine and verapamil (Gintant et al., 2006), and drugs that prolong QT interval through hERG blockade, but are extremely low in risk of proarrhythmia, such as amiodarone, quetiapine, phenobarbital and ranolazine (Piccini et al., 2009). Overall, the performance of the hERG-based assay in determining drug-induced proarrhythmia is limited, and therefore new strategies for drug discovery are warranted (Gintant, 2011).

1.7 Overview of thesis

Human PSC-derived cardiomyocytes present an exciting tool for *in vitro* studies of human cardiac electrophysiology. The goal of this thesis is to explore the utility of hPSC-CMs in a syncytial context, where large populations of cells can interact and exhibit coordinated electrical activity, much like the native myocardium. In **Chapter 2**, electrophysiological characteristics of hPSC-CMs are compared between a small cell cluster and a large syncytial cell monolayer, especially in terms of the variability in action potentials. This comparison provides a baseline characterization of hPSC-CM electrophysiology in cell monolayers. In **Chapter 3**, a disease model with a syncytial monolayer is studied by using cardiomyocytes carrying a mutation that leads to type 2 LQTS, and a potential pharmacological rescuing strategy is evaluated. In **Chapter 4**, the syncytial monolayer model is applied to test the response of hiPSC-CMs to cardioactive drugs, and how such monolayer models can provide insight into drug-induced proarrhythmia is discussed. I conclude in **Chapter 5** by discussing the implication and limitations of the current study and potential future directions for electrophysiological studies with hPSC-CM syncytial models.

Chapter 2

Electrophysiology and variability in human PSC-CMs

2.1 Introduction

Cardiomyocytes derived from human pluripotent stem cells are a novel platform for the *in vitro* study of cardiac physiology. The self-renewal capability of hPSCs allows virtually unlimited access to precious human cardiomyocytes. Further, cardiomyocytes derived from hiPSCs carry the same genotype as their donor, enabling *in vitro* disease models to be developed. However, our understanding of hPSC derived cardiomyocytes is far from comprehensive, making it difficult to interpret findings in hPSC-CMs.

Cardiac electrophysiology is the physiology of the electrical activity in cardiomyocytes, which involves the coordinated operation of cardiac ion channels that carry electrical currents across the cell membrane. At the cellular level, this generates action potentials, where cardiomyocytes go through phases of depolarization, plateau,

repolarization and rest. This highly organized sequence of events initiates and regulates the mechanical contractile function of cardiomyocytes, which fulfills the heart's function to pump blood throughout the circulatory system.

The balanced interaction of ion channels that governs cardiac action potentials is subject to biological variability. In the native heart, this variability manifests mainly in two ways. First, cardiomyocytes located in different regions of the heart have different electrophysiology adapted to their specialized role. For example, cardiomyocytes in the sinoatrial node have a spontaneous depolarizing resting phase because of I_f expression. The rate of this spontaneous depolarization sets the heart rate. On the other hand, cardiomyocytes in the ventricles are characterized by having a prominent plateau phase, where the membrane potential stays relatively close to 0 mV for an extended period, allowing calcium to enter the cell and facilitating electrical-contraction interactions that are key in the process known as excitation-contraction coupling. These major phenotypic differences in cardiomyocyte electrophysiology are the result of different functional specializations within the heart and are developed based on the major anatomical structures such as the four chambers and the conduction system within the heart (Baró and Escande, 2008). Second, in addition to the major phenotypes, there are subtle differences in electrophysiology of cardiomyocytes within the same phenotype, such as the transmural heterogeneity across the ventricular wall, where cardiomyocytes from the endocardium and epicardium have slight differences in action potential shape and duration. These subtle differences compensate for the non-simultaneous ventricular activation and is essential for healthy cardiac function. However, when the heterogeneity become excessive it can also lead to arrhythmia (Boukens et al., 2016).

Cardiomyocytes derived from hPSCs recapitulate many important properties of the native human cardiomyocyte in terms of their electrophysiology and cell and molecular biology. Action potentials recorded from hPSC-CMs have shown that they resemble those of all three major phenotypes of native cardiomyocytes. However, the criteria for assigning electrophysiological phenotypes are inconsistent among research groups. Attempts have also been made to study the electrophysiology of hPSC-derived cardiomyocytes in large populations of cells (López-Redondo et al., 2016), but due to the low throughput patch-clamp procedure, this has been greatly limited to only 93 samples.

In this chapter, I investigate the electrophysiology of hPSC-derived cardiomyocytes obtained from two different cardiac differentiation methods. The first one is an hEB-based method, which generates independent aggregates of cells containing cardiomyocytes. In this model, the electrophysiology of cardiomyocyte populations is analyzed both across hEBs and within each hEB. The second differentiation method is monolayer-based, which generates cardiomyocytes in a much larger, tissue-like context and enables measurement of tissue-level properties such as conduction which is very difficult with small clusters. By using high-resolution optical mapping, I study action potentials recorded simultaneously from hundreds to thousands of sites within a single preparation. The work on hEBs in this chapter has been published (Zhu et al., 2016).

2.2 Methods

2.2.1 Human PSC culture and cardiac differentiation

For hEB-based cardiac differentiation, the H9 line of hESCs (WiCell WA09) was used. H9 hESCs were maintained on a layer of MEF feeder cells and dissociated to form

hEBs just before initiation of differentiation. Spontaneous beating hEBs were obtained using a forced aggregation method with 5×10^3 cells initially seeded per aggregate (Burridge et al., 2011; Burridge and Zambidis, 2013). Beating areas of hEBs from the same differentiation batch were mechanically dissected on day 15 of differentiation, and then transferred to plastic coverslips coated with 0.1% gelatin (Sigma-Aldrich). These cardiac cell clusters were maintained in culture for at least 5 days to attach and recover before optical mapping experiments were conducted at 21-24 days after initiation of differentiation.

For monolayer-based cardiac differentiation, the WT11 line of hiPSCs (a kind gift from Dr. Bruce Conklin, UCSF) was maintained in feeder-free monolayer culture in Essential 8 medium (ThermoFisher) and differentiated into cardiomyocytes using a monolayer-based protocol (Boheler et al., 2014; Wang et al., 2015). Beating monolayers were dissociated with 0.05% Trypsin (ThermoFisher) and re-plated on Geltrex (Gibco)-coated cell culture plates between 15 and 20 days after initiation of differentiation. A second dissociation was performed 5-7 days afterwards, after which the beating cardiomyocytes were seeded at 3×10^5 cells/cm^2 density onto a Geltrex-coated 35 mm diameter tissue culture dish. The growth area of the tissue culture dish was restricted to a 10 mm diameter circle by using a polydimethylsiloxane (**PDMS**) stencil: PDMS was filled and heat-cured in 35 mm diameter tissue culture dishes to completely block the cell culture-treated surface, after which a 10 mm diameter core of PDMS was removed by a dermal punch, exposing the cell culture-treated surface underneath. This exposed surface was then coated with Geltrex. The use of the PDMS stencil created a defined size and shape of the monolayer, which was matched to the field of view of the optical mapping system. The

monolayers were kept in culture for 35-55 days total after initiation of differentiation before proceeding further with experiments. A small percentage of monolayers that detached from the culture vessel during this time were excluded from experiments.

Commercially available Cor.4U hiPSC-CMs were obtained as frozen vials (Lot CB142CL_V_4M) from Axiogenesis along with manufacturer-provided culture media. Cells were thawed into fibronectin-coated T75 tissue culture flasks per the manufacturer's protocol and kept for 2 days for recovery. Cells were then dissociated and re-plated onto fibronectin-coated 35 mm dishes at 1.6×10^5 cells/cm^2 to form confluent cell monolayers. The growth area was also restricted to a 10 mm diameter circle by a PDMS stencil. The monolayers were cultured for an additional 7 to 8 days per the manufacturer's recommendation before optical mapping experiments began.

2.2.2 Optical mapping

Optical recordings of action potentials were performed using epifluorescence imaging. Both hEBs and monolayers were stained with 10 μM di-4-ANEPPS (ThermoFisher), a voltage-sensitive dye, for 10 min to enable optical recordings of electrical activity. The samples were kept in Tyrode's solution (135 mM NaCl, 5.4 m M KCl, 1.8 mM $CaCl_2$, 1.0 mM $MgCl_2$, 0.33 mM NaH_2PO_4, 5.0 mM HEPES and 5.0 mM glucose, all from Sigma-Aldrich) warmed to 37°C throughout the experiments. To inhibit motion, blebbistatin (Sigma-Aldrich), a myosin II inhibitor, was added to the Tyrode's solution at 50 μM for hEB experiments and at 10 μM for monolayer experiments. For experiments with applied cardioactive compounds, including E-4031 and carbenoxolone (both from Tocris), each compound was prepared as a stock solution that was 1000× the concentration of the lowest concentration tested in dimethyl sulfoxide (for E-4031) or

water (for carbenoxolone). The stock solution of the volume equal to 1/1000 of the volume of Tyrode's solution in the mapping chamber was added during optical mapping to yield the desired test concentration. When multiple concentrations were tested, the higher concentrations were achieved by serially adding the differential amount of necessary stock solution into the mapping chamber containing Tyrode's solution.

Electrical pacing was delivered through a pair of platinum electrodes. For hEB experiments, electrodes were placed across hEBs, delivering field pacing as 5-10 ms rectangular voltage pulses. Pacing rate started at 60 beats per minute (**bpm**), and was incremented in steps of 30 bpm until the cluster failed to maintain 1:1 capture by the pacing stimulus. For monolayer experiments, point pacing was delivered at the edge of the monolayer to initiate propagating action potentials across the monolayer. A cycle length of 1000 ms, equivalent to 60 bpm, was used for monolayer experiments.

Optical action potentials were recorded using a MiCAM Ultima-L CMOS camera with 100 × 100 pixels at 500 frames per second (**fps**). The schematic of the optical mapping system is shown in Fig. 2.1A, and a photograph of the mapping setup with details of the objectivelens, pacing electrode, sample and heated stage is shown in Fig. 2.1B. A tandem combination of a 5x objective and 0.63x condensing lens was used for hEB experiments, resulting a 1.6 mm-by-1.6 mm field of view (16 μm/pixel). A tandem combination of a 1x objective and 1x condensing lens was used for monolayer experiments, resulting a 1cm-by-1cm field of view (100 μm/pixel).

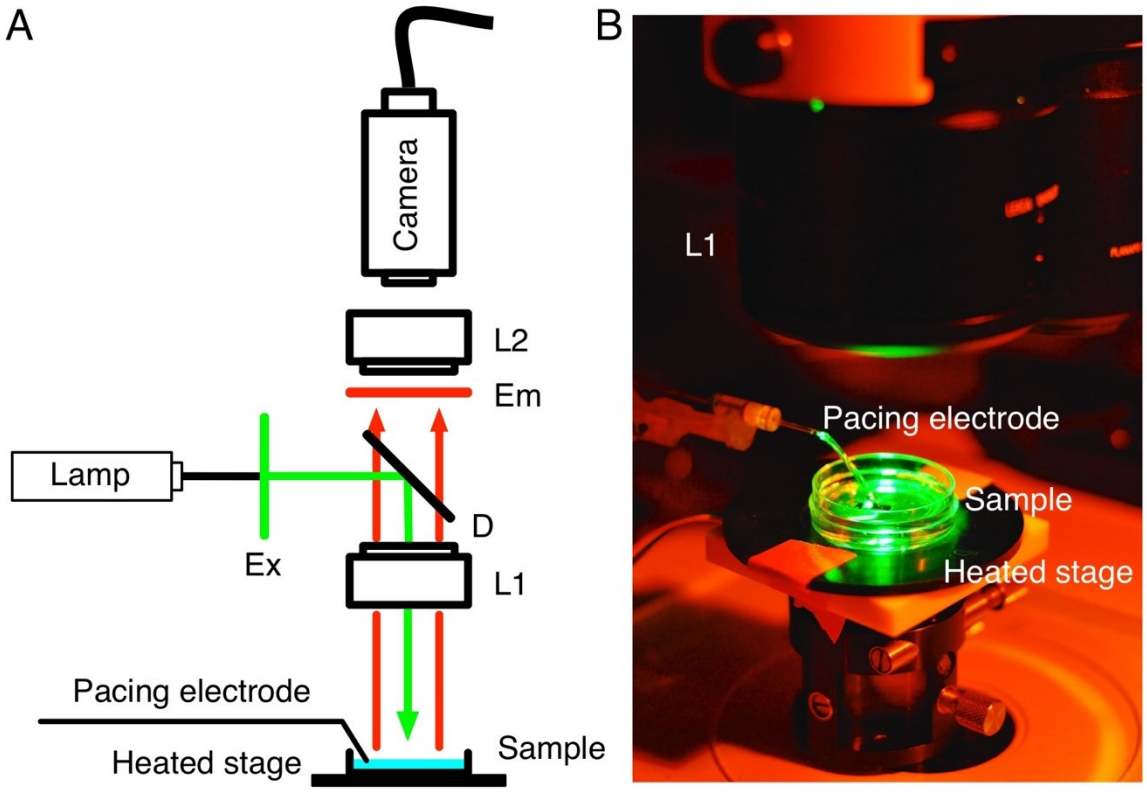

Figure 2.1 The optical mapping system. (**A**) Schematic drawing of the optical mapping system. The excitation light (Lamp, 2 × 150W halogen lamps) is filtered through an excitation filter (Ex, 531/40 nm bandpass) and reflected by the dichroic mirror (D, 560 nm), through the objective lens (L1, switchable various magnifications) onto the Sample sitting on a Heated stage. The emission light is collected through L1, and the component longer than 560 nm passes through D, filtered by the emission filter (Em, 610 nm longpass) and projected through the condensing lens (L2, switchable various magnifications) onto the CMOS sensor in the Camera. Pacing electrode is held by an electrode holder with the tip of the electrodes placed next to the Sample. (**B**) Photograph of the mapping system highlighting L1, Pacing electrode, Sample and Heated stage.

2.2.3 Signal processing and data analysis

For hEBs, the optical action potential recordings were convolved with a 5×5 boxcar filter to improve signal quality. The border of each cluster was traced manually to identify the recording pixels contained within that cluster. When electrical pacing was applied, multiple APs from each recording site were temporally aligned by their activation times (calculated as the time of fastest AP upstroke), after which an average of the APs was

calculated for that recording site. The averaged APs were quantified by 4 parameters: AP duration at 30% and 80% repolarization (**APD_{30}** and **APD_{80}**, respectively), triangulation (time from APD_{30} to APD_{80}) and fractional repolarization time (time from APD_{30} to APD_{80} divided by APD_{80}). For triangulation, APD_{80}, rather than APD_{90} as originally defined by Hondeghem et al., (Hondeghem et al., 2001) was used because in some cells the AP had a slow repolarizing tail following the rapid repolarization phase, making measurements of the time of 90% repolarization difficult. These four parameters were used to quantify AP variability within and among clusters. Principal component analysis (Abdi and Williams, 2010) was used to determine the linear combination of AP parameters that accounted for the most variability within the dataset by orthogonal transformation. Levene's test of equal variances was used to compare the variability in APD_{80} at spontaneous or paced conditions.

For monolayers, optical action potential recordings were convolved with a 5×5 Gaussian filter to improve signal quality. The portion of the camera image that corresponded to the monolayer was identified by including pixels whose optical signal contained a primary frequency component equal to the frequency of applied electrical pacing. Both APD_{30} and APD_{80} were calculated as defined for hEB experiments, and the interquartile range of APD_{80} (**IQR-APD_{80}**), the range between the 25^{th} and 75^{th} percentile of APD_{80}, was used to quantify action potential variability in the monolayers.

2.2.4 Automated grouping

For hEB experiments, action potentials recorded from clusters paced at 90 bpm were separated into groups based on their action potential morphology, using a waveform-based automated algorithm previously described (Gorospe et al., 2014). This grouping algorithm had been developed using data from 9 of the 32 clusters presented here. Briefly,

APs were divided into 2 or 3 groups based on an unsupervised, spectral clustering technique that amasses APs with similar shapes together and separates APs having different shapes. The similarity between pairs of APs is calculated mathematically as a weighted function based on the cumulative squared errors between the two temporal waveforms. Davies-Bouldin Index (**DBI**) (Davies and Bouldin, 1979) was also calculated using the cumulative squared errors, to compare cluster separation for different numbers of groups. Linear decision boundaries in pairs of AP parameter spaces were derived by support vector machines (**SVMs**) using labels determined by the spectral clustering.

2.2.5 Statistics

Data are presented as mean±SD, with n values provided. Levene's test of equal variances was used to compare the variability in APD_{80} at spontaneous or paced conditions. The paired Student's t-test was used to compare IQR-APD_{80} and conduction velocities before and after drug applications, where a significance level of $p < 0.05$ was used.

2.3 Results

2.3.1 Action potential variability in hESC-CM clusters

Spontaneous and electrically stimulated activity of cardiac cell clusters

Spontaneously beating hEBs started to emerge in culture around day 10 of differentiation. The number of beating hEBs varied as differentiation proceeded and varied among differentiation batches. To minimize inter-batch variability, hEBs from a single batch of differentiation were used, where more than 90% of hEBs were beating by day 15 (day of mechanical dissection). Although similar numbers of undifferentiated hESCs were

seeded for hEB formation (5×10^3 cells/hEB), clear differences in size and shape of hEBs and their beating areas were observed (Fig. 2.2A, left column). After mechanical dissection, all cardiac cell clusters (beating areas of hEBs) attached to the coverslip and recovered spontaneous beating within 5 days, prior to being optically mapped.

From the 55 clusters obtained from this batch, spontaneous APs were recorded using optical mapping. Both continuous (35 clusters) and episodic (20 clusters) patterns of beating were observed, the latter being identified by the existence of at least 4 seconds of quiescence between APs during the recording. Among continuously beating clusters, beating rate was unstable in 6 clusters. Action potentials recorded from different clusters exhibited different spontaneous rates and had clearly different morphologies (Fig. 2.2A, middle column). The average beating rate of stable, continuously beating clusters was 62±21 bpm (mean±SD), and their average APD_{80} was 165±49 ms (n=29). Because action potential characteristics and their underlying ion currents are known to be rate-dependent, a test of whether some of the variability in APD_{80} of the clusters could be secondary to the differences in the beat rates was performed. Thus, electrical pacing was applied as described in 2.2.2. In the examples shown, a fixed rate of 90 bpm was able to pace-capture, and reduced, but did not eliminate the differences among APs from different clusters (Fig. 2.2A, right column).

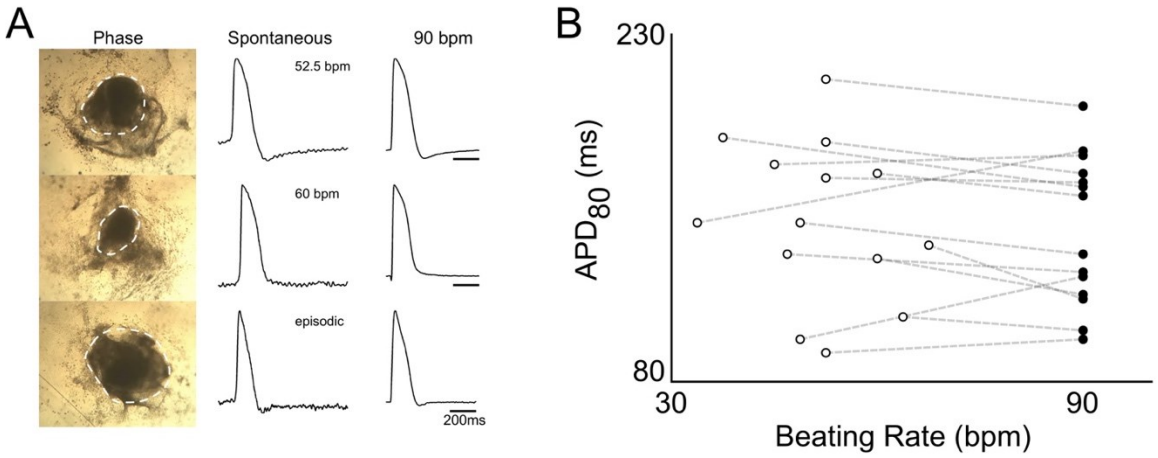

Figure 2.2 Spontaneous activity of cardiac cell clusters. (**A**) Left column: three beating hEBs at 14 days after initiating cardiac differentiation. Dashed contours indicate beating areas. Middle column: spontaneous action potentials recorded from a site in each of the cardiac cell clusters derived from the three hEBs. Right column: action potentials recorded from the same sites of each cluster during 90 bpm pacing. (**B**) APD_{80} of spontaneous and paced cardiac cell clusters. Open circles: APD_{80} of spontaneous APs recorded from 14 cardiac cell clusters. Closed circles: APD_{80} of APs recorded at fixed 90 bpm pacing rate. Dashed line connecting open and closed circles indicates the same cluster.

Overall, 14 of the 29 continuously beating clusters with stable beating rate could be entrained by electrical stimulation at 90 bpm. For these 14 clusters, individual APD_{80}s measured during spontaneous beating did not correlate with the beat rate (Fig. 2.2B, open circles), and different APD_{80}s were observed even among clusters with similar beat rate. When 90 bpm pacing was applied, there was no significant change in the mean or SD of APD_{80} (147±36 (mean±SD) ms without pacing compared with 143±33 ms with pacing, Fig. 2.2B, closed circles). In most cases, the increase in beating rate from spontaneous rate to 90 bpm produced a drop in APD_{80}, consistent with the negative rate-dependence observed in natural human cardiomyocytes/tissue, although it was the opposite case for 4 of the 14 clusters where APD_{80} increased instead. The large variability in APD_{80} at 90 bpm and the distinctly different rate-dependences among clusters indicate that both rate-

independent and rate-dependent effects contribute to the variable AP durations observed at spontaneous beat rates.

Variability of APs within cardiac cell clusters

The rate-independent variability of APs within cardiac cell clusters was first studied by pacing the clusters at a common rate of 90 bpm, and then recording the spatial distribution of action potentials via high-resolution optical mapping. A representative example is shown in Fig. 2.3A, where APD_{80} of 981 recordings obtained from a single cluster are shown as a histogram. The average APD_{80} was 119±19 ms, and two prominent distribution peaks were observed in the histogram, suggesting the existence of two subpopulations within the cluster. The advantage of optical mapping is its ability to discriminate whether the two subpopulations are interspersed or whether they cluster together spatially. In the spatial map of this cluster (Fig. 2.3B), two distinct regions having either long or short APD_{80} were apparent, indicating that on a local scale of the order of a hundred microns, cells have similar AP duration, but on a larger scale of the order of a mm, different AP durations can emerge.

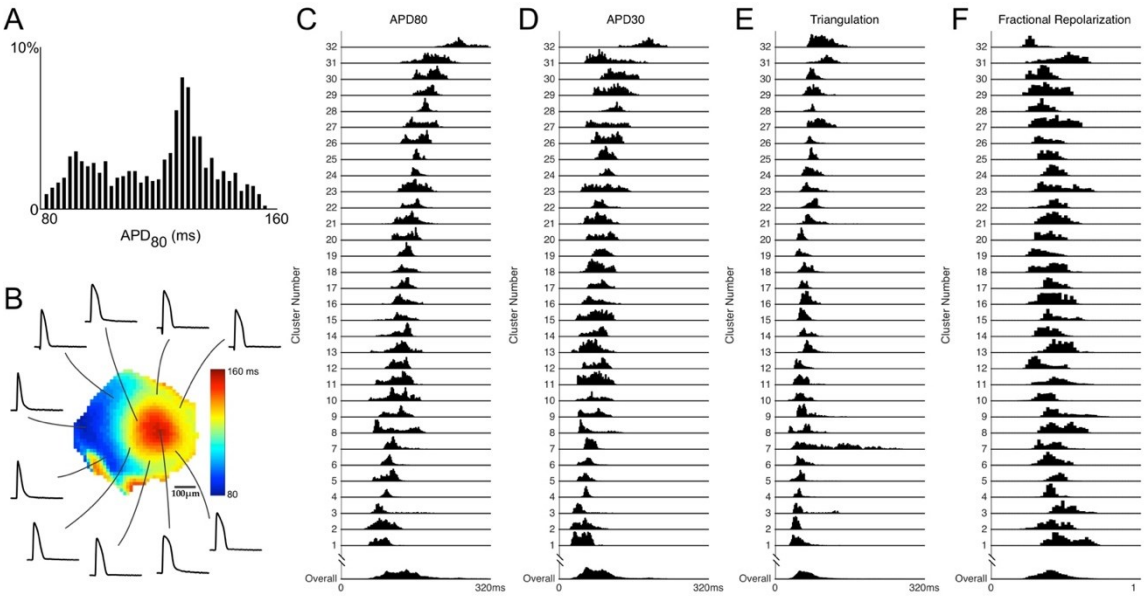

Figure 2.3 Variability of action potentials within a single cardiac cell cluster and among different clusters. (**A**) APD_{80} histogram of action potentials recorded from a cardiac cell cluster (cluster 9). Two peaks in the histogram indicate subpopulations with predominantly long or short durations. (**B**) Sample action potentials recorded from this cluster. Center: APD_{80} map, showing two distinct regions with long or short AP durations. (**C-F**) Single AP parameter histograms (APD_{80}, APD_{30}, triangulation and fractional repolarization; see main text for definition) of 32 cardiac cell clusters paced at 90 bpm. Each row represents one cluster. The overall distribution (bottom row) is the summation of all recording sites (n=23117) from these 32 clusters.

Next, AP variability within each cardiac cell cluster was compared to that among the entire cluster population. Fixed 90 bpm recordings were obtained from 32 cardiac cell clusters with an average of 722±252 recording sites in each cluster. The average and variation in AP parameters are summarized in Table 2.1. Even though some of these clusters had spontaneous activity (including the 14 continuously beating clusters analyzed in Fig. 2.2) while others were quiescent, there were no systematic differences in APs when they were paced at 90 bpm that could be correlated to their spontaneous rates. Single AP parameter distributions for individual clusters were clearly different (Fig. 2.3 C-F). In some clusters (e.g, clusters 4, 24, 25, 28), the distributions of all AP parameters were relatively

narrow, indicating a relatively homogeneous population of cells within the cluster, whereas in other clusters (e.g. clusters 8, 21, 27, 30) AP parameters were distributed over a wide range and had multiple peaks, revealing multiple sub-populations or a spectrum of cells. In other clusters (e.g. cluster 7), while distributions for some AP parameters (APD_{80}, APD_{30} and fractional repolarization) were relatively narrow, much wider distributions were found in triangulation. Thus, AP variability presents differently for different AP parameters. Therefore differences in subpopulation identification may be expected when a single AP parameter (such as APD_{80}) is used compared to when multiple AP parameters, or the entire AP waveform is used.

Table 2.1 Variability of AP parameters within individual and among all 32 clusters paced at 90 bpm

	APD_{30}	APD_{80}	Triangulation	Fractional repolarization
Individual Means	46 to 188 ms	85 to 257 ms	45 to 117 ms	0.27 to 0.51
Overall Mean	85 ms	137 ms	70 ms	0.41
Individual SDs	4.3 to 30 ms	6.5 to 34 ms	4.8 to 58 ms	0.03 to 0.11
Overall SD	33 ms	41 ms	24 ms	0.09

To further investigate the potential subpopulations among these cardiac cell clusters, different grouping strategies were applied to the dataset and compared against each other. Starting with APD_{80}, two Gaussian distributions were fitted to the overall distribution of the entire population, and the crossover value was used as a threshold that divided APs into two groups, namely groups of long or short AP, respectively (Fig. 2.4A). The average action potentials from the two groups are shown in Fig. 2.4D. Another action potential parameter, APD_{30} was then added to the analysis. Using principal component

(**PC**) analysis, the linear combination of APD_{80} and APD_{30} that accounted for most of the variability in the population was identified, and its distribution is shown in Fig. 2.4B. By fitting two Gaussian distributions and using the crossover value, the APs were again divided into two groups, and the average AP from each group is shown in Fig. 2.4E. In a third approach, an automated unsupervised algorithm was used to provide an unbiased grouping of APs based on their wave shapes across the entire cluster population. Fig. 2.4C shows the grouping results displayed in terms of APD_{80} and color-coded by the group assignment. Only a small fraction of the action potentials (in light blue) were labeled as different from the bulk of the population, leading to a very different result than those using AP parameters alone (Fig. 2.4A and 2.4B). The average APs from the two groups identified by waveform analysis are shown in Fig. 2.4F. Compared with the average APs using AP parameter analysis (Fig. 2.4D and 2.4E), these had greater differences in morphology (Fig. 2.4F), with one group having a shorter AP with more triangular profile, and the other group having a longer AP and a longer plateau phase. Differences among the three grouping methods can be visualized in the joint distribution of measured APD_{30} and APD_{80} (Fig. 2.4G). Here, dashed lines have been drawn corresponding to decision boundaries between the two groups determined by the analysis of: (1) APD_{80} only, (2) APD_{80} + APD_{30} PC, and (3) entire waveform. While the APD_{80}-only method always grouped cells with similar APD_{80} values together, the variability in their APD_{30} (as indicated by the vertical spread in the joint distribution) resulted in AP groups that could include very different AP shapes. The inclusion of APD_{30} introduced a tilt to the threshold line (compare lines 1 and 2), indicating the contribution of both parameters to the subtype identification. To quantify the distinction between groups, the Davies-Bouldin Index (Fig. 2.4H) was calculated, which

compares within-group tightness against between-group separations, such that lower DBI indicates better clustering (tighter groups and/or larger separations). DBI was lower for groups identified by waveform analysis (0.75) than when groups were identified by APD_{80}-threshold (0.93) or PCA (0.93) (Fig. 2.4H).

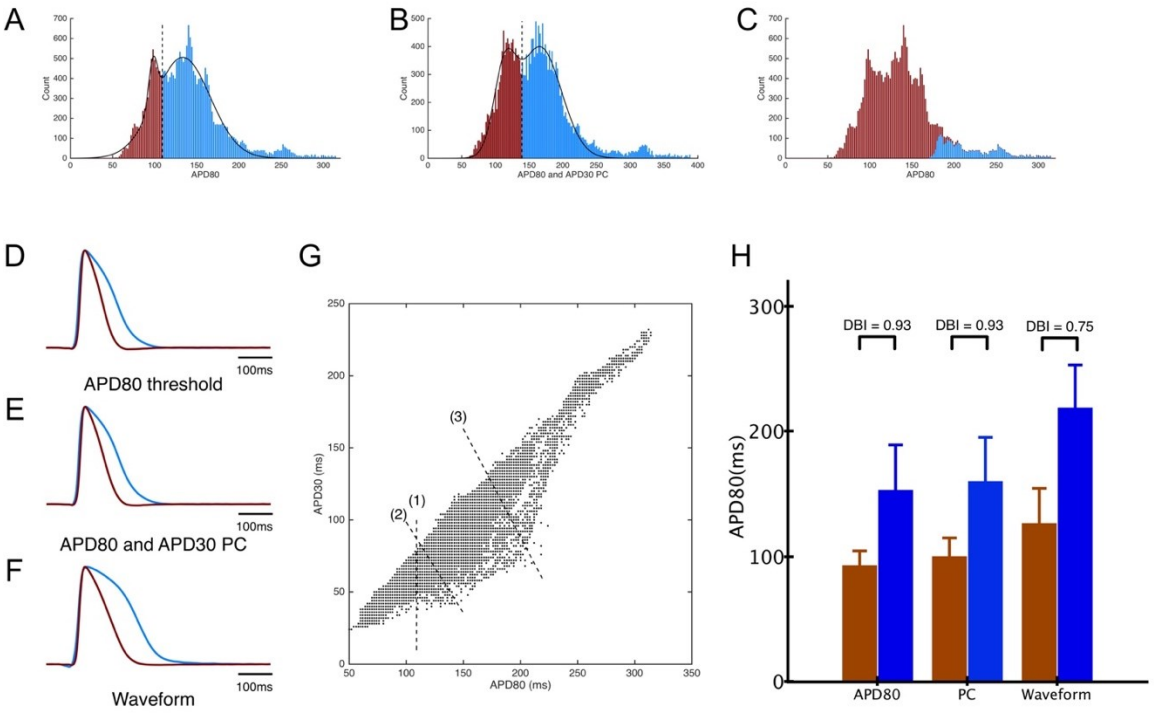

Figure 2.4 Comparison of grouping methods. (**A**) Histogram of APD_{80} from all recording sites from 32 clusters. Solid lines show fits of the data by two Gaussian curves, and dashed line indicates threshold used to divide groups of APs (shown in brown and blue). (**B**) Histogram of the principal component (PC), which is a linear combination of APD_{80} and APD_{30}. Solid lines show fits of the PC data by two Gaussian distributions, and dashed line indicates threshold used to divide groups of APs (shown in brown and blue). (**C**) Histogram of APD_{80} with waveform-based grouping, with colors showing different groups. Stacking of different colors indicate overlap in APD_{80} parameters between groups. (**D-F**) Average AP traces obtained by grouping APs based on APD_{80} threshold, PC of APD_{30} and APD_{80}, and waveform analysis, respectively. (**G**) Scatter plot of APD_{80} and APD_{30} for all recorded APs. Dashed lines represent linear classification boundaries according to (1) threshold using APD_{80}, (2) threshold using the principal component, which is a linear combination of APD_{30} and APD_{80} and (3) waveform analysis. (**H**) Comparison of APD_{80} between groups for the three different grouping methods. Colored bars correspond to groups of APs shown in (A-C). Waveform analysis resulted in groups with the most distinct AP differences, as indicated by the lowest DBI value.

Differences in the outcomes of the parameter and waveform analyses are especially apparent in comparing APs within individual clusters (e.g, clusters 7 and 27 in Fig. 2.5). APD_{80} maps (Fig. 2.5A) showed considerable variability between the two clusters, reflecting differences among the AP waveforms (Fig. 2.5B). Among the 4 APs shown, one had short duration with rapid repolarization (a), one had a short duration with a slow repolarization tail at the end of the AP (b), one was very triangular (c) and the last had a long duration with rapid repolarization (d). Different groupings were obtained with the single parameter analysis (here, being APD_{80}) compared with the waveform analysis. APD_{80} analysis grouped APs b and c with AP d, whereas waveform analysis grouped these APs with AP a. The limitations of single parameter analysis are also illustrated for APs having the same APD_{80} (Fig. 2.5C) but drastically different morphology. Analysis in terms of other parameters (such as APD_{30} in Fig. 2.5D) also encounter morphological differences. Only when both APD_{80} and APD_{30} were used together, were the morphological differences greatly reduced (Fig. 2.5E). Waveform analysis was successful in separating these APs into different groups. Furthermore, the slower repolarization and more triangulated shapes in APs b-c could be captured by analyzing all of the APs as 3 groups, whereupon APs b-c were identified as belonging to the third group.

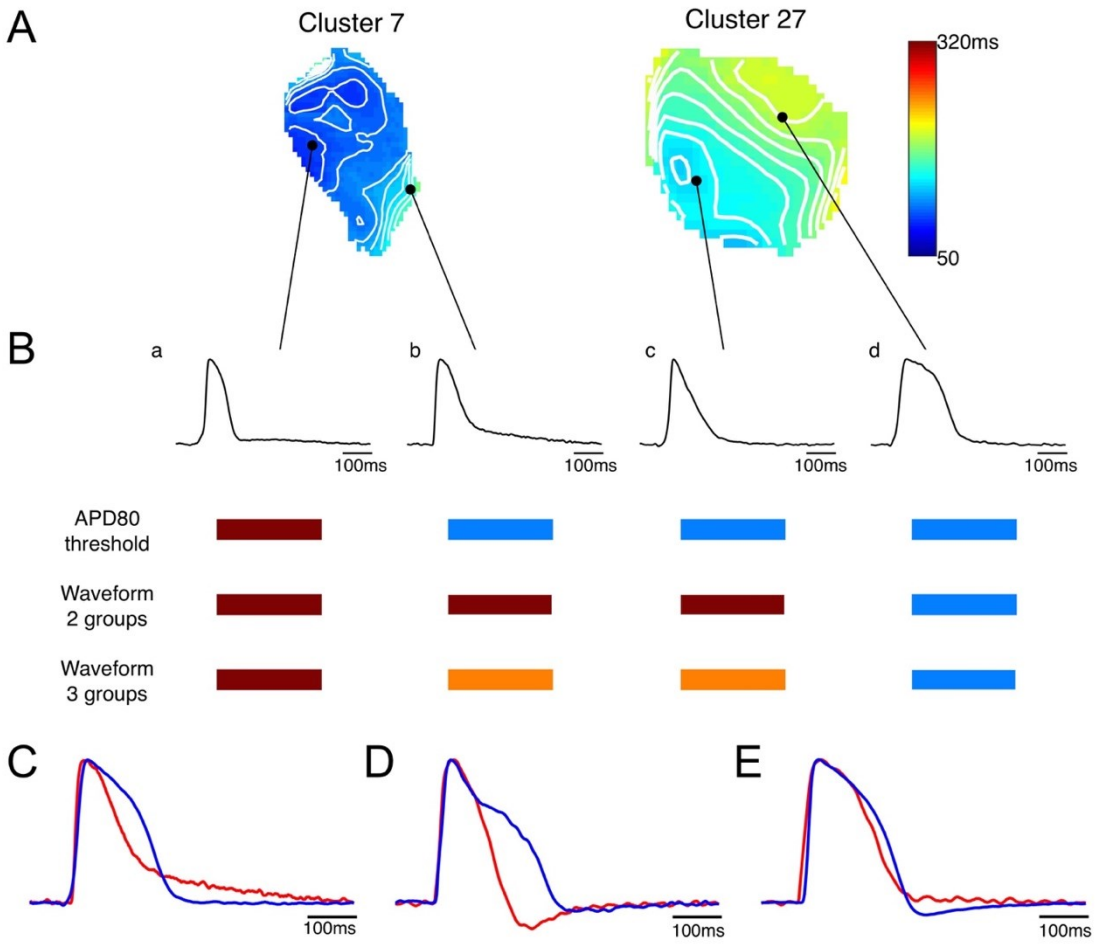

Figure 2.5 Comparison between grouping by single AP parameter (APD_{80}) and by waveform analysis. (**A**) APD_{80} map of two clusters. (**B**) APs recorded from locations indicated by black dots in (A), showing significant differences in AP morphology. Grouping results using different methods are shown as color-coded bars below. APs having the same APD_{80} (**C**) or APD_{30} (**D**) can have very different morphology. (**E**) APs having both same APD_{80} and APD_{30} have similar shapes.

The analysis of spatial heterogeneity was then expanded to two other metrics of AP shape: triangulation and fractional repolarization. Five representative clusters are shown in Fig. 2.6 (rows 1-4 for 4 total AP parameters, one cluster per column). In some cases (cluster 4), APD_{30}, APD_{80}, fractional repolarization and triangulation were uniform across the cluster, indicating a single population of cells. In other cases (clusters 9, 27) the 4 AP parameters had similar patterns showing two distinct regions (e.g, on the left and right sides

of cluster 9, and lower left and upper right sides of cluster 27) indicative of two subpopulations, although for cluster 27 the regions were not entirely concordant across parameters. In still other cases (cluster 7, 24) the patterns for the AP parameters were dissimilar. By using the automated algorithm with the entire AP waveform, cells among the clusters were separated into 2 groups, with spatial patterns as shown (Fig. 2.6, second to last row). The 2-group analysis revealed that 14 of 32 clusters contained cells from different groups. This coexistence of cells from different groups is more notable with automated 3-group analysis (Fig. 2.6, last row), where 17 clusters had cells from all 3 groups, 12 clusters had cells from 2 different groups, and only 3 clusters had cells from a single (and different) group. Furthermore, cells belonging to different groups were not intermingled and tended to occupy separate areas within a cluster (Fig. 2.6, last two rows) even though spatial information was not incorporated into the grouping algorithm. Separate groups could be identified even in clusters where the patterns of APD parameters were discordant (e.g. cluster 24). Additionally, the analysis described in this chapter resulted in the identification of individual AP phenotypes that were common to multiple clusters (e.g., group 3 in clusters 9, 24, and 27). Note, however, that the increased number of groups was accompanied by a higher DBI value (0.91 for 3 groups vs. 0.75 for 2 groups), suggesting that 2 groups better describe this particular population of action potentials.

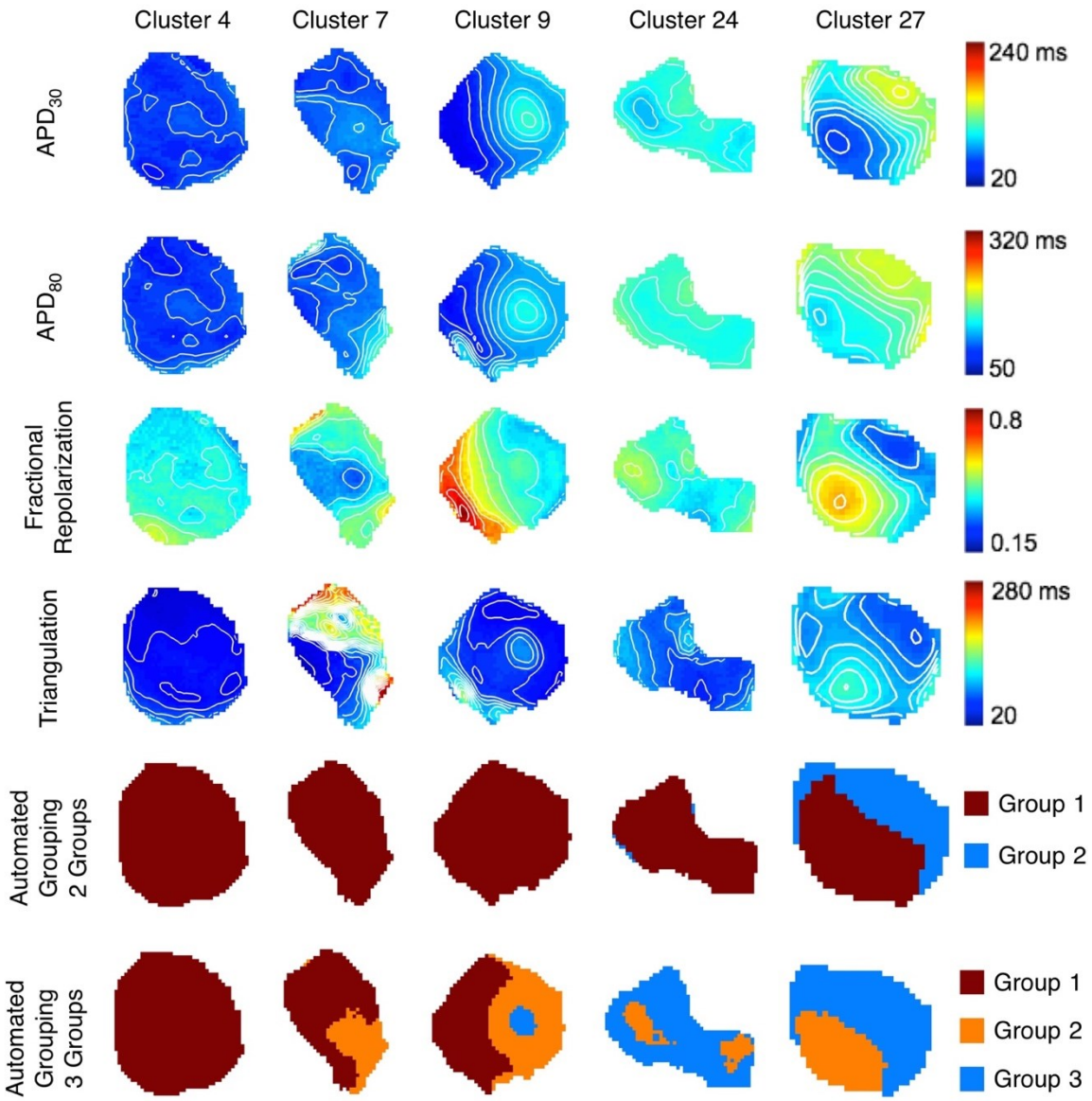

Figure 2.6 Spatial maps of different AP parameters or groups for five different cell clusters. Top four rows: Spatial distributions of APD_{30}, APD_{80}, fractional repolarization, and triangulation in the clusters. Iso-parameter contours have 10 ms spacing for APD_{30}, APD_{80} and triangulation and 0.05 spacing for fractional repolarization. Maps in the same row share same color bar. Bottom two rows: Grouping resulting from the automated algorithm and assumption of 2 (second to last row) or 3 (last row) groups. Colors signify different groups assigned by the algorithm. Columns: clusters 4, 7, 9, 24 and 27.

For visualization and discussion purposes, all APs were plotted as scatter plots of joint distributions of pairs of AP parameters, along with their group labels by waveform analysis in colors (Fig. 2.7). Although paced at the same rate, the entire set of APs encompassed a large area in all 2D spaces of AP parameter pairs, indicating a high degree of variability. When APs were divided into two groups, they occupied relatively distinct regions in all 2D spaces. Linear boundaries were determined by SVMs within each 2D space, and shown as dashed lines. The degree of overlap of the two groups was defined as the total percentage of APs of each group located outside the boundary of their respective groups, and ranged from 0.9% to 8.1% across all of the 2D spaces, indicating the influence of features of AP shape not captured by just a pair of AP parameters. In general, the overlap in the 2D spaces with AP duration parameters (Fig. 2.7A) was smaller than that in 2D spaces with triangulation and fractional repolarization parameters (Fig. 2.7F), suggesting that AP duration parameters have a stronger contribution in grouping than triangulation or fractional repolarization.

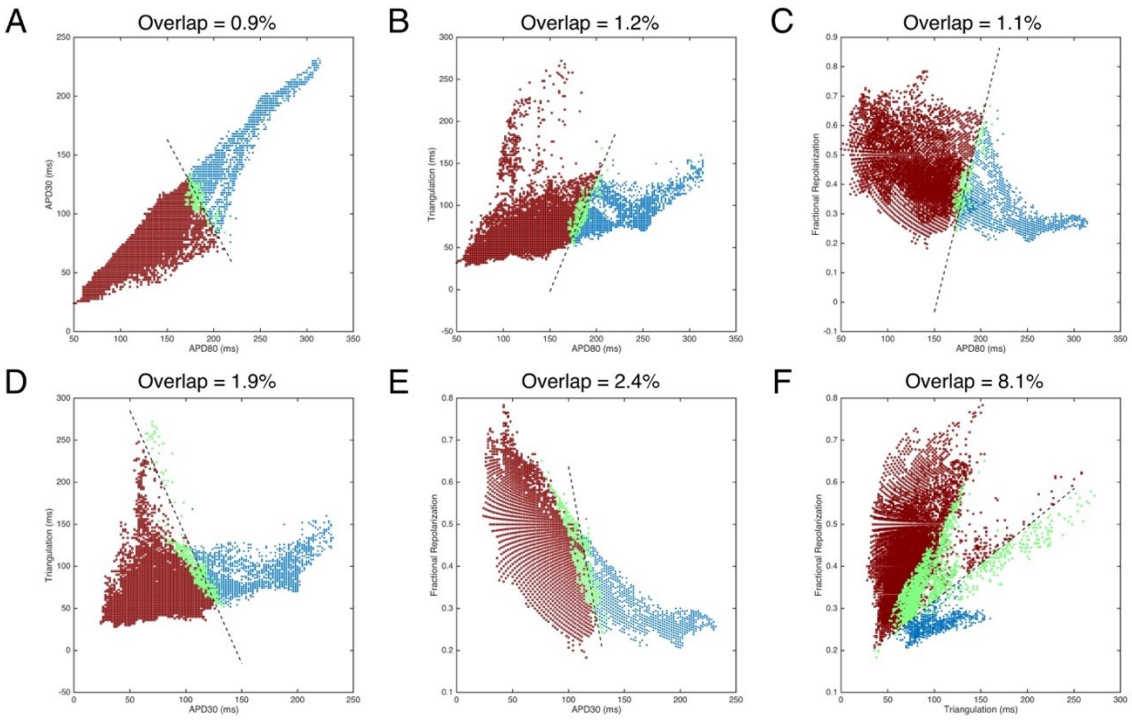

Figure 2.7 Pairwise scatter plots of individual AP parameters for all recorded APs, color-coded by grouping results defined by waveform analysis. Dashed lines indicate linear decision boundaries separating the two groups in the parameter space, derived by support vector machines. APs of each group falling on the opposite side of the boundary (the overlaps, highlighted in green) were quantified as percentage of the total APs and are given above each panel.

Rate dependency

Depending on the cluster, electrical pacing could stimulate APs up to 330 bpm while maintaining 1:1 capture, allowing the study of the rate-dependence of paced APs (Fig. 2.2B) and whether rate-dependency could be an additional means by which different sub-populations (phenotypes) of cells could be discriminated. In a cluster having two regions with different AP durations (cluster 26), electrical pacing was applied from 90 to 180 bpm in 30 bpm increments. While all recording sites (n=585) in this cluster had rate-dependent shortening of APD_{80}, the rate-dependencies of fractional repolarization varied greatly, being positive (increased fractional repolarization with increased rate) in some

regions (n=180) and negative in others (n=405). Two representative recordings from this cluster and their corresponding APD_{80} and fractional repolarization rate-dependencies are shown in Fig. 2.8. The differences in rate-dependencies suggest that the use of multiple pacing rates may further assist in identifying phenotypic differences.

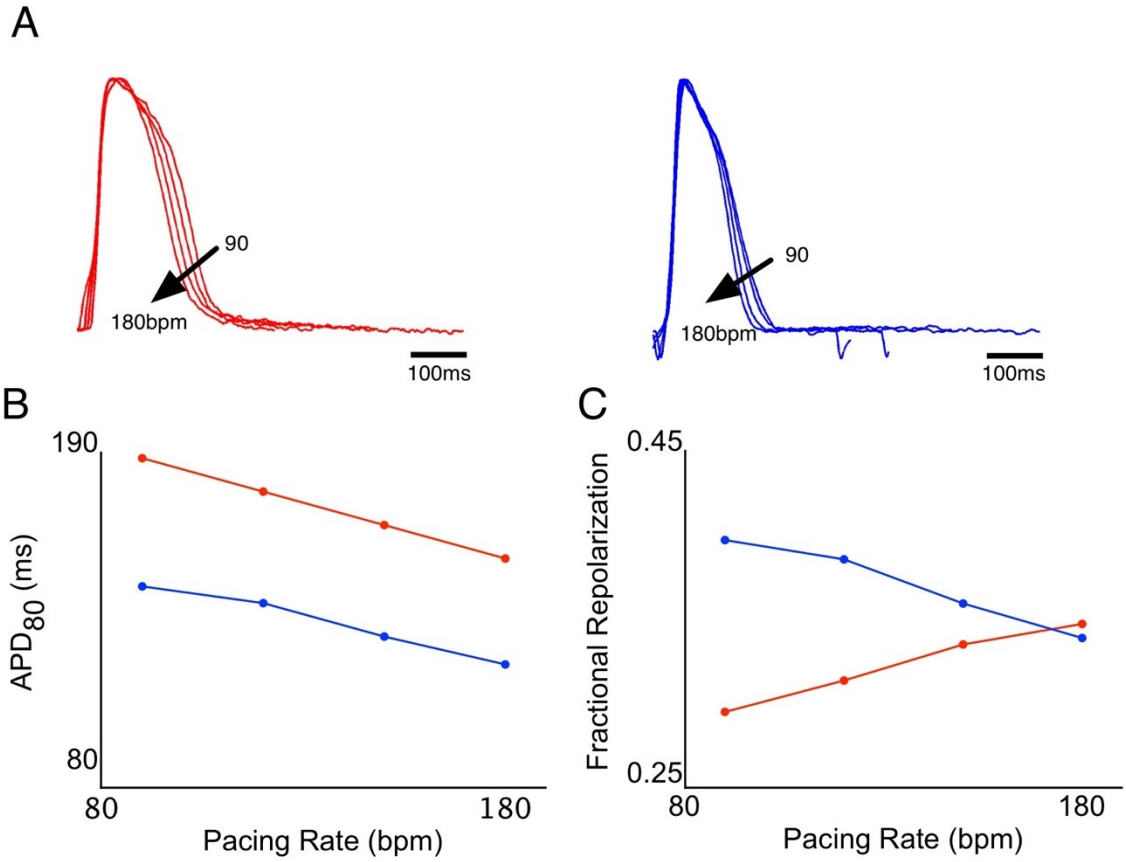

Figure 2.8 Rate-dependence of action potentials in a cell cluster (cluster 26). (**A**) Action potentials recorded from two different locations in the cluster having long (left, red traces) and short (right, blue traces) APs, at 90, 120, 150 and 180 bpm pacing. (**B**) Rate-dependence of APD_{80} at the two recording sites. (**C**) Rate-dependence of fractional repolarization at the two recording sites.

2.3.2 Action potential variability in hiPSC-CM monolayers

General electrophysiological properties of hiPSC-CM monolayers

A PDMS stencil was used to restrict the growth area of hiPSC-CM monolayers (Fig. 2.9A) and effectively control the size and shape of the monolayers. Approximately two days after monolayer plating, spontaneous beating was observed across the monolayers, with beating often originating from different locations across the monolayer. These asynchronous spontaneous activities gradually become synchronized over time in culture, indicating formation of a functional syncytium.

When electrical point pacing was applied at the edge of the monolayer, smoothly propagating action potentials could be initiated across the monolayer. A representative activation map is shown in Fig. 2.9B, where the pacing was applied at the upper left corner of the monolayer. The average conduction velocity measured at 1000 ms cycle length for WT11 hiPSC-CM monolayers was 12.1±3.4cm/s (n=3 monolayers), which is substantially slower than typical conduction velocities measured in adult myocardium (41.4±3.4cm/s, transmural) (Glukhov et al., 2010). The contour lines show isochrones of activation times. Typically, a smooth propagation pattern was observed, with no significant slowing or other abnormality that may indicate conduction heterogeneity. These observations reinforce the notion that hiPSC-CM monolayers are an electrically functional syncytial model.

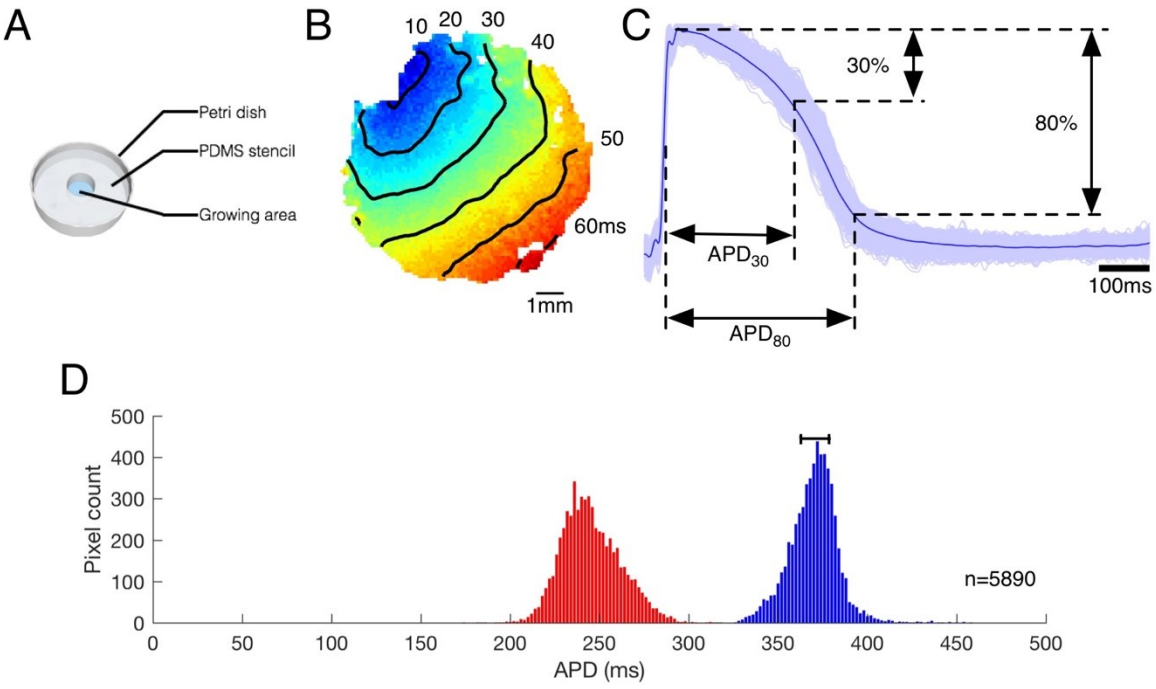

Figure 2.9 General electrophysiological properties of hiPSC-CM monolayers. (**A**) Schematic diagram of PDMS stencil used to restrict the growth area to a 10 mm diameter circle in a 35 mm dish. (**B**) Representative activation map of an hiPSC-CM monolayer when electrically paced at 1000 ms cycle length. Blue indicates regions activated at an earlier time, red indicates regions activated later. Isochrones show area activated at the same time, and are drawn at 10 ms intervals as indicated. Scale bar is 1 mm. (**C**) Action potentials recorded from the hiPSC-CM monolayer shown in B. Solid line is the action potential averaged over the entire monolayer. Shaded area is an overlay of individual action potentials recorded from each recording site of the monolayer. (**D**) APD_{80} (blue) and APD_{30} (red) histograms of this monolayer, showing 5890 recording sites. Bar on top of blue histogram indicates IQR-APD_{80}.

Action potentials recorded from different recording sites are demonstrated in Fig. 2.9C for this example monolayer. The solid line indicates the average of all action potentials recorded across the entire monolayer, representing the aggregate electrophysiology of the monolayer. The lighter traces show superimposed action potentials from 5890 individual recording sites in this monolayer, representing local electrophysiology at different sites within the monolayer. As shown in this example, action potentials recorded from individual sites deviate slightly from the average, but in general

follow the same morphology. This observation is also evident when APD_{80} and APD_{30} are used as measures of the action potentials, which is shown in Fig. 2.9D. Only a single peak was observed for both APD_{80} and APD_{30} histograms, further indicating relatively uniform action potential properties and a single electrophysiological phenotype. The variation of action potential durations was measured by the interquartile range of APD_{80} (IQR-APD_{80}). In this example, the IQR-APD_{80} was 16 ms, which was very narrow compared to the average APD_{80} of 370 ms. Similar observations of a single peak histogram for APD_{80} were observed in all other monolayers analyzed (n=9). These observations suggest only one phenotype is present in hiPSC-CM monolayer cultures.

Effect of I_{Kr} blockade on action potential variability in hiPSC-CM monolayers

The effect of ion channel blockade on action potential variability was investigated by pharmacologically blocking I_{Kr}, an important repolarizing current in the cardiomyocytes. For this purpose, E-4031, a specific I_{Kr} blocker was applied to hiPSC-CM monolayers. E-4031 induced a concentration-dependent prolongation in the average action potential of the monolayer (Fig. 2.10A). The action potential also had slower repolarization and become more triangular in morphology. The monolayers remained captured to 1000 ms cycle length electrical pacing, and no ectopic activity was observed with E-4031. For individual recording sites across the monolayer, action potentials across again deviated only slightly from the average action potential (Fig. 2.10B, lighter traces are overlays of individual APs, solid lines are average APs). The application of E-4031 did not create separation in action potential morphologies, consistent with a single phenotype even with I_{Kr} blockade. The APD_{80} histograms (Fig. 2.10C) showed a rightward shift with increasing concentration of E-4031, and a slight increase in spread in this example, but remained

having a single peak. The box plots of APD_{80} (Fig. 2.10D) also show this pattern, with concentration-dependent prolongation in APD_{80}, but only a very slight increase in APD_{80} variability When measured over multiple monolayers (n=3), IQR-APD_{80} was not affected by E-4031 in a statistically significant way (Fig. 2.10E). Further, conduction velocity remained the same with or without E-4031 (Fig. 2.10F).

Spatially, clustering of APs with similar durations was also observed in hiPSC-CM monolayers, similar to observations with hEBs (Fig. 2.6), except that a single peak in APD_{80} histogram was always observed, unlike the multiple peaks often observed in hEBs (Fig 2.3). E-4031 also did not change the clustered distribution of action potentials (Fig. 2.10G a-d). Activation maps at baseline and all E-4031 concentrations tested showed homogeneous AP propagation, with no conduction slowing or block (Fig. 2.10G e-h).

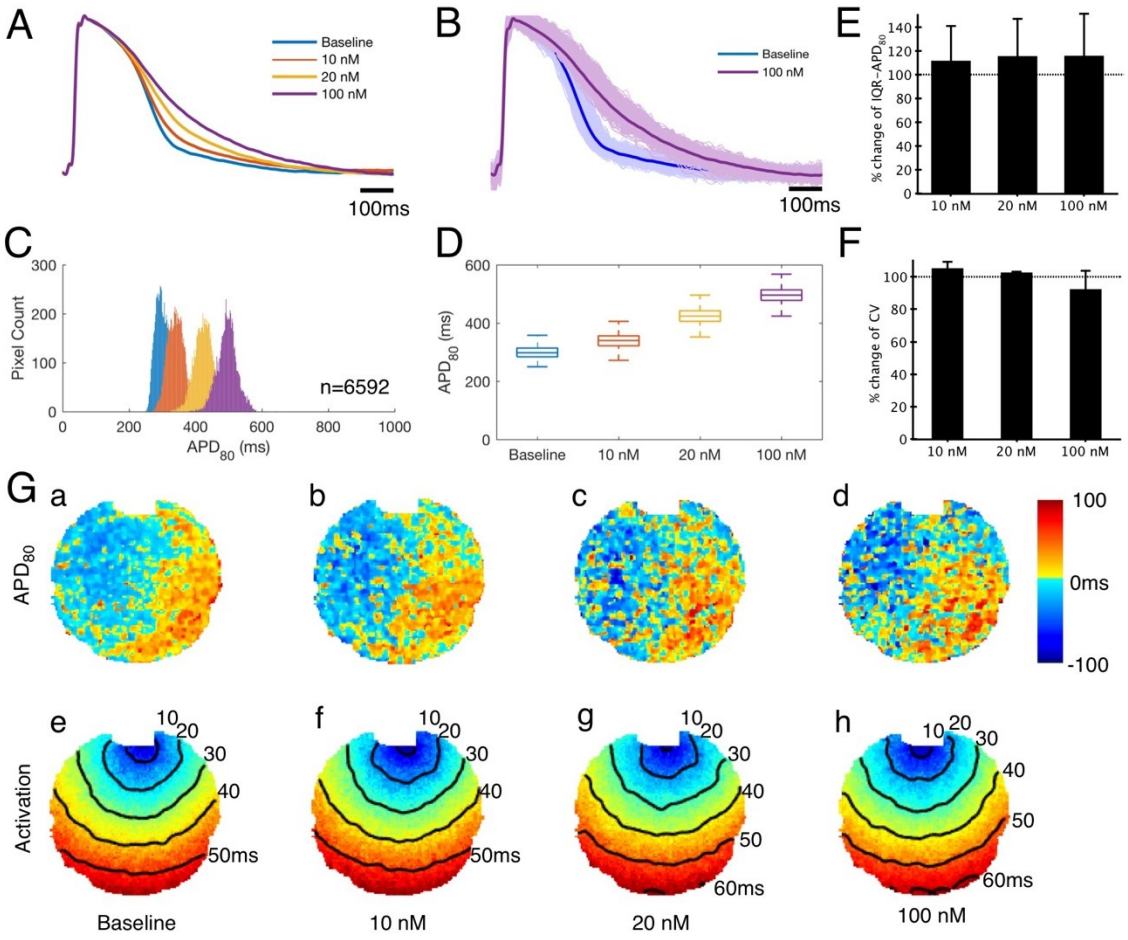

Figure 2.10 Effect of I_{Kr} blockade on action potential variability in hiPSC-CM monolayers. (**A**) Average action potential across a single hiPSC-CM monolayer, at baseline and with different concentrations of E-4031. (**B**) Average APs (solid line) and individual APs within the monolayer at baseline and with 100 nM E-4031. (**C**) APD_{80} histograms at baseline and with different concentrations of E-4031, showing 6592 recording sites. (**D**) Box blot of APD_{80} of action potentials within the same hiPSC-CM monolayer. Box indicates interquartile range, whiskers indicate 5th and 95th percentiles. (**E**) Relative change in IQR-APD_{80} in response to E-4031. (**F**) Relative change in conduction velocity in response to E-4031. (**G**) a-d. APD_{80} variability maps of an hiPSC-CM monolayer at baseline or with E-4031. Blue indicates areas with APD_{80} shorter than the median APD_{80} across the monolayer, red indicates areas with APD_{80} longer than the median. e-h. activation maps of the same monolayer at baseline or with E-4031. (E-F) n=3 monolayers, all ns compared to baseline.

Effect of acute electrical uncoupling on action potential variability in hiPSC-CM monolayers

In a syncytial monolayer, cardiomyocytes are electrically coupled through gap junctions among cells. Therefore, it is possible that electrical coupling could reduce the intrinsic AP variability by smoothing differences among neighboring APs. To test whether electrical uncoupling can reduce action potential variability, carbenoxolone (**CBX**), a gap junction blocker, was applied acutely to hiPSC-CM monolayers. I_{Kr} blockade was then repeated in the presence of CBX to investigate any additional effect on action potential variability.

Application of 50 μM CBX slightly prolonged the average action potential of the hiPSC-CM monolayer (Fig. 2.11A). The APD_{80} histogram showed a slight rightward shift in the population action potentials, but remained having a single peak (Fig. 2.11B). The IQR-APD80 did not change significantly either (Fig. 2.11D). Conduction velocity was significantly slowed with CBX, as expected with a decrease in electrical coupling (Fig. 2.11C), which is also evident in compression of the isochrone lines in the activation maps (Fig. 2.11E f-g). The spatial distribution of APD_{80} was not affected by carbenoxolone (Fig. 2.11E a-b). Further blockade of I_{Kr} by E-4031 led to a concentration-dependent prolongation of action potential that was similar to the non-CBX results. The APD_{80} histogram slightly widened but remained having a single peak and the IQR-APD_{80} did not deviate significantly from baseline (Fig. 2.11D), supporting the notion of a single predominant phenotype in the monolayer. However, in contrast to non-CBX conditions, I_{Kr} blockade with CBX led to further concentration-dependent slowing in conduction (Fig.

2.11C). On the other hand, despite conduction velocity slowing, there was no change in the pattern of action potential propagation (Fig. 2.11E f-j).

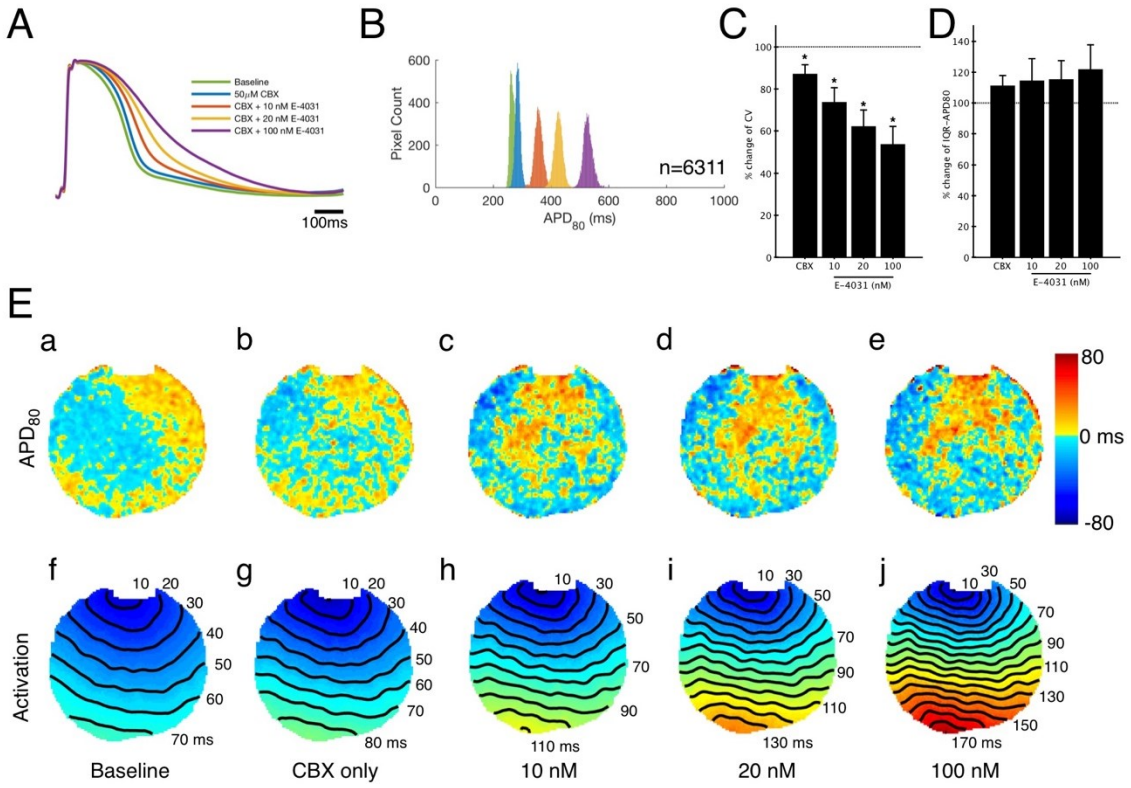

Figure 2.11 Effect of acute electrical uncoupling on action potential variability. (**A**) Average action potentials of hiPSC-CM monolayer with CBX and E-4031. (**B**) APD_{80} histogram of action potentials from a total of 6311 recording sites within the monolayer. (**C**) Relative change in conduction velocity in response to CBX and E-4031. (**D**) Relative change in IQR-APD_{80} in response to CBX and E-4031. (**E**) a-e. APD_{80} maps at different CBX concentrations; blue indicates regions with APD_{80} shorter than the median, red indicates regions with APD_{80} longer than the median. f-j. activation maps of the monolayer at different CBX concentrations. (C-D) n=5 monolayers, * indicate significant ($p<0.05$) compared to baseline (100%).

Comparison between in-house derived and commercially available hiPSC-CMs

Action potential variability was compared between monolayer cultures of in-house differentiated WT11 hiPSC-CMs and commercially available Axiogenesis Cor.4U cardiomyocytes. The Cor.4U cells are purified human iPSC-derived cardiomyocytes with approximate composition of 60%-20%-20% ventricular-like, atrial-like and nodal-like

phenotypes identified by patch clamp of single cells (Kettenhofen et al., 2014). However, when cultured as monolayers the cells reveal just a single predominant electrophysiological phenotype. The implication of a single phenotype within hiPSC-CM monolayers on their drug responses is further discussed in **Chapter 4**.

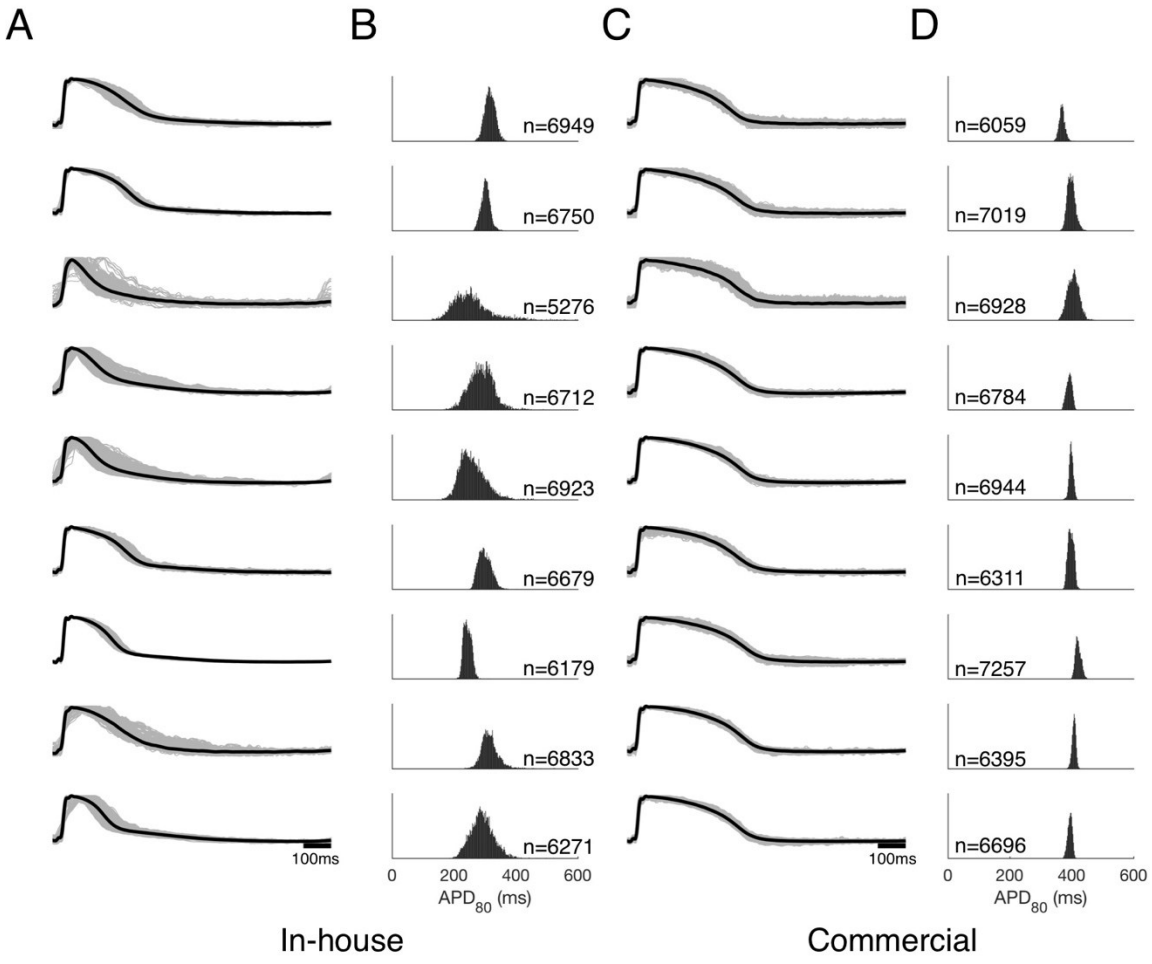

Figure 2.12 Comparison of action potential variability between monolayers consisting of in-house or commercial hiPSC-CMs. (**A**) Action potentials recorded from multiple in-house monolayers. (**B**) APD_{80} histograms of corresponding monolayers in A. (**C**) Action potentials recorded from multiple commercial monolayers. (**D**) APD_{80} histograms of corresponding monolayers in C. (**B,D**) number of recording sites within each monolayer are as indicated.

Action potentials recorded from both in-house derived iPSC-CM monolayers (Fig. 2.12A) and Cor.4U monolayers (Fig. 2.12C) were always uniform within individual

monolayers, with only small variations. This is also evident in the APD_{80} histograms (Fig. 2.12B for in-house monolayers and Fig. 2.12D for Cor.4U monolayers). However, it is also worth noting that, overall the action potentials were more uniform across multiple Cor.4U monolayers than across multiple in-house derived monolayers, presumably due to the more stringent quality control in the production of the Cor.4U cells. The in-house monolayers had an IQR-APD_{80} of 39±19 ms (mean±SD) and an inter-monolayer SD of average APD_{80} of 26 ms (n=9), while the Cor.4U monolayers had an IQR-APD_{80} of 13±5 ms and an inter-monolayer SD of average APD_{80} of 14ms (n=9). For comparison, the hEBs had an IQR-APD_{80} of 23±12 ms (mean±SD) and an inter-hEB SD of average APD_{80} of 37 ms. To account for the differences in pacing rates between hEB and monolayer experiments (90 bpm for hEBs and 60 bpm for monolayers), IQR-APD_{80} was normalized to the average APD_{80}, and the ratio of IQR-APD_{80} to APD_{80} was 0.17±0.10, 0.14±0.07 and 0.03±0.01 for hEBs, in-house monolayers and Cor.4U monolayers, respectively.

2.4 Discussion

Manifestation of action potential variability in cluster and monolayer models

Electrophysiological variability observed in hPSC-derived cardiomyocytes is an undesired property for many *in vitro* applications. For example, in regenerative medicine, heterogeneous action potentials can be problematic as they can create a proarrhythmic substrate. The nodal-like cells may also become ectopic pacing sites if integrated in host tissue. Another example is in *in vitro* testing of drug responses using hPSC-derived cardiomyocytes. Variability in electrophysiology creates a heterogeneous baseline which

makes interpreting drug responses more difficult and less reliable. The action potentials of hPSC-CMs are generally recognized as heterogeneous and not fully like adult phenotypes (Blazeski et al., 2012b; 2012a), but to date the largest population in which this variability has been studied was 134 cells (López-Redondo et al., 2016). The results in this chapter characterized AP variability in two different *in vitro* hPSC-CM models: small clusters of hESC-derived cardiomyocytes, which had 722±252 (n = 32) recording sites with 16 μm resolution and large monolayers of hiPSC-derived cardiomyocytes, which had 6609±464 (n = 18) recording sites with 100 μm resolution.

Small clusters of hESC-CMs provide a platform to investigate how electrical variability manifests both within the same cluster and among clusters from the same differentiation batch. This can help in the understanding of the smallest spatial scale at which action potential variability becomes significant. Prior studies using microelectrode impalements of hEBs showed that APs differed substantially among different hEBs but were mostly similar within individual clusters (He et al., 2003; Jonsson et al., 2010), although the sample size obtained per cluster was small and limited by the experimental methods. However, the large population analyses in this chapter show that APs vary over a wide range across hEBs and over a smaller, but still substantial range within hEBs. Further, although numerous research groups have reported percentages of nodal-like, atrial-like and ventricular-like cells at a stage of differentiation similar to the clusters studied in this chapter (20-24 days) (Fu et al., 2011; Lee et al., 2011; Lieu et al., 2013; Moore et al., 2008), the results here demonstrate that different phenotypes are difficult to distinguish for at least two reasons: 1) individual parameters are insufficient to divide populations of APs into different groups, since APs with similar parameter values (such as

APD_{80}) could have very different morphology indicative of different phenotypes, and 2) the wide range and continuous variability of APs make it extremely difficult to subjectively determine cut-offs between groups. However, by using an automated grouping algorithm that utilized the entire AP waveform shape, the AP dataset could be objectively separated into 2 or 3 maximally separated groups.

Cardiac cell clusters derived from hEBs are self-assembled, three-dimensional aggregates. This three-dimensional organization provides a natually formed microenvironment for hPSC-derived cardiomyocytes, allowing them to grow and remodel their surrounding extracellular matrix, to undergo paracrine and autocrine signaling, and to contract against a compliant mechanical load. However, the microenvironments experienced by cells in each cluster are independent of one another and not necessarily the same. The hEB-based differentiation protocol (Burridge et al., 2011; Burridge and Zambidis, 2013) used here has high efficiency, so that a large number of beating hEBs can be generated within a single differentiation batch sufficient for studies of variability introduced under culture conditions. Some sources of variability were managed. Optical mapping was performed on beating cell clusters within a narrow time window, 21-24 days after initiation of differentiation. Fixed-rate pacing was used so that APs could be compared at the same beat rate. However, there remained several uncontrolled experimental variables. Although similar numbers of hESCs were seeded to form hEBs, the ensuing hEBs still had different sizes, shapes and beat rates, which could influence the differentiation process. In addition, the beating cardiac cell clusters that were mechanically dissected from the hEBs may represent only a subset of all of the cardiomyocytes that were present. Also, the uncontrolled amount of nonmyocytes in the cell aggregates can influence

the maturation of the embedded hESC-CMs (Kim et al., 2010a). The action potential variability observed within and across hEBs is a combined result of these environmental factors, and reflects the adaptability of hPSC-CMs and their electrophysiology to the local microenvironment.

High-resolution measurements of early differentiated clusters suggest that a relatively broad distribution of APs is present within the clusters (Fig. 2.3), although not as broad as across the entire set of 32 clusters that was studied. In many, but not all clusters, a histogram of APD_{80} that was either narrow or else wide with multiple peaks was observed, suggestive of one or multiple predominant phenotypes. APD_{30}, triangulation and fractional repolarization are other ways to quantify the plateau and repolarization phases of the AP, which in turn are manifestations of the underlying ion currents which have differing temporal and voltage-dependent kinetics (Shah et al., 2005). APD_{30} is a rough measure of plateau duration, while APD_{80} is a measure of the combined plateau and repolarization durations. Triangulation (Hondeghem et al., 2001) is roughly the duration of phase 3 repolarization, and is considered to be proarrhythmic when prolonged. Fractional repolarization is the fraction of the total APD involved with phase 3 repolarization. This parameter is also akin to the comparison between plateau (duration between APD_{30} and APD_{40}) and repolarization (duration between APD_{70} and APD_{80}) phases defined by others to distinguish between ventricular-like cells and atrial-like cells (Ma et al., 2011). In this study, the spatial patterns of groupings based on APD_{80}, APD_{30}, triangulation and fractional repolarization were usually but not always concordant with one another (Fig. 2.6), raising the question of which parameter(s) is most important for phenotype identification.

Given that variability exists within and among small sized, independent groups of hPSC-CMs, it is also important to know if they retain their variable action potential properties when allowed to interact and form a larger syncytium. In fact, a recent study has demonstrated that geometric shape and size can affect action potentials in hiPSC-CMs, where larger aggregates of cells tend to have more mature electrical and calcium dynamics (Werley et al., 2017), although the largest island tested was 1 mm × 1 mm. The larger monolayers used in this chapter provide a model for further investigating this question. Individual hiPSC-CMs are heterogeneous and comprised of all three phenotypes, as is the case for Axiogenesis Cor.4U cardiomyocytes, which have been characterized by the manufacturer to have a mixed population of nodal-, atrial- and ventricular-like cells at expected fractions of 20%, 20% and 60% respectively. However, the action potentials within individual monolayers in fact had similar shapes, rather than distinctly different shapes, suggesting that the cell monolayers, despite being much larger in dimension than hEBs, promote the convergence of the hiPSC-CMs to a single predominant electrophysiological phenotype. This phenotype convergence is evident in two ways. First, monolayers had a lower inter-sample variability than hEBs, which is indicated by the lower SD of average APD_{80} (26 ms and 14 ms for in-house and Cor.4U monolayers, respectively, compared to 37 ms for hEBs), and second, variability within each sample, as measured by the ratio of IQR-APD_{80} to APD_{80} to account for pacing rate differences, was also lower in in-house and Cor.4U monolayers than in hEBs (0.14 ± 0.07 and 0.03 ± 0.01 compared to 0.17 ± 0.10). It is worth noting that the size of the hEBs is much smaller than the monolayers (hundreds of microns vs. 1 cm diameter), and despite the higher spatial resolution used for hEBs (16 μm/pixel vs. 100 μm/pixel for monolayers), the number of recording sites within

hEBs was still much smaller than within monolayers (722±252 vs. 6609±464, respectively). The hEBs were also paced at a higher rate of 90 bpm compared to 60 bpm for the monolayers. These factors could contribute to an underestimation of variability observed in hEBs.

Unlike spontaneously-formed hEBs, monolayers provide a more consistent microenvironment during culture. Cardiomyocytes in monolayers have more uniform access to nutrients and growth factors present in the culture medium, experience similar biomechanical stimuli from the culture substrate to which they are attached, and once electrically coupled, have the same spontaneous activity and therefore bioelectrical signals. Individually, these environmental factors have been shown to affect the electrophysiology in hPSC-CMs (Zhu et al., 2014). Therefore, the uniformity observed in monolayers is possibly a combined result of uniformity of these environmental factors.

The action potential is an aggregate measurement of hPSC-CM electrophysiology, and is generated by the coordinated activity of multiple ion currents. Different ion current compositions can, however, result in a similar action potential waveform. If this is the case, selective blockade of individual ion currents may reveal an underlying ion current heterogeneity in a population of cells by disturbing their balance in a differential manner, changing the action potential in different, revealing ways. However, the monolayer response to I_{Kr} blockade with E-4031 suggests the contrary. I_{Kr} is one of the most important currents that activates during repolarization of the action potential, and strongly affects action potential morphology and duration. However, blockade of this important current did not lead to separation of the APD_{80} histogram into multiple peaks, separation of regions of the monolayer into different phenotypes, or even a significant increase in AP variability as

quantified by IQR-APD_{80}. These observations suggest that the similarity in action potentials within hiPSC-CM monolayers reflects a uniformity in ion current composition (at least, for I_{Kr}) across the monolayer, which is further indicative of a single electrophysiological phenotype.

Gap junctions connecting cardiomyocytes can also make action potentials appear to be similar through cell-cell electrotonic coupling. However, decrease of electrical coupling by carbenoxolone did not lead to phenotype separation nor increase in action potential variability, suggesting an electrical smoothing effect was not responsible for the similarity in action potentials. It is worth pointing out that although carbenoxolone only reduced conduction velocity by a small percentage, this is reflective of a much larger reduction in intercellular coupling (Kléber and Rudy, 2004). With reduced electrical coupling, E-4031 produced a dramatic reduction in conduction velocity while it did not with normal electrical coupling. This result can be explained as follows. The prolongation of action potential by E-4031 reduced the diastolic interval following the action potential, thereby impairing excitability and slowing down conduction of the next action potential. With normal electrical coupling, this reduction in excitability was insufficient to impair conduction because of conduction reserve in the tissue (van Rijen et al., 2006), but with reduction of electrical coupling by CBX, conduction reserve is diminished, thereby augmenting the slowing effects of E-4031.

In hEBs, clustering of cells having similar action potential phenotypes was observed. Similarly, this was also the case for monolayers. E-4031 or CBX did not significantly change the local clustering of electrophysiologically similar cells, except at a high concentration of E-4031 where there was a slight dissipation of clustering towards an

intermixed distribution. This can be explained if the electrophysiological variability underlying clustering is due in large part to I_{Kr}, which becomes nearly completely blocked at the high concentration of E-4031. Similar to small clusters, hPSC-CM monolayers also contain cardiomyocytes that are electrically and mechanically coupled, which are potential pathways to modulate the electrophysiology of individual cells that could work over long range distances of multiple cell dimensions. Therefore, monolayer experiments can provide insight on how does this homogenizing effect extend to much larger physical dimensions when cells are cultured as larger scale monolayers.

The main difference between in-house derived hiPSC-CMs and commercially available cells lies in their quality control. Industrial production of hiPSC-CMs requires higher scalability and reproducibility than cardiac differentiations in a research environment. Good Manufacturing Practice (**GMP**) compatibility is also taken into consideration for commercial hiPSC-CMs, as it is a requirement for pharmaceutical and clinical applications. The differences in practices can affect the quality of hiPSC-CMs in several ways. For example, despite generally high differentiation efficiency with the monolayer-based protocol, there is inevitably some variable amount of non-myocytes left in the in-house hiPSC-CM differentiations that contributes to the variability in experimental observations, which is not strictly controlled. This is not the case of Cor.4U hiPSC-CMs, where purification methods are used to ensure near 100% cardiomyocytes. In addition, the consistency in culture conditions is also subject to more variability for in-house production of hiPSC-CMs than for commercial production, such as the batch-to-batch variability in research-only grade reagents, the more frequent access to the cells in the incubator which could disturb the culture environment, and the variability in culture

handling among researchers. The combination of the above-mentioned factors, along with others, could explain the observation that commercial cells are much more uniform in electrophysiology, both within the monolayer, and across monolayers compared to in-house hiPSC-CM monolayers.

Phenotype identification in hPSC-CMs

The gold standard for identifying phenotypes of cardiomyocytes derived from hPSCs is still under debate (Kane and Terracciano, 2017). The most accepted method is comparison of the immature phenotype found in hPSC-CMs with that of mature human cardiomyocytes. This include features such as molecular cellular markers, cellular morphological characteristics and action potential properties. However, molecular cellular markers are currently limited primarily to MLC2v or IRX-4 for the ventricular subtype (Karakikes et al., 2014; Otsuji et al., 2010; Zhang et al., 2011) and cannot be used on live cells. In practice, classification by AP morphology is still the most widely adopted method by which cardiomyocyte phenotypes have been assessed by microelectrode or optical recordings (Ardehali et al., 2013; Du et al., 2015; Fu et al., 2011; Lee et al., 2011; Leyton-Mange et al., 2014; Tohyama et al., 2013; Wang et al., 2011), although there are also questions on the utility of this approach (Bett et al., 2016; Du et al., 2015; Giles and Noble, 2016; Kane et al., 2016). Major subtypes of hPSC-CMs (nodal-like, atrial-like, ventricular-like) have most often been identified subjectively by the similarity of their AP shapes to those of the adult phenotypes. Only a few studies specified quantitative criteria for classification in terms of AP parameters, including APD_{90} (Peng et al., 2010), combination of APD_{90} and beat rate (Jonsson et al., 2010), ratio of APDs (Chan et al., 2013; Ma et al., 2011), and a combination of AP amplitude, upstroke velocity, APD_{50} and APD_{90} (Fu et al.,

2011; Lieu et al., 2013). The hEB classification results of this chapter show that grouping by histogram analysis of single parameters does not assure consistent AP morphology; action potentials having the same APD_{80} or APD_{30} can have differing AP shapes reflecting different phenotypes (Fig. 2.5C and 2.5D). Increased numbers of parameters result in improved grouping, with the ultimate representation being the entire waveshape.

Analysis of the entire data set of APs (recorded across 32 hEBs) by an automated machine learning algorithm (Gorospe et al., 2014) divided the APs into different groups based on their waveshape and similarity to one another. This method also produced the most distinctive differences in AP waveforms between groups (Fig. 2.4F). Within individual hEBs the groups occupied separate spatial regions rather than being intermixed, even though the automated algorithm did not incorporate spatial information. This finding suggests that physical location or cell-cell interactions can influence phenotypic specification during hESC-CM differentiation and maturation, which is manifested in the local distribution patterns of individual parameters (Fig. 2.6). The use of the entire set of APs across all clusters also enabled cells that belong to same group to be identified in multiple clusters (Fig. 2.6), which would not be possible by separate analyses of individual clusters. It should be noted that although APs were divided into 3 groups, those groups do not necessarily correspond to nodal-, atrial- and ventricular-like cells, but perhaps, to precursor or intermediate stage cells. Further studies are warranted to develop more advanced methods for AP shape analysis and ultimately, phenotypic classification.

A further improvement for the discrimination of different phenotypes, which has not been employed so far by other laboratories, is the use of different pacing rates, which takes advantage of the different rate-dependent kinetic properties of the ion currents

underlying the AP. As shown in one example, with increasing rate, APD_{80} decreases across the cluster, whereas fractional repolarization may change in opposite directions in different regions of the cluster (Fig. 2.8).

Strength and limitations of optical mapping

Sharp microelectrodes and multiple impalements have been used to study the variability in electrophysiology of hEBs (He et al., 2003; Peng et al., 2010), but in practice are limited to around 10 measurements or less per hEB. In contrast, optical mapping is a more flexible approach for measuring action potentials in hPSC-CMs. When used in a plate reader-like system (CellOPTIQ, Clyde Biosciences), average action potentials can be recorded from small groups of cells with relatively high throughput (Hortigon-Vinagre et al., 2016). When used in a high-resolution setup such as the system used in this thesis, hundreds to thousands of recordings can be obtained from hEBs or monolayers. With the right combination of optics, a field of view larger than 1 cm × 1 cm used here can be achieved for measurements in an even broader tissue context. With the development of genetically encoded voltage sensors, it has also become possible to measure action potentials from a specific promoter-driven subpopulation of cardiomyocytes (Chen et al., 2017). However, there are also limitations to the optical mapping approach. First, there are limits on true spatial resolution, owing to diffuse light scattering of the fluorescent signal and volume integration of signals along the recording path (Bishop et al., 2007; Ding et al., 2001). Electrical coupling among neighboring cells can also electrically average APs within close proximity, though this would also affect other experimental methods such as MEAs. The boxcar (for hEBs) or Gaussian (for monolayers) filter applied in the data analysis, which was necessary to improve signal quality, also limits the spatial resolution

in this method. Another limitation of optical measurements is that they measure only relative changes in transmembrane voltage and not absolute values (unless advanced methods such as dual wavelength measurements and microelectrode calibration are used) (Entcheva and Bien, 2006; Fast, 2005). Nevertheless, they have fast responses that can faithfully track the transmembrane voltage and preserve AP shape (Girouard et al., 1996; Tritthart, 2005).

Conclusions

In conclusion, intrinsic variability in electrophysiology was found in small clusters of hPSC-CMs, resembling different phenotypes. The phenotypes can be identified by a waveform-based algorithm. This electrophysiological variability was found to be greatly reduced in large monolayer cultures for both in-house and commercially available hPSC-CMs, suggesting that large monolayer culture promotes similarity in the electrophysiological phenotypes of hPSC-CMs.

Chapter 3

Modeling type 2 long QT syndrome with human iPSC-CMs

3.1 Introduction

Genetic mutations can cause various types of heart disorders, many of which can lead to life threatening arrhythmias. Among these conditions, long QT syndrome (**LQTS**) is characterized *in vivo* by a prolonged QT interval in the patient's ECG, and is accompanied by increased risk of a specific type of polymorphic ventricular tachycardia known as Torsades de Pointes (**TdP**). In inherited LQTS patients, mutations in different cardiac ion channels can cause imbalance of ion currents during repolarization of cardiac action potentials, leading to prolonged QT intervals. A notable example is type 2 LQTS that represents approximately 45% of known LQTS defects (Splawski et al., 2000). In this LQTS family, a reduction in rapid delayed rectifier K^+ current ($\boldsymbol{I_{Kr}}$) caused by mutations in its alpha subunit, known as Kv11.1, encoded by the human Ether-a-go-go Related Gene

(**hERG**) is responsible for the prolonged QT interval. These hERG mutations have been extensively studied using heterologous expression systems, typically in HEK 293 cells, revealing different mechanisms of mutation-induced I_{Kr} reduction, including disruption of channel synthesis, gating, permeation and most commonly, impaired protein trafficking (Anderson et al., 2006; 2014). Temperature and pharmacological correction strategies have also been evaluated using heterologous systems, and were shown to have different efficacy depending on the location and nature of the mutation (Guo et al., 2012; Smith et al., 2016).

More recently, the development of cardiac differentiation using human induced pluripotent stem cells has provided unique opportunities to study inherited heart disorders in a human cardiomyocyte context. These cardiomyocytes, differentiated from patient-specific hiPSCs, preserve the genotype of their donor, making them a promising *in vitro* substitute to native tissue for physiological studies. LQTS was among the first congenital heart diseases being modeled (Moretti et al., 2010), and is one of the most extensively studied diseases using hiPSC-CMs, in part because most LQTS subtypes are caused by a single gene mutation, making genotype identification relatively straightforward (Tester and Ackerman, 2014). At the cellular level, cardiomyocytes recapitulate the LQT2 phenotype in several hiPSC-CM lines carrying hERG missense mutations (Bellin et al., 2013; Matsa et al., 2011; Mehta et al., 2014b; Spencer et al., 2014), and respond to rescuing strategies found effective with heterologous systems, validating their potential use in studies of inherited LQTS. However, few studies are available on the tissue properties of *in vitro* hiPSC-CM syncytial models.

First identified in an Asian family with LQT2, the hERG-A422T mutation has been shown to cause dominant-negative suppression of WT hERG when expressed in HEK 293

cells (Guo et al., 2012; Sharma et al., 2004). Further investigation suggested that this missense mutation, like most other hERG missense mutations, caused immature mutant hERG protein to be retained in the endoplasmic reticulum in HEK 293 cells, resulting a trafficking defect, which can be partially rescued by incubation with pharmacologic chaperone E-4031 or low temperature (Guo et al., 2012). Recently, a human iPS line derived from a patient with A422T mutation (**LQT2-A422T**) has been established, and cardiomyocytes derived from these cells have been reported to have prolonged AP duration and Ca^{2+} transients that are consistent with the LQT2 phenotype (Spencer et al., 2014). In this study, the *in vitro* LQT2 model is further explored in a syncytial context, and electrophysiological assays are performed to characterize the LQT2 phenotype associated with this heterozygous A422T mutation. The effect of I_{Kr} activation is also evaluated as a potential rescuing strategy for this LQT2 model.

3.2 Methods

3.2.1 Cell culture and cardiomyocyte differentiation

For comparison with LQT2-A422T hiPSCs, human iPS cells from an unrelated patient with no known cardiac disease was used as control, which is referred to as wild type (**WT**, which is the same as the WT11 line used in **Chapter 2**). WT and LQT2-A422T human iPSCs were maintained feeder-free as monolayers in Essential 8 medium (ThermoFisher). Cardiac differentiation was performed by timed modulation of the Wnt pathway as previously described (Boheler et al., 2014; Wang et al., 2015). Beating cardiomyocytes were dissociated with 0.05% Trypsin (ThermoFisher) and re-plated for different assays. For optical mapping, cells were plated at $3x10^5$ cells/cm^2 on Geltrex

(Gibco)-coated 35 mm tissue culture dishes, where the growth area was restricted by a PDMS stencil to a 10 mm diameter area to match the field of view of the camera system. Similar to **Chapter 2**, the monolayers were kept in culture for 35-55 days total after initiation of differentiation before proceeding further with experiments. A small percentage of monolayers that detached from the culture dish during this time were excluded from experiments.

3.2.2 Molecular biology

Flow cytometry

WT and LQT2-A422T cardiomyocytes were dissociated by 0.05% Trypsin into single cells for flow cytometry. Cells were fixed with BD Cytofix and permeablized with BD Phosflow (both from BD Biosciences) per manufacturer's instructions. Primary antibody against cardiac troponin T (ThermoScientific MS-295-P, 4 μg/200 μL) was used to identify cardiomyocytes. Mouse IgG1 control (Life Technologies MG100, 4 μg/200 μL) was used as isotype control. Cells were stained with Alexa Fluor 488 goat anti-mouse IgG1 antibody (Life Technologies, A21121, 0.6 μg/200 μL) for visualization in the flow cytometer. A BD FACSCalibur cell analyzer was used to perform flow cytometry, and a total of 50,000 events was recorded for each condition.

RT-PCR

Total mRNA of WT and LQT2-A422T cardiomyocytes was extracted by the TRIzol-based protocol. The quantity and quality of extracted mRNA was measured by a NanoDrop Spectrophotometer. A total of 2 μg mRNA was reverse transcribed with a commercial kit (Applied Biosystems). The product cDNA was used for downstream PCR

analysis. Primer pairs used to amplify WT- or mutant-specific KCNH2 mRNA are summarized in Table 3.1. PCR reaction was performed with PCR master mix (Bimake) in a Technic ATC 401 thermal cycler. The PCR product was analyzed by electrophoresis in 1% agarose gel and visualized by SYBR Safe DNA Gel Stain (ThermoFisher).

Table 3.1 Primers used in RT-PCR

KCNH2 WT specific	Forward	5'-GCTGCTGGTCATCTACACGG-3'
	Reverse	5'-CTCGTTGGCATTGACGTAGG-3'
KCNH2, LQT2-A422T specific	Forward	5'-GCTGCTGGTCATCTACACTA-3'
	Reverse	5'-CTCGTTGGCATTGACGTAGG-3'

Western blot

For western blot, total protein was harvested using RiPA buffer (ThermoFisher). For Proteinase K treated samples, cells were first incubated with 200 μg/mL proteinase K (Sigma-Aldrich) in buffer containing 10 mM HEPES, 150 mM NaCl and 2 mM $CaCl_2$ for 30 min, followed by inactivation of proteinase K by ice cold PBS containing 6 mM PMSF (Sigma-Aldrich) and 2 mM EDTA (ThermoFisher). All samples were then resolved using NuPAGE 4-12% SDS-polyacrylamide gel (ThermoFisher) by electrophoresis. Separated proteins were transferred on a PVDF membrane using the iBlot2 Transfer Stacks with the iBlot 2 dry blotting system (both from ThermoFisher). The membrane was then blocked in 10% milk in Tris-buffered saline and stained with mouse anti-hERG monoclonal antibody (Santa-Cruz, sc-377388, 1:100) and mouse anti-GAPDH monoclonal antibody (EMD Millipore, MAB374, 1:1000) overnight at 4°C, and then stained with goat anti-mouse IgG IRDye secondary antibody (LI-COR, 1:10000). The membrane was visualized using the Odyssey imaging system (LI-COR).

Immunocytochemistry

For immunocytochemistry, cells were fixed in 4% paraformaldehyde (Affymetrix) at room temperature, permeabilized with 0.01% Triton X for 5 min, then blocked in 10% goat serum before staining with the following primary antibodies overnight: rabbit anti-hERG polyclonal (Santa Cruz sc-20130, 1:50) and mouse IgG2b anti-cardiac troponin I (US Biological T8665-13F, 1:200). Corresponding secondary antibodies used were: goat anti-rabbit IgG Alexa Fluor 488 and goat anti-mouse IgG2b Alexa Fluor 633 (ThermoFisher, 1:200). The nuclei were stained with 3 μM DAPI (Sigma-Aldrich). Images were taken with a Zeiss LSM 510 Meta confocal microscope with a 63x objective.

3.2.3 Optical mapping

Monolayers were stained with 10 μM di-4-ANEPPS (ThermoFisher) for 10 min at 37°C in Tyrode's solution before transfer to a heated stage for optical mapping. After staining, 10 μM blebbistatin (Sigma-Aldrich) was added to the Tyrode's solution to inhibit motion artifact due to cell contraction. Optical action potentials were recorded with a MiCAM Ultima-L CMOS camera at 500 frames per second with tandem 1x macro lenses, providing a field of view of 1cm x 1cm and spatial resolution of 100 x 100 pixels. Electrical pacing was delivered through a pair of platinum electrodes placed immediately next to the edge of each monolayer. For drug tests, E-4031 (Tocris) or ML-T531 (a kind gift from Dr. Min Li at Johns Hopkins) were added to the mapping bath in sequential incremental concentrations, and action potentials were recorded 8 min after each concentration to allow sufficient time for the cardiomyocytes to respond to the drugs.

Optical recordings were analyzed by custom MATLAB scripts. Briefly, optical action potentials were de-noised at each pixel by regulating the total variance in the signal

using a previously described method (Little and Jones, 2010) and convolved with a 5×5 spatial Gaussian filter. The border of the coverslip was manually traced, and pixels outside the border were excluded from analysis. The derivative of membrane potential (dV/dt) was calculated as previously described (Chartrand, 2011), and then the activation time was found by the time of maximum dV/dt and was used to calculate local conduction velocity. Action potential durations were calculated as the time spent from upstroke to the time of the membrane voltage's first return to a defined percentage towards resting potential (e.g., 30% or 80% repolarization).

3.2.4 Statistics

Data are presented as mean±SD, with number of measurements (values of n) provided. The unpaired Student's t-test was used to compare action potential and conduction velocity measurements between WT and LQT2-A422T monolayers. The paired t-test was used to compare the IQR-APD_{80} and conduction velocities before and after drug application. A significance level of $p < 0.05$ was used.

3.3 Results

3.3.1 Differentiation and syncytial culture of LQT2-A422T hiPSC-CMs

Using a monolayer-based differentiation protocol (Boheler et al., 2014; Wang et al., 2015), beating cardiomyocytes were obtained from both WT and LQT2-A422T hiPSCs. Beating areas were found in cultures as early as 7 days after initiating differentiation, and continued to develop with time. The percentage of cardiomyocytes from differentiation was verified by flow cytometry, which showed >95% cTnT positive cells that were

considered as cardiomyocytes (Fig. 3.1C) for both lines. There was no difference in differentiation efficiency between WT and LQT2-A422T hiPSCs. Dissociating and re-plating the cardiomyocytes with trypsin resulted in evenly distributed monolayers of cardiomyocytes that beat spontaneously and regularly across the entire seeded area, with visible synchronized beating under phase contrast microscopy emerging a few days after re-plating. These monolayers were stable in culture for at least 60 days.

3.3.2 Molecular biological characteristics

To confirm the disease genotype in the LQT2-A422T hiPSCs, Sanger sequencing of the KCNH2 gene was performed around the expected mutation site for both WT and LQT2-A422T hiPSC-CMs. The result confirmed the presence of a heterozygous single nucleotide mutation G1264A in the LQT2-A442T line, leading to a single amino acid substitution (A422T) in hERG (Fig. 3.1A). This missense mutation was not found in WT hiPSCs. Furthermore, RT-PCR of KCNH2 found both wild type and mutant mRNA in LQT2-A422T cardiomyocytes, indicating both alleles were actively transcribed. On the other hand, mutant mRNA was absent in WT cardiomyocytes (Fig. 3.1B), consistent with its labeled WT phenotype. At the protein level, western blots of hERG revealed a single band at around 110 kDa for both WT and LQT2-A422T cardiomyocytes (Fig. 3.1D); however, the relative amount of hERG was less in LQT2-A422T than in WT cardiomyocytes. Proteinase K treatment before protein extraction eliminated the hERG band in both WT and LQT2-A422T cardiomyocytes, indicating the hERG protein was accessible to proteinase K and thus likely bound to the cell membrane. In contrast to findings in HEK 293 cells, there was no distinguishable separation in hERG bands that would correspond to different glycosylation levels of the protein. Immunostaining of

hiPSC-CMs was also performed to study localization of the hERG protein in WT and LQT2-A422T cardiomyocytes (Fig. 3.1E). In WT cardiomyocytes (as labeled by cardiac troponin I, cTnI), hERG was evenly distributed throughout the cell, without significant perinuclear localization. On the other hand, in LQT2-A422T cardiomyocytes, some perinuclear hERG was also present, suggesting a potential trafficking defect, which is consistent with previous heterologous studies (Guo et al., 2012). However, there was also a significant amount of membrane-bound hERG in LQT2-A422T cardiomyocytes, which suggests that successful hERG trafficking was present in these mutant cardiomyocytes, and that the hERG protein may form function potassium channels in the membrane.

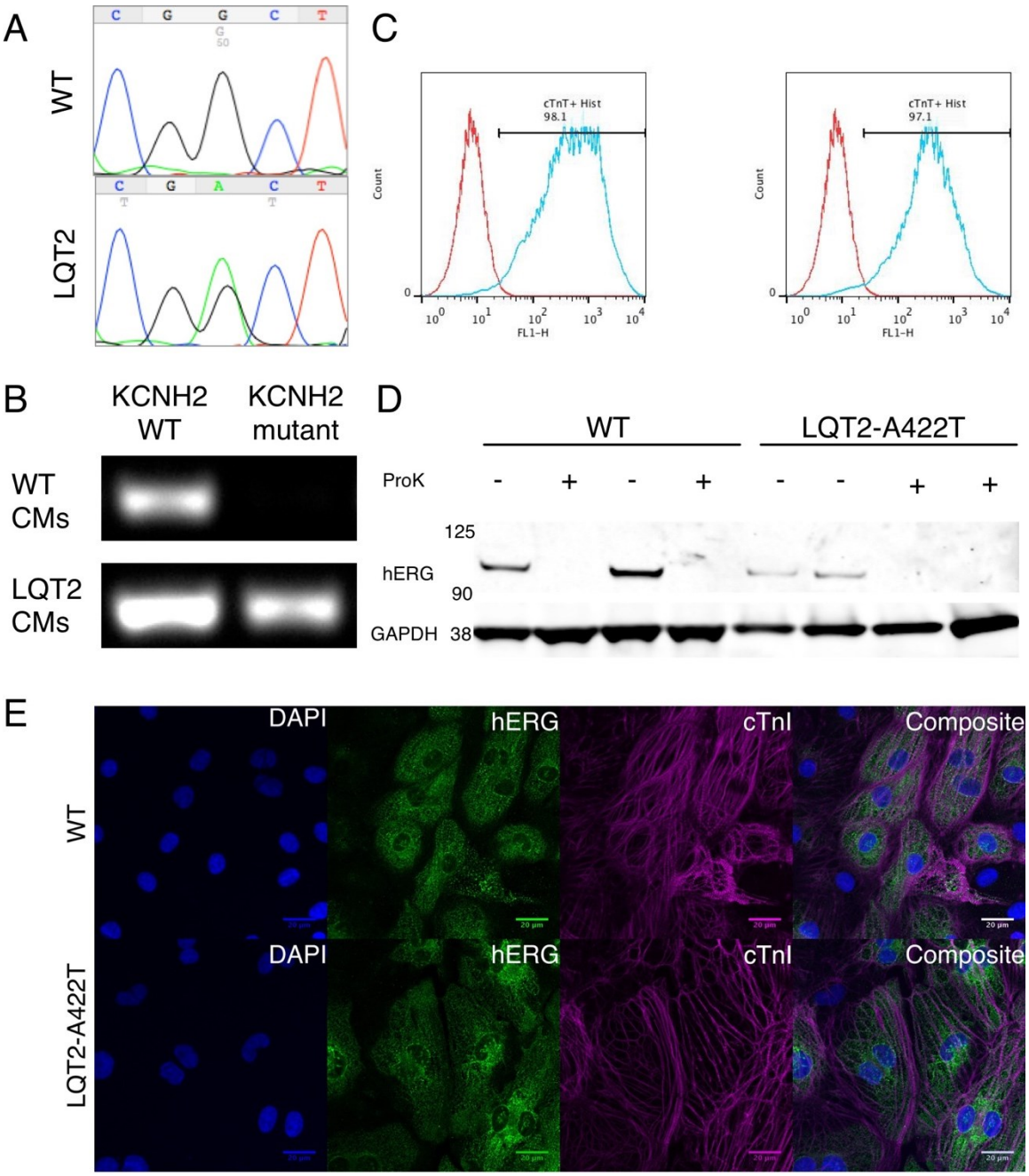

Figure 3.1 Molecular biological characteristics of LQT2-A422T hiPSC-CM. (**A**) DNA sequencing showing heterozygous mutation in KCNH2 gene. (**B**) RT-PCR confirms the presence of only WT mRNA in WT cardiomyocytes, while both WT and mutant mRNA are present in LQT2-A422T cardiomyocytes. (**C**) Flow cytometry of WT and LQT2-A422T differentiation, showing >95% cTnT positive cells. (**D**) Western blot of hERG in WT and LQT2-A422T hiPSC-CMs. Proteinase K was used to confirm membrane localization of detected hERG band. (**E**) Immunostaining of WT (top row) and LQT2-A422T (bottom row) monolayer.

3.3.3 Syncytial properties of hiPSC-CM monolayers

Both WT and LQT2-A422T monolayers could support smoothly propagating action potentials, suggesting a functional syncytium. A pair of platinum electrodes was positioned just next to the monolayer to deliver electrical stimuli at a 1000 ms cycle length (**CL**), and the pacing was always able to initiate waves of action potentials that propagated across the entire area, as shown in the spatial maps of activation times (Fig. 3.2A-B). The smooth activation patterns indicate that the entire monolayer was electrically coupled, without conduction block. At 1000 ms CL, the average conduction velocities (**CVs**) were 12.1±3.4 cm/s and 12.4±6.7 cm/s for WT and LQT monolayers, respectively, and did not differ significantly (Fig. 3.2C). Consistent with the LQT2 genotype, action potentials of LQT2-A422T monolayers were in general longer than those of WT monolayers (Fig. 3.2D). The action potential duration measured at 80% repolarization (**APD_{80}**) for LQT2 monolayers was 416±66 ms, which was significantly longer than 291±19 ms for WT monolayers (Fig. 3.2E). The prolonged APD was mainly due to the longer plateau phase of the action potential, as indicated by the prolonged AP duration at 30% repolarization (**APD_{30}**) for LQT2 monolayers compared with WT monolayers (310±63 ms vs. 170±23 ms, respectively, Fig. 3.2F), rather than the rapid repolarization phase, as measured by triangulation (time from APD_{30} to APD_{80}), which was in fact slightly shorter in LQT2 monolayers than in WT monolayers (105±6 ms vs 121±17 ms, Fig. 3.2G).

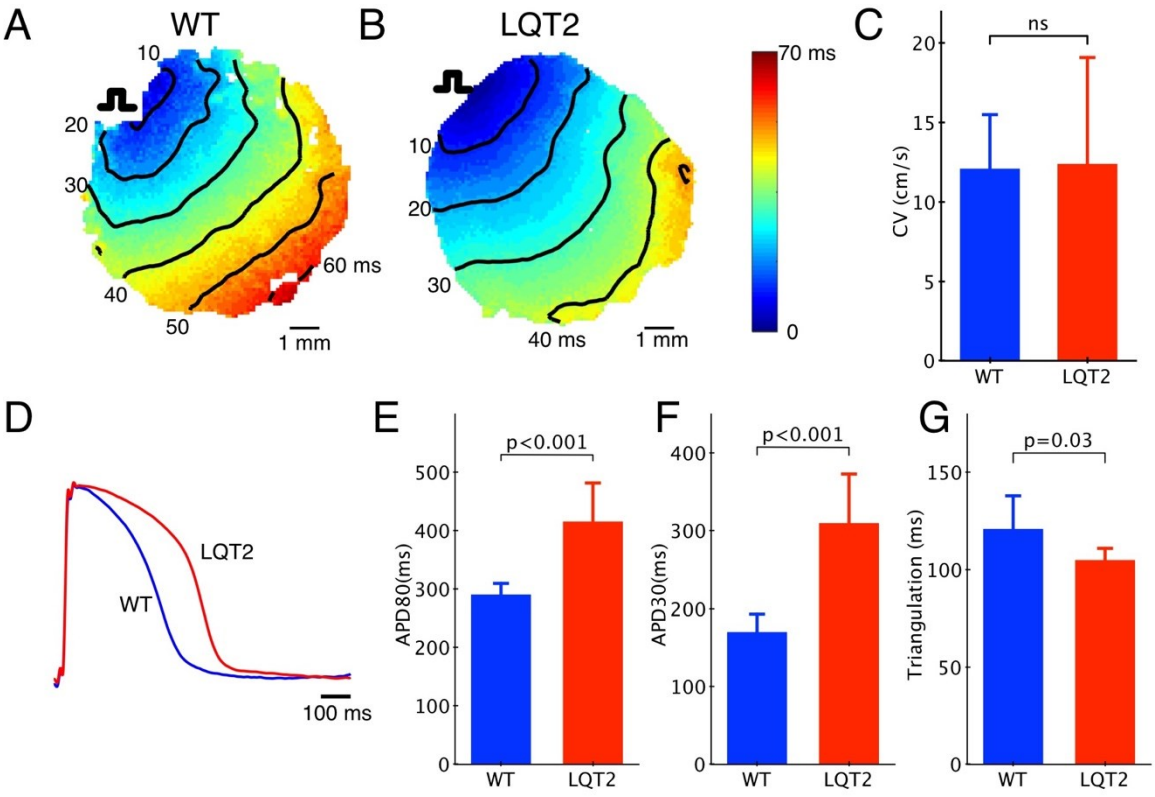

Figure 3.2 Syncytial properties of hiPSC-CM monolayers. (**A-B**) Activation map of representative WT and LQT2 monolayers when electrically stimulated at 1000 ms cycle length. Blue indicates early activation, red indicates late activation. Isochrones have 10 ms spacing. (**C**) Conduction velocity measured in WT and LQT2 monolayers. (**D**) Comparison of average action potentials across entire WT or LQT2 monolayers. (**E-G**) Comparison of action potential parameters between WT and LQT2 monolayers. (**C, E-G**) n=6 for WT monolayers and n=8 for LQT2 monolayers

The use of a cm-sized syncytial model enabled comparison of action potentials recorded from many different sites within the monolayer. An example is shown in Fig. 3.3. Within a single monolayer, there was some variability in action potential shapes, as shown in Fig. 3.3A, where the solid line indicates the average action potential for that monolayer, and lighter traces indicate the superimposed APs recorded from individual sites across the monolayer. APs across the monolayer generally had the same overall morphology of the average AP for the monolayer, with no significant variation observed. This is in sharp contrast to action potentials recorded from single cells, where much larger variability in

AP morphology is usually observed and often categorized into nodal-like, atrial-like and ventricular-like subtypes by their action potential shapes. Action potential durations are usually among the criteria used for subtype classification. Therefore, APD_{80} and APD_{30} from individual recording sites were also calculated, and their distributions are shown in Fig. 3.3B. Comparing the blue cluster of a representative WT monolayer and the red cluster of an LQT2 monolayer, there was a clear phenotypic difference between the two, as the two clusters occupied separate, distinct areas in the AP parameter space. The distributions of APD_{30} (vertical) and APD_{80} (horizontal) in the margins suggest a similar conclusion, with the LQT monolayer having longer APDs at both repolarization levels. The spreads within both the WT (blue) cluster and LQT2 (red) cluster were much smaller than the differences between the means (indicated by the white dots). This is also represented in the separated histograms for both APD_{80} and APD_{30}, where a single, Gaussian-like distribution was observed for each monolayer. The spread in AP morphology presumably reflects biological variability inherent to the hiPSC-CMs, but the tightness of the APD_{80} and APD_{30} distributions suggests there is only one phenotype within the monolayer as discussed in **Chapter 2**. The tightness of distributions within each monolayer was quantified by average IQR-APD_{80} values for WT and LQT2 monolayers were 27.6±11.2 and 23.0±7.6 ms, respectively, and were not significantly different (Fig. 3.3C). As commented earlier, these were much smaller than the difference between the mean APD_{80}s (125±69 ms).

Further, how cells with different AP characteristics are spatially distributed within a monolayer was studied. The spatial maps of APD_{80} of representative WT and LQT2 monolayers are shown in Fig. 3.3D-E, respectively. Overall, there was a tendency for cells with similar APD_{80} to cluster within proximity of each other (n = 6 WT monolayers and n

= 8 LQT2 monolayers), rather than being distributed in an intermixed pattern (none observed). This local grouping phenomenon suggests that environmental factors, such as bioelectrical, biomechanical and biochemical signals, may cause cells in proximity to develop similar electrophysiological properties, even for disease hiPSC-CMs, as discussed in **Chapter 2**.

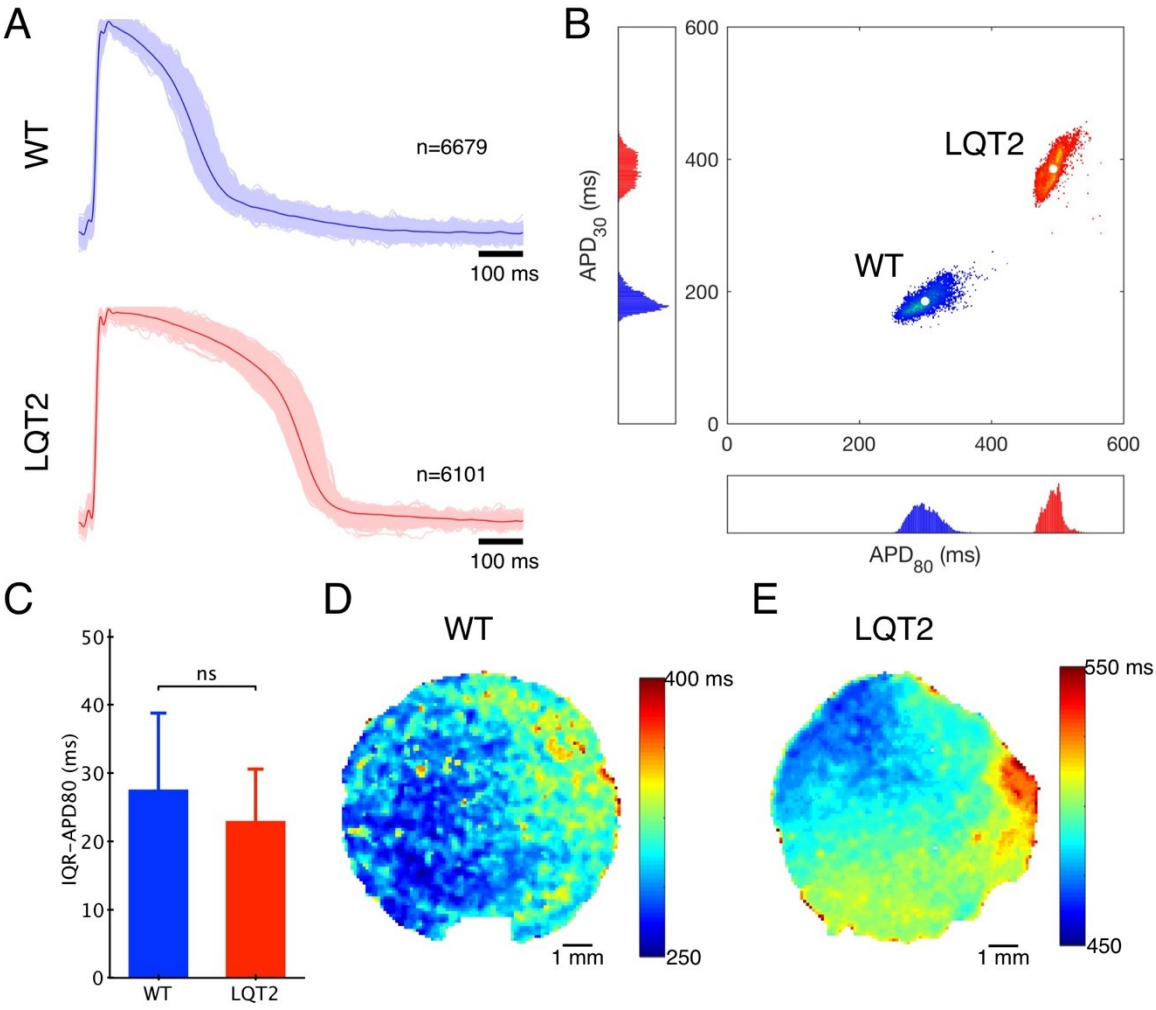

Figure 3.3 Variability in WT and LQT2 monolayers. (**A**) Action potential variability in representative WT (blue) and LQT2 (red) monolayers. Solid lines are average action potential of the monolayer. Shaded areas indicate overlay of action potentials recorded from individual sites within the monolayer (n=6679 for WT and n=6101 for LQT2). (**B**) APD_{80} and APD_{30} distributions of WT and LQT2 monolayers. (**C**) Comparison of IQR-APD_{80}, a measurement of APD_{80} variability, between WT (n=6) and LQT2 (n=8) monolayers. (**D-E**) Spatial map of APD_{80} in representative WT and LQT2 monolayers.

3.3.4 Response of WT and LQT2 monolayers to I_{Kr} blockade with E-4031

The A422T mutation in hERG has been shown in HEK 293 cells to impair the rapid component of the delayed outward potassium current (I_{Kr}). Since immunofluorescence data suggests membrane-bound hERG exists in the heterozygous LQT2-A422T hiPSC-CMs (Fig. 3.1E), additional I_{Kr} blockade experiments were conducted. E-4031 (a specific I_{Kr} blocker) was applied to LQT2-A422T monolayers, which led to a concentration-dependent prolongation of action potential (Fig. 3.4A), confirming the presence of functional I_{Kr} in LQT2 monolayers. Furthermore, E-4031 led to loss of excitability in LQT2 monolayers at 20 nM concentration for all 5 samples tested, and at 10 nM for 3 among them, which suggests that I_{Kr} assists in the maintenance of resting potential and sodium current availability necessary for excitation. On the other hand, WT monolayers retained excitability with I_{Kr} blockade by E-4031 at a much higher concentration, up to the highest concentration tested (100 nM). Similar to LQT2 monolayers, WT monolayers also showed a concentration-dependent prolongation in action potentials with increasing E-4031 (Fig. 3.4B), but the concentration required to elicit a given amount of AP prolongation was much higher than that required for LQT monolayers. The concentration responses to E-4031 in terms of APD_{80} (a measure of the overall action potential duration), APD_{30} (a measure of the plateau phase duration) and triangulation (a measure of the rapid repolarization phase duration) are shown in Fig. 3.4 C-E, where LQT2 monolayers demonstrated a higher sensitivity to E-4031 compared to WT monolayers, as shown by the left-shifted response curves. Furthermore, I_{Kr} blockade prolonged the plateau and rapid repolarization phases of the action potential in LQT2 monolayers as evident by simultaneously increased APD_{30}, APD_{80} and triangulation. But in WT monolayers its effect was mostly on the rapid

repolarization phase, with a more marked increase in APD_{80} and triangulation than in APD_{30}.

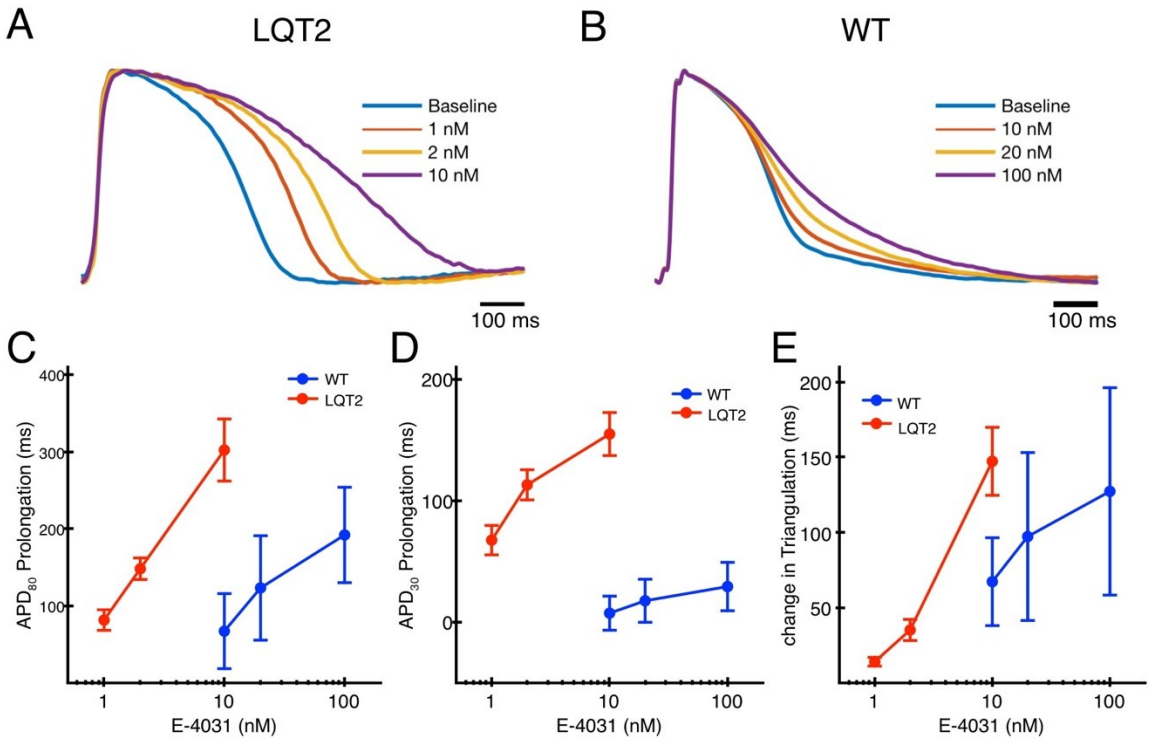

Figure 3.4 Monolayer response to I_{Kr} blockade by E-4031. (**A**) Average action potentials across an LQT2 monolayer in response to 0-10 nM E-4031. (**B**) Average action potentials across a WT monolayer in response to 0-100 nM E-4031. (**C-E**) Concentration-dependent APD_{80} (C), APD_{30} (D) and Triangulation (E) responses to E-4031 in LQT2 (n=5 for 1 nM and 2 nM, n=2 for 10 nM) and WT (n=3) monolayers. Error bars indicate standard deviation.

3.3.5 Response of WT and LQT2 monolayers to I_{Kr} activation with ML-T531

Next, the hypothesis that I_{Kr} can normalize action potentials in LQT2-A422T monolayers was tested. ML-T531 is an I_{Kr} activator that enhances the current by reducing the voltage sensitivity of inactivation, and has been shown to normalize action potentials in LQT1 (reduced I_{Ks}) hiPSC-CMs (Zhang et al., 2012). With ML-T531, APs recorded from LQT2 monolayers showed a concentration-dependent shortening (Fig. 3.5A). At 10 μM (highest concentration tested), an elevated membrane potential at the end of rapid

repolarization was also observed, before slowly returning to baseline (Fig. 3.5A, arrow) which may indicate an increased risk of ectopic activity. On the other hand, ML-T531 did not significantly shorten the action potentials of WT monolayers (Fig. 3.5B), possibly because of the relatively short plateau phase, which is where ML-T531 would have been most effective by keeping I_{Kr} from becoming inactivated. Measurements of AP durations are also consistent with the waveform observations. ML-T531 significantly shortened APD_{80} in LQT2 but not WT monolayers (Fig. 3.5C), which was mainly the result of shortened plateau (as measured by APD_{30}, Fig. 3.5D) rather than of more rapid repolarization (as measured by triangulation, Fig. 3.5E). Indeed, 6 μM of ML-T531 shortened APs in LQT2-A422T monolayers to a level comparable to that of WT monolayers. Furthermore, a representative activation map showed that in the presence of ML-T531 the monolayer still supported smooth AP propagation (Fig. 3.5F), which was also observed in two other LQT2 monolayers tested. ML-T531 also led to an increase in conduction velocity in LQT2 monolayers at 10 μM concentration ($p=0.002$, $n=3$), which may be a result of a greater percentage recovery of excitability due to the increased diastolic interval at the constant 1000 ms cycle length (Fig. 3.5 G).

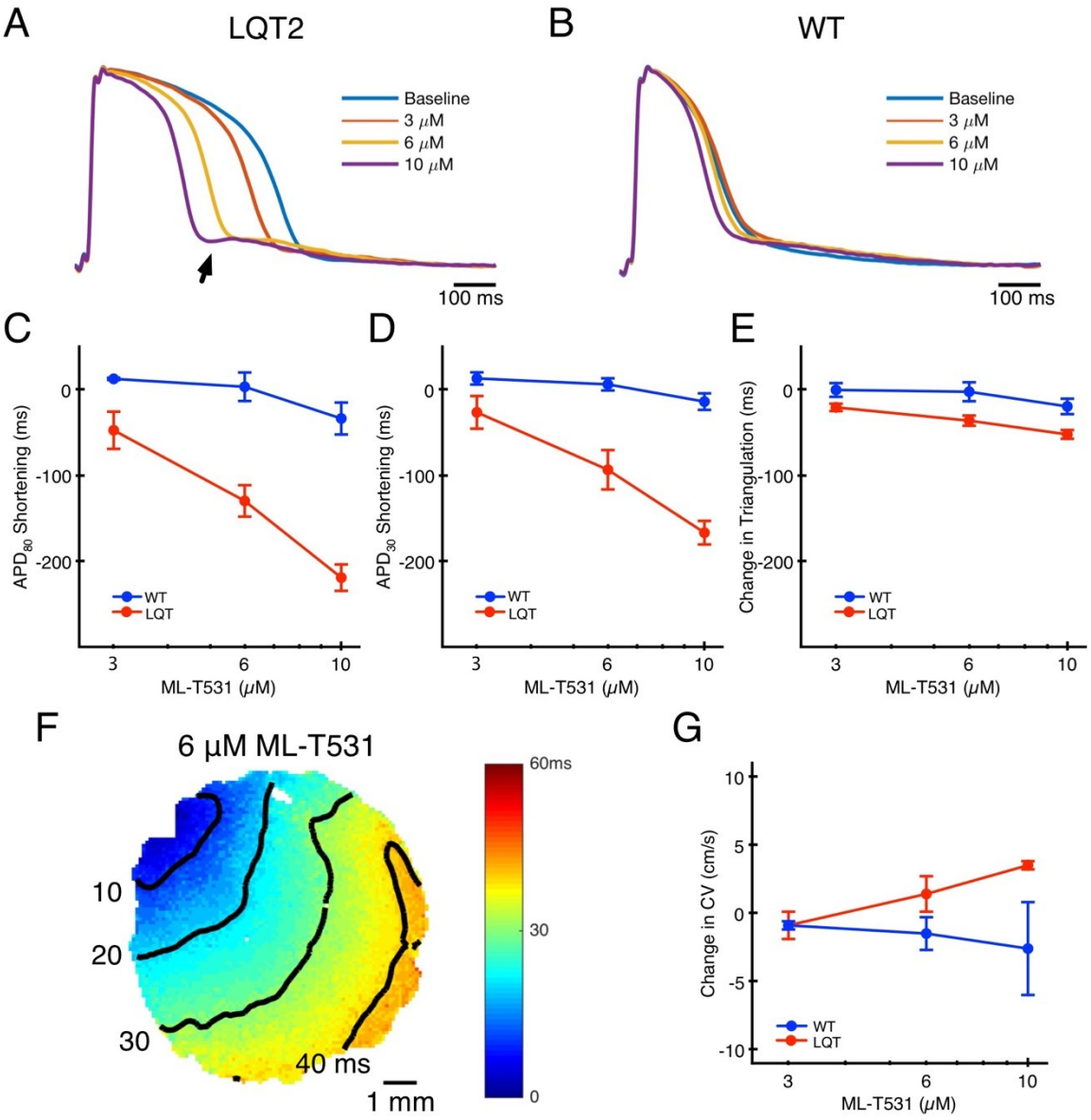

Figure 3.5 Monolayer response to I_{Kr} activation by ML-T531. (**A**) Average action potentials across an LQT2 monolayer in response to 0-10 μM ML-T531. (**B**) Average action potentials across a WT monolayer in response to 0-10 μM ML-T531. (**C-E**) Concentration-dependent response of APD_{80} (C), APD_{30} (D) and Triangulation (E) to ML-T531 in LQT2 and WT monolayers. Error bars indicate standard deviation. (**F**) Activation times in a representative LQT2 monolayer with ML-T531. (**G**) Conduction velocity response to ML-T531 in WT and LQT2 monolayers. (**C-E,G**) n=3 each for LQT2 and WT.

3.3.6 Dependency of drug response to baseline action potential duration

Next, the effect of I_{Kr} blockade and activation on action potential variability was investigated. The APD_{80} histograms at different E-4031 concentrations for a representative LQT2 monolayer are shown in Fig. 3.6A-a. The AP variability (IQR-APD_{80}) was not significantly affected by 1 nM E-4031 for this and 4 other monolayers tested (97%±11% of baseline, n=5), but at 10 nM, it increased to 170% and 188% of baseline values for this and one other monolayer that remained excitable, respectively. On the other hand, the APD_{80} histograms at different E-4031 concentrations for a representative WT monolayer are shown in Fig. 3.6A-b. At both 10 nM and 100 nM, IQR-APD_{80} was not significantly affected for this and other 2 monolayers tested (111%±29% and 116%±35% of baseline, respectively, n=3).

Since the AP-shortening effect by ML-T531 was most prominent during the plateau phase rather than the rapid repolarization phase (Fig. 3.5 C-E), APD_{30} was used instead of APD_{80} for studying the effect of ML-T531 on action potential variability. The APD_{30} histograms are shown for a representative LQT2 monolayer in Fig. 3.6B-a, and for a representative WT monolayer in Fig. 3.6B-b. The spread of APD_{30} for LQT2 was decreased by 10 μM ML-T531 (IQR-APD_{30} was reduced to 50%±5% of baseline), but stayed roughly the same for WT (IQR-APD_{30} was 99%±32% of baseline).

Next, how I_{Kr} blockade and activation can affect action potential variability was investigated. Fig. 3.6C shows the response to E-4031 of cells having similar baseline APD_{80}, using the LQT2 monolayer of Fig. 3.6A-a as an example. The gray histogram in Fig. 3.6C-a shows the APD_{80} distribution within the monolayer. The black bar indicates a subpopulation of cells having similar baseline APD_{80}. Application of 1 nM E-4031 caused

a general right-shift of the histogram for this monolayer, as shown in the light blue histogram in Fig. 3.6C-b. The subpopulation cells with similar baseline APD_{80} responded differently to 1 nM E-4031, as indicated by the solid blue histogram contained within the light blue histogram. The grey lines connecting Fig. 3.6C-a and b indicate the range of post-drug APD_{80} for this subpopulation. The differences between each cell represented in the blue and black histogram is their corresponding responses to 1 nM E-4031, as quantified by ΔAPD_{80}. The variable responses of cells having similar baseline APD_{80} can potentially increase variability.

The process of calculating ΔAPD_{80} was repeated for all cells in the example LQT2 and WT monolayers shown in Fig. 3.6A, and the results are shown in Fig. 3.6D (D-a for LQT2 and D-b for WT) as the dependency of E-4031 blockade (shown as drug-induced increase of APD_{80}) on pre-drug APD_{80}. In general, there was a consistent negative dependence of APD_{80} prolongation (ΔAPD_{80}) on baseline (pre-drug) APD_{80} in LQT2 monolayers with 1 nM E-4031, where the prolongation of APD_{80} was larger in regions with shorter baseline APD_{80} than in regions with longer baseline APD_{80}. This negative APD_{80} dependency disappeared when E-4031 concentration was increased to 10 nM. Instead, the drug response became highly variable independent of the baseline APD_{80}, which was accompanied by a wider spread in the ΔAPD_{80} histogram (compare the red to the blue histogram in the vertical margin of the graph. Fig. 3.6D-a). When linear regression was applied to analyze the ΔAPD_{80} dependency on baseline APD_{80}, a negative slope was found for both 1 nM and 10 nM E-4031, as indicated by the dashed lines in Fig. 3.6D-a. However, the R-squared values decreased with increased E-4031 concentration (from 0.45 to 0.09 in this example), indicating increased variance not explained by the negative baseline APD_{80}

dependency. WT monolayers also showed a consistently negative APD_{80} dependence of APD_{80} prolongation over all E-4031 concentrations tested. There was some variability in E-4031 response within regions of similar baseline APD_{80}, but the spread in the ΔAPD_{80} histogram was not affected by the higher drug concentration (Fig. 3.6D-b). This is also evident by the negative slope found in the linear regression (dashed lines in Fig. 3.6D-b). In fact, the R-squared values increased with increased E-4031 concentration (from 0.29 to 0.50) in this example. The negative APD_{80}-dependency on baseline APD_{80} observed here can potentially decrease variability.

APD_{30} was used instead of APD_{80} for studying the monolayer response to ML-T531, and the ΔAPD_{30}-dependency on baseline APD_{30} is shown in Fig. 3.6E (E-a for the example LQT2 monolayer in Fig. 3.6B-a and E-b for the example WT monolayer in Fig. 3.6B-b). A strong negative APD_{30}-dependency of ΔAPD_{30} was observed at 10 μM ML-T531 for LQT2 monolayers, with a weaker negative APD_{30}-dependency at 3 μM ML-T531 for LQT2 monolayers and at both 3 μM and 10 μM ML-T531 for WT monolayers. In all these monolayers, recording sites with longer baseline APD_{30} tend to be shortened more by the drug than sites with shorter baseline APD_{30}. This is also represented in the example shown in Fig. 3.6E by the steeper slope (-0.69) of the linear regression of LQT2 at 10 μM compared to the other conditions (-0.24 for LQT2 at 3 μM, -0.23 for WT at 3 μM and -0.25 for WT at 10 μM). The R-squared values increased in the LQT2 example from 0.26 at 3 μM to 0.67 at 10 μM, and slightly decreased in the WT example from 0.16 at 3 μM to 0.13 at 10 μM. Like the APD_{80}-dependency on baseline APD_{80} described for E-4031 response, the negative APD_{30}-dependency on baseline APD_{30} observed here can also potentially decrease variability.

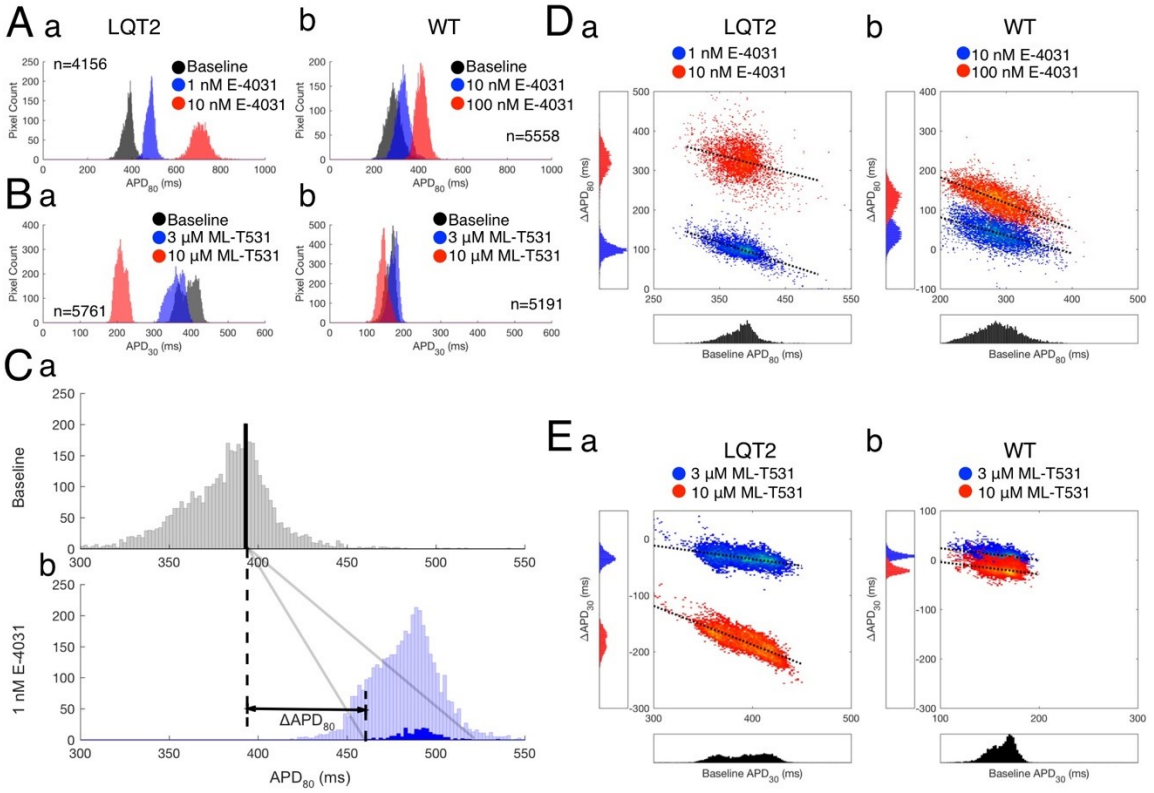

Figure 3.6 Action potential variability in response to I_{Kr} blockade or activation. (**A**) APD_{80} histograms at baseline or with E-4031 for representative LQT2 (a) and WT (b) monolayers. (**B**) APD_{30} histograms at baseline or with ML-T531 for representative LQT2 (a) and WT (b) monolayers. (**C**) Illustration of ΔAPD_{80} calculation. (a) baseline APD_{80} histogram of the LQT2 monolayer of A-a, with the solid black bar highlighting the cells with baseline APD_{80} falling within a 2 ms-wide bin centered at 392 ms. (b) APD_{80} histogram of this monolayer with 1 nM E-4031. The cells represented within black bar in C-a became the dark blue histogram contained in the larger, light blue histogram. ΔAPD_{80} is calculated for each cell in the black bar as the difference between APD_{80} at baseline and with the cell's corresponding point in the dark blue histogram, as indicated in the figure. (**D**) ΔAPD_{80}-dependence on baseline APD_{80} for representative LQT2 (a) and WT (b) monolayers in response to E-4031. (**E**) ΔAPD_{30}-dependence on baseline APD_{30} for representative LQT2 (a) and WT (b) monolayers in response to ML-T531. (**D,E**) Dashed lines are linear regression fits of the scatter plots.

3.3.7 Electrophysiological abnormality in LQT2-A422T monolayers

The two-dimensional cell monolayer provides a substrate in which complex patterns of propagation can occur. Conduction heterogeneity and conduction block are among the most important factors that promote the induction and maintenance of reentrant

arrhythmia. In LQT2-A422T monolayers, conduction heterogeneity and conduction block can be induced by several methods, including premature pacing and hypoxia.

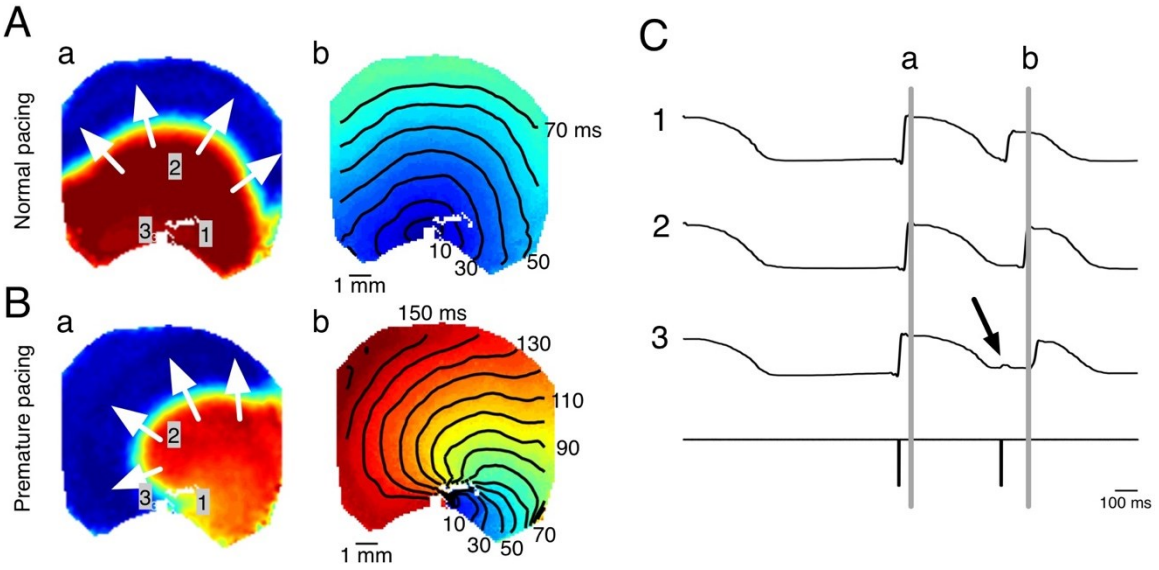

Figure 3.7 Example of conduction heterogeneity in LQT2 monolayers. (**A**) Activation snapshot during baseline pacing at 1000 ms cycle length (a) and corresponding activation map (b). (**B**) Activation snapshot immediately following a 450 ms interval premature stimulus (a) and corresponding activation map (b). In activation snapshots red indicates depolarized regions, blue indicates resting regions. In activation maps isochrones have 10 ms spacing. (**C**) Action potentials recorded from three different locations on the monolayer, as indicated in A-a and B-a. Bottom trace shows the electrical stimulus pulses. Arrow indicates the premature pacing-induced subthreshold activity at site 3.

The effect of premature pacing is shown in Fig. 3.7. At baseline, 1000 ms cycle length pacing always initiated propagating action potentials across the monolayer, as shown in the membrane potential snapshot (Fig. 3.7A-a) and activation map (Fig. 3.7A-b). When a premature stimulus was applied at 450 ms interval following a baseline paced stimulus pulse, the action potential was only able to propagate to one side of the pacing electrode (to the right-hand side in Fig. 3.7B-a, with a complete conduction block on the left-hand side). The activation map had a curved AP propagation pattern (Fig. 3.7B-b), which is a precursor to spiral wave formation. The conduction velocity was also slower,

due to the shorter diastolic interval and wavefront curvature. The presence of conduction block produced by the premature stimulus is also evident in the individual action potential traces recorded from different sites in the monolayer (Fig. 3.7C), corresponding to the numbered sites shown in Fig. 3.7 A-a and B-a. In site 1, to the right of the pacing site, premature pacing elicited an action potential that propagated to site 2. In site 3, to the left of the pacing site, premature pacing only triggered a sub-threshold response (arrow), and an action potential was later initiated by propagation from site 2. This example demonstrates that a monolayer model can be created from LQT2 hiPSC-CMs that manifests conduction heterogeneity created by temporal, dynamic pacing.

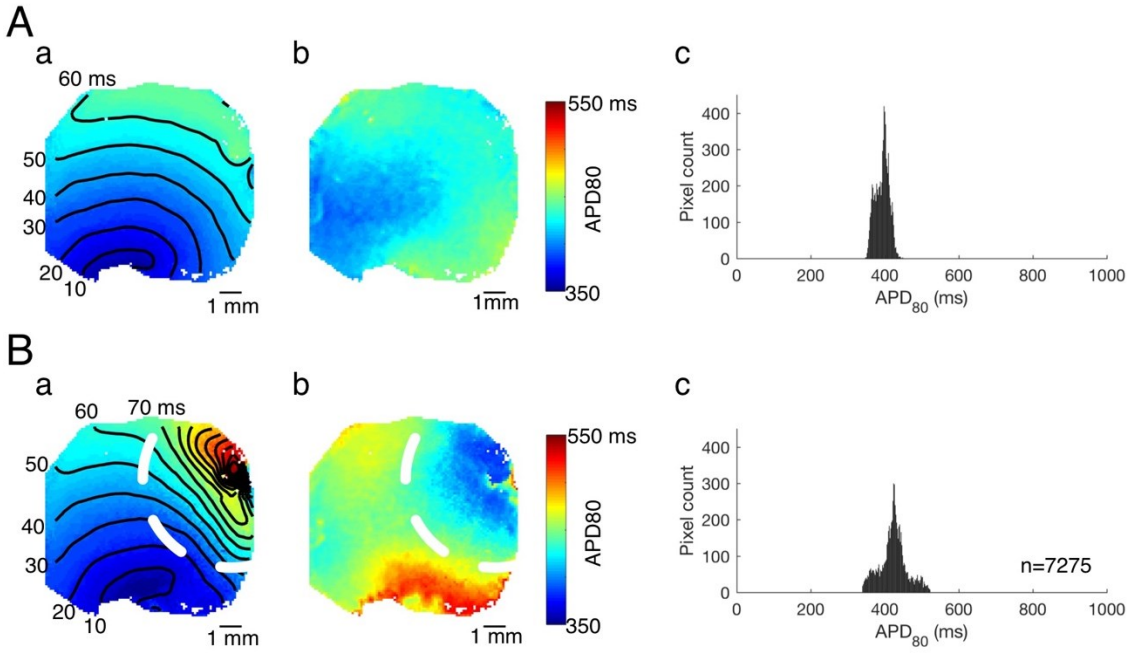

Figure 3.8 Hypoxia-induced variability in LQT2-A422T monolayer. (**A**) Baseline. (**B**) Monolayer partially covered by a circular glass coverslip (approximate location of edge indicated by white dashed line in B-a,b) for 20 min to induce a hypoxic condition. For both baseline and hypoxic conditions: (a) Activation pattern. Isochrones are 10 ms apart. Note the alteration in conduction pattern induced by the coverslip. (b) APD_{80} map. (c) APD_{80} histogram for the entire monolayer.

In addition to dynamic pacing, cellular heterogeneity can also be produced by blocking access of part of the monolayer to the bath solution by a glass coverslip as has been demonstrated previously in neonatal rat myocyte monolayers (de Diego et al., 2008; Pitts and Toombs, 2004). The coverslip creates an acute hypoxic condition, as shown in Fig. 3.8. This LQT2-A422T monolayer at baseline was able to support smoothly propagating action potentials (Fig. 3.8A-a), and the action potential characteristics were also relatively homogeneous, as indicated by the APD_{80} map (Fig. 3.8A-b) and single peak in the APD_{80} histogram (Fig. 3.8A-c). When a glass coverslip was placed on top of a portion of the monolayer (Fig. 3.8B-a), the area underneath the coverslip (bounded by the dashed white line) became hypoxic, which led to slowing of conduction and a complex activation pattern. Action potential variability increased as result of the hypoxic condition. Action potentials in the region located underneath the coverslip became shorter, potentially as a result of the opening of the ATP-sensitive potassium channel ($I_{K,ATP}$) in response to the hypoxic condition, while action potentials in the region surrounding the coverslip became longer, which could be an effect secondary to the slowed conduction and reduced excitability in the adjacent region underneath the coverslip (Fig. 3.8B-b). The overall APD_{80} histogram became wider (Fig. 3.8B-c), reflecting the increased AP variability (Fig. 3.8B-c).

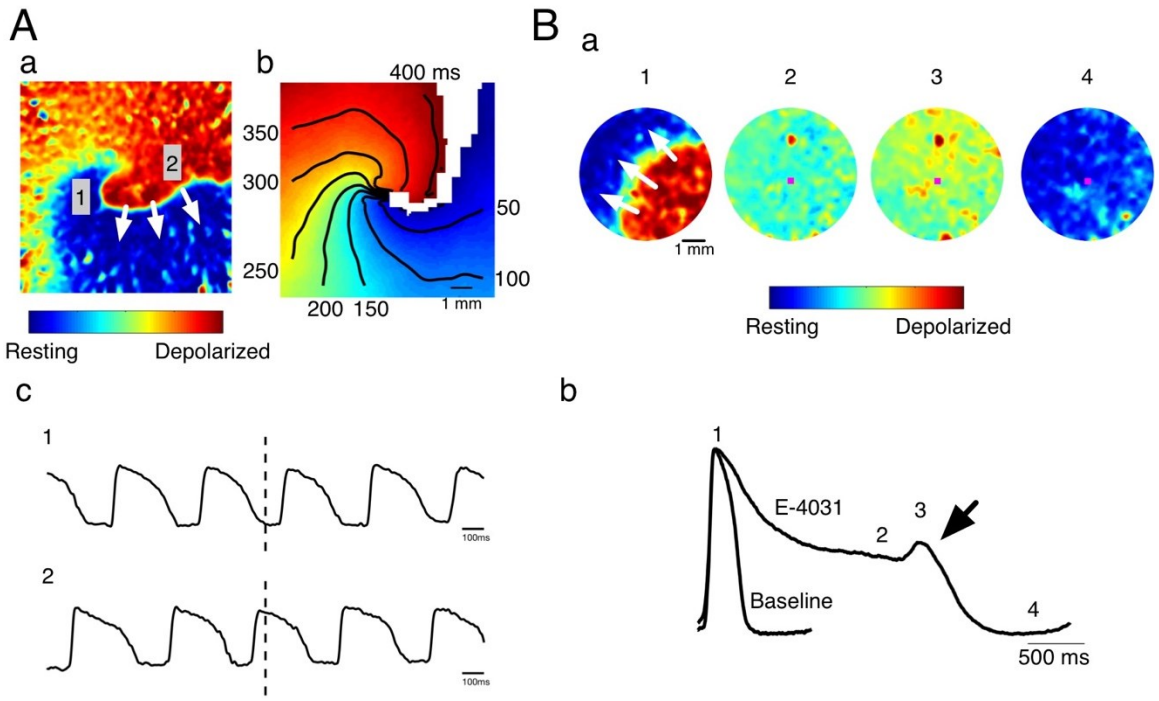

Figure 3.9 Arrhythmic event in LQT2-A422T monolayers. (**A**) Spontaneously formed spiral wave anchored to the center of a 35 mm diameter monolayer. a. Activation snapshot. White arrows indicate direction of spiral wave propagation. Blue indicates resting tissue; red indicates activated tissue. b. activation time map shows the core of the spiral wave. Activation isochones are 50 ms apart. Scale bars in a and b are 1mm. c. Action potential traces recorded within the monolayer, corresponding to the same numbered sites in a. Scale bar is 100 ms. (**B**) Ectopic activity in 6 mm diameter monolayer. a. activation snapshots at different time points corresponding to labels in b, specifically: 1. Propagation of a spontaneous action potential originating from a site at the edge of the monolayer. 2. Just before EAD. 3. Peak of EAD. 4. At rest. b. Action potentials averaged across the entire 6 mm monolayer paced at 1000 ms cycle length at baseline, or spontaneous with 100 nM E-4031. Spontaneous EAD occurred in the presence of E-4031, as indicated by the arrow.

Further, the size of the monolayer can influence the electrophysiological behavior of the monolayer. In a large, 35 mm diameter LQT2 monolayer, a spiral wave formed spontaneously (Fig. 3.9A). In this case, application of ML-T531 abbreviated the action potentials but was not able to terminate the reentrant activity (not shown). On the other hand, EADs were inducible in smaller, 6 mm diameter monolayers (3 out of 4 total), by I_{Kr} blockade with 100 nM E-4031 (Fig. 3.9B). A spontaneous action potential originated from

the edge of the monolayer and propagated across the monolayer (Fig. 3.9B-a, time point 1). The entire monolayer then repolarized by approximately by 50% (Fig. 3.9B-a, time point 2), just prior to the occurrence of an EAD. The EAD then occurred, affecting the entire monolayer and slightly depolarizing the membrane potential before returning to rest (Fig. 3.9B-a, time points 3-4). The average action potentials of this small monolayer at baseline and with E-4031 are shown in Fig. 3.9B-b. Note that E-4031 dramatically prolonged the action potential to have a duration of more than 3 sec. The significantly prolonged period at a depolarized membrane potential provided the necessary condition for EAD formation.

3.4 Discussion

The electrophysiological characteristic of LQTS is a prolonged QT interval in the ECG, which is the result of action potential prolongation at the cellular level. Cardiomyocytes derived from LQTS patients have been shown to recapitulate this key characteristic (Bellin et al., 2013; Lahti et al., 2012; Matsa et al., 2011; Mehta et al., 2014b; Spencer et al., 2014). The results shown here in the monolayer model are consistent with these prior findings, with markedly prolonged APs in LQT2-A422T monolayers compared to those in WT monolayers (Fig. 3.2). The morphological changes in action potential observed here are also similar to those previously reported, where LQT2 cardiomyocytes generally have a more prominent plateau in their APs, despite differences in specific mutations in KCNH2 (Lahti et al., 2012; Matsa et al., 2011; Mehta et al., 2014b). Patch clamp recordings of APs in LQT2 hiPSC-CMs suggest three major cardiac phenotypes, similar to the observations of non-diseased hiPSC-CMs. However, a prolonged AP was

most consistently observed in ventricular-like cardiomyocytes (Lahti et al., 2012; Matsa et al., 2011; Mehta et al., 2014b), not always in atrial-like cardiomyocytes (or even absent (Lahti et al., 2012)), and not in pacemaker-like cardiomyocytes (Matsa et al., 2011). In contrast, I have shown in **Chapter 2** that cell monolayers promote a single phenotype in hPSC-CMs. The observations with LQT2-A422T hiPSC-CMs of a single LQT2 phenotype also support this finding. Here, the single phenotype is ventricular-like with prolonged action potential duration, which is the characteristic electrophysiological feature of LQTS. As discussed in **Chapter 2**, the reduced variability in AP duration and morphology is likely to be a combined result of cell-cell interactions through bioelectrical, biochemical and biomechanical pathways. This is very different from observations from patch clamp studies, where varying action potential morphologies are observed and empirically identified as different subtypes, and where the prolongation in action potentials is also absent in some subtypes. The promotion of a single phenotype in the monolayer model can result in more consistency in terms of studying cardiac diseases like LQT2.

Spontaneous arrhythmic activity is frequently observed in single cell electrophysiological recordings of LQT2 hiPSC-CMs, usually as EADs. A previous study on hiPSC derived cardiomyocytes carrying the same LQT2-A422T mutation showed that small clusters of diseased hiPSC-CMs had markedly prolonged action potentials and spontaneous EADs that were closely correlated with their Ca^{2+} transients, demonstrating a possible mechanism of arrhythmia (Spencer et al., 2014). Interestingly, this ectopic activity was not observed in the 10 mm monolayers of this study (Fig. 3.4A), which resembled a much milder LQT2 phenotype. However, stressing the 10 mm LQT2 monolayers further with E-4031 revealed an elevated sensitivity to I_{Kr} blockade compared to WT monolayers

(Fig. 3.4A,B), consistent with previous observations of the LQT2 hiPSC-CM phenotype (Matsa et al., 2011), although EADs were still absent in this study. It was only when the size of the monolayers was reduced to 6 mm, and with I_{Kr} blockade, that EADs were observed (Fig. 3.9). The reduced-dimension monolayers are closer to, although still much larger than the small clusters used in previous studies with MEAs (Lahti et al., 2012; Matsa et al., 2011; Mehta et al., 2014a). Taken together, these observations suggest the dimension of syncytial cultures may affect the stability and occurrence of ectopic activity in hiPSC-CMs. It is worth pointing out that despite being significantly higher than in healthy adults, the occurrence of cardiac events in LQTS patients is still rare in absolute measures (Kim et al., 2010b). Thus, the absence of EADs in cm-sized syncytial monolayers may indeed be a manifestation more similar to the patient situation.

The mechanism of the hERG-A422T mutation affecting hERG current was first studied in heterologous expression systems using HEK 293 cells (Guo et al., 2012; Sharma et al., 2004). Like many other mutations in the KCNH2 gene, as reviewed in (Smith et al., 2016), A422T has been shown to lead to marked reduction of I_{Kr} by causing a hERG trafficking defect, and exert dominant-negative suppression of WT protein. The immunofluorescence data in this study are consistent with this mechanism, in that perinuclear hERG was observed in LQT2-A422T but not in WT cardiomyocytes (Fig. 3.1E). However, membrane-bound hERG expression was also found in both WT and LQT2-A422T cardiomyocytes. This is probably a manifestation at the protein level of the mutation being heterozygous in the LQT2-A422T hiPSC line, and suggests that, at physiological expression levels in a cardiomyocyte, not all hERG proteins are affected by the trafficking defect. Other evidence of membrane-bound hERG expression includes the

protease K-sensitive band in western blots (Fig 3.1D). Some earlier reports of LQT2 hiPSC-CMs carrying different KCNH2 mutations reported two hERG bands in western blots, indicative of different levels of glycosylation and therefore a possible trafficking defect (Bellin et al., 2013; Mehta et al., 2014b), but in this study only a single band was observed.

Methods to rescue diseased phenotypes can also be evaluated using patient-specific hiPSC-CMs. For LQTS, widely adopted strategies based on the mechanism of the disease include: 1) β-blockers, which has high efficacy in LQT1 patients, by reducing ectopic events that could lead to arrhythmia during exercise; 2) pharmacological strategy that compensates for the abnormal function of the mutant channel, thereby restoring balance in ion currents and normalizing action potentials, and 3) specifically for trafficking defects, chemical chaperones that stabilize the mutant protein and facilitate trafficking to restore normal channel expression (Ruan et al., 2008). The membrane-bound hERG found in immunostaining, as well as E-4031-induced AP prolongation suggests the presence of functional I_{Kr} in LQT2-A422T monolayers, making pharmacological I_{Kr} activation a viable strategy to be tested. The ML-T531 used in this study is an I_{Kr} activator that enhances I_{Kr} by reducing the voltage sensitivity of channel inactivation during an action potential. It has been shown previously to normalize action potentials in LQT1 (KCNQ1 mutation) hiPSC-CMs (Zhang et al., 2012). Application of ML-T531 was sufficient to normalize action potentials in the present LQT2-A422T model (Fig. 3.5A), supporting the notion that functional hERG is present at the cell membrane. The ectopic activity induced by a high concentration of ML-T531 indicates the presence of a net inward current towards the end of the action potential, which could be a result of an overly shortened action potential

duration, where outward I_{Kr} inactivates near the resting potential regardless of the presence of ML-T531, while inward currents such as I_{CaL} or I_{NaCa} may still persist. A similar observation of an afterdepolarization in the presence of a different I_{Kr} enhancer has been reported in a different LQT2 hiPSC-CM model (Matsa et al., 2011), although in that study beta-adrenergic stimulation was also required.

To date, electrophysiology studies using hiPSC-CMs have been predominately performed with isolated cardiomyocytes and patch clamp. These cellular-level models are valuable in understanding single cell electrophysiology and the triggers of arrhythmia events, such as EADs. Small clusters of cells have also been used where their electrophysiology was recorded with MEAs in the form of field potentials (**FPs**). While it has been shown that FPs are correlated to APs, especially with respect to their durations (Halbach et al., 2003), and it is possible to mathematically relate FPs to APs (Tertoolen et al., 2017), they are still indirect measures of the APs. Due to the increased complexity in circuit design with the fabrication of an increased number of electrodes, a typical MEA system is limited to approximately 60 electrodes and is usually recording from a much smaller area (around 1mm × 1mm) than the areas that were optically mapped in the monolayers studied in this chapter. While MEAs do record electrophysiological activities from small groups of cardiomyocytes that are considered to form a functional syncytium, the small dimension greatly limits the measurements of tissue-level properties such as conduction velocity. The smaller dimension models also cannot sustain reentrant arrhythmia, which therefore limits their application in studying the maintenance of an arrhythmia event.

High resolution optical mapping enables simultaneous recordings of action potentials of large hiPSC-CM populations across much larger syncytial areas than those studied with MEAs. This enables the study of variability in electrophysiology that can favor drug- and disease-induced arrhythmias. One example explored in this study was variability in cellular responses to I_{Kr} blockade and its dependency on baseline electrophysiology. In general, a negative APD_{80}-dependency was observed with E-4031 in both WT and LQT2 monolayers, indicating that cells with shorter baseline AP were affected more by I_{Kr} blockade (Fig. 3.6A). This is presumably because those cells had more I_{Kr} than cells with longer baseline APs, and therefore would respond more strongly. Such a negative APD_{80}-dependency can potentially reduce overall AP variability. However, in LQT2-A422T monolayers this effect was masked by an additional overall increase in AP variability in response to the drug for cells having the same baseline APD_{80}s, indicated by the reduction in the R-squared value of the linear fit of the APD_{80}-dependency (Fig. 3.6A-a). Interestingly, this variability among cells with similar baseline APs increased with higher E-4031 concentration (Fig. 3.6A-a), up to the concentration where monolayers lost capture to electrical pacing. The increase in response variability led in turn to increased post-drug APD_{80} heterogeneity, which is a potentially proarrhythmia effect, despite the overall negative APD_{80}-dependency which acts to reduce its variability.

Negative APD-dependency at 30% repolarization (APD_{30}-dependency) was also observed with ML-T531 in LQT2-A422T monolayers (Fig. 3.6C-a), where APD_{30} shortening was smaller in regions with baseline APs having shorter plateaus than in regions with baseline APs having longer plateaus, an effect that again would reduce overall AP variability. This dependency was mostly absent in WT monolayers (Fig. 3.6C-b), due to

only minor shortening in APD by ML-T531. In LQT2-A422T monolayers, the negative APD_{30}-dependency is consistent with the activation window of I_{Kr} current being at AP plateau voltages and is different from the strong APD_{80} dependency observed with E-4031 (Fig. 3.6A-a). This difference can be explained by the different mechanisms of action of ML-T531 and E-4031. ML-T531 shifts the inactivation of I_{Kr} towards more positive voltages and slow inactivation (Zhang et al., 2012), thereby increasing I_{Kr}. The effect of enhanced I_{Kr} is more prominent during the earlier phase of the action potential where inactivation, rather than deactivation determines the availability of hERG channels, and is therefore captured by APD_{30}, and indirectly by APD_{80} (Fig. 3.5C), but not by triangulation (Fig. 3.5E). On the other hand, E-4031 blocks I_{Kr} in its open state (Spector et al., 1996), which affects open channels during the entire duration of an action potential, thereby creating a long-lasting effect that is mainly captured by APD_{80}.

Furthermore, the ability to sustain propagating action potentials in the monolayer model allowed investigation of conduction and its relation to the mutation as well as drug treatment. Smooth propagation of action potentials was always observed in both WT and LQT2-A422T monolayers (Fig. 3.2A,B). There was qualitatively no change in conduction pattern observed with E-4031 or ML-T531 treatment, confirming the maintenance of a uniform syncytium. In the case of ML-T531, a lack of effect on conduction is important if it is to be considered as a rescuing strategy. ML-T531 did slightly increase CV in LQT2 monolayers, but not in WT monolayers. This is perhaps a consequence of the shortening in action potential duration, which in turn shortens the refractory period, prolongs the diastolic interval and allows more time for recovery of excitability of the cardiomyocytes.

The experimentally-induced conduction heterogeneity demonstrated the capability of the 2D monolayer in studying induction and maintenance of reentrant arrhythmia in diseased models. Premature pacing induced a transient unidirectional block (Fig. 3.7B), which is well known to facilitate reentry (Quan and Rudy, 1990). The curved action potential wavefronts resulting from this unidirectional block further demonstrated the potential of reentry wave formation. Another example of conduction heterogeneity is by creating local hypoxia (Fig. 3.8). Acute hypoxia is known to shorten action potentials in cardiomyocytes through activation of ATP-sensitive K^+ channels (Nichols et al., 1991). In the case of the LQT2-A422T monolayer, the action potentials became shorter with a slower upstroke (phase 0) in the region underneath the coverslip. Both of these conditions contributed to the heterogeneity in conduction that ultimately led to slowed and curved AP propagation. For future work, experimental approaches like this can be used to evaluate proarrhythmia risk in disease models. In addition to revealing arrhythmia triggers, the monolayer can also be used to quantify the risk in the syncytium for arrhythmia sustainability.

Finally, reentry arrhythmia can spontaneously form in LQT2 monolayers, but a method to reliably induce arrhythmia in the monolayers was not determined in the current study. The spiral wave in the example shown in Fig. 3.9 was anchored to the center of the monolayer, which was likely a result of a local anatomical defect or local heterogeneity in the monolayer which facilitates spiral wave attachment (Lim et al., 2006), rather than a specific consequence of the LQT2 disease phenotype. Further, the conduction velocity of the spiral wave averaged across the entire observed area within the monolayer (1 cm × 1 cm) was much slower than typically measured in monolayers without spontaneously

formed reentry, as indicated by the denser activation isochrones. This is in part due to fast activation at short cycle lengths, which reduces excitability and slows conduction, as well as the wavefront curvature (Fast and Kléber, 1997). The slow conduction can in turn, contribute to the maintenance of the spiral wave, which also warrants further investigation.

In conclusion, syncytial monolayers of hiPSC-CMs are valuable in disease modeling. In the LQT2-A422T model discussed here, I have shown that the monolayer recapitulates key aspects of the disease phenotype and electrophysiology, and demonstrated that ML-T531 is a possible rescue strategy for this mutation. Tissue level properties, such as conduction velocity and population variability analysis, provided further insight on the proarrhythmic substrate of the disease.

Chapter 4

Predicting response to cardioactive drugs with hiPSC-CM monolayers

4.1 Introduction

Unexpected interaction with cardiomyocytes is the leading cause of removal of pharmaceutical agents from the market, for both cardiovascular and non-cardiovascular applications. There continues to be high demand for more accurate testing platforms for drug development. The current guidelines, ICH S7B for non-clinical and ICH E14 for clinical evaluation, were established in 2005 and before the discovery of hiPSCs. These current guidelines, as reviewed in **Chapter 1.5**, strongly rely on surrogate biomarkers such as interactions with hERG channels, or prolongation of the QT interval in the ECG, to predict the risk of drug-induced proarrhythmia. However, drug-induced proarrhythmia is the consequence of many factors combined, beyond the complexity of these surrogate biomarkers that only measure simple indices such as hERG channel blockade or QT

prolongation. In fact, these current biomarkers have been shown to be inadequate in performance (Gintant, 2011). Recently, the comprehensive in vitro proarrhythmia assay (**CiPA**) initiative has been proposed that combines heterologous expression systems, in silico simulation, hPSC derived cardiomyocytes and human ECG with the goal of developing an improved paradigm for assessing proarrhythmic risk (Colatsky et al., 2016).

Cardiomyocytes derived from hPSCs are an invaluable resource for studying drug interactions in a human context, where the test compound can interact with major cardiac ion channels in a physiological context. Direct biomarkers related to drug-induced proarrhythmia, such as changes in beat rate, action potential duration and EAD formation, can be obtained, providing a more comprehensive assessment of proarrhythmia risk (Sinnecker et al., 2014). The use of hPSC-CMs for drug testing was introduced with hESC-CMs (Braam et al., 2010; Caspi et al., 2009), but hiPSC-CMs provide additional benefits, including patient-specific and disease-specific drug responses. Well-established electrophysiological methods, such as MEA and patch clamp have been widely used in drug testing with hPSC-CMs (Braam and Mummery, 2010; Caspi et al., 2009; Tanaka et al., 2009). Other methods aimed at improving the accuracy and/or throughput of drug screening have also been reported, such as impedance-based assay (Peters et al., 2015), Kinetic image cytometry (Cerignoli et al., 2012) and microphysiological system (Mathur et al., 2015). A comparison with other pre-clinical assays showed that hiPSC-CMs in an MEA assay can identify similar effects as in rabbit ventricular wedge preparations for a panel of drugs (Harris et al., 2013), supporting their potential application for drug screening. However, single cell or small cluster models, while excellent in identifying drug-induced ectopic activities that could trigger an arrhythmia event, provide limited

insight on whether these triggered activities can become sustained arrhythmia. This limitation makes larger syncytial models, such as cell monolayers, desirable for their ability to model tissue-level properties.

In **Chapter 2**, I have shown that monolayer culture promotes uniformity in the electrophysiological phenotype of hPSC-derived cardiomyocytes. The homogeneity in electrophysiology creates a consistent baseline for studying drug response within each monolayer. Further, monolayer-to-monolayer consistency was also found to be high in commercially available hiPSC-CMs, allowing the comparison of responses to different drugs across multiple monolayers. Here, as part of the CiPA phase 1 study, I present the response to cardioactive drugs of monolayers derived from commercially available Cor.4U hiPSC-CMs. The drugs and their respective concentrations were selected by the CiPA initiative, and include three categories: 1) specific ion channel blockers that selectively target a single ion current, including E-4031 (I_{Kr}), nifedipine (I_{CaL}), mexiletine (I_{Na}) and JNJ303 (I_{Ks}); 2) mixed ion channel blockers that interact with multiple channels, including flecainide, quinidine and ranolazine; and 3) drug with off-target ion channel effect, which is moxifloxacin. The specific ion channel blockers suppress different major currents contributing to the cardiac action potentials, as noted above. Studying hiPSC-CM responses to these specific blockers can serve as positive controls to test the fidelity of an hiPSC-CM-based platform for drug screening. The mixed ion channel blockers include two class I antiarrhythmic agents (quinidine: class Ia and flecainide: class Ic) and one anti-angina drug (ranolazine). These multi-activity drugs are used to study if a combination of effects are represented by different biomarkers that correspond to the different channel blockade effects. The drug with off-target effect, moxifloxacin, belongs to the family of

fluoroquinolone antibacterial agents and has a known QT-prolonging effect through blockade of hERG channels (Bischoff et al., 2000; Kang et al., 2001), and serves as an example of an hiPSC-CM-based platform being used to test non-cardiac drugs. In addition to action potential measurements, I also show monolayer responses to drugs in terms of tissue-level properties such as conduction velocity and action potential variability.

Further, electrophysiological heterogeneity in the human heart plays an important role in maintaining normal cardiac function, and deviation from normal heterogeneity can be arrhythmogenic (Boukens et al., 2016). Optical mapping of the human heart wedge preparation has confirmed the presence of a transmural repolarization gradient that is a result of heterogeneity in action potential durations (Glukhov et al., 2010). Faithfully recapitulating this important electrophysiological property of the heart is especially beneficial for studying drug-induced proarrhythmic substrates, but is beyond the capability of a homogeneous cell monolayer. Computational simulations, on the other hand, provide a feasible alternative method to experiments for studying the variability of human cardiomyocyte populations. It has been demonstrated that biological variability can be represented in computational models of cardiomyocytes by introducing stochastic variables in the model's parameter space, which in turn leads to variation in the model output (Britton et al., 2013; Johnstone et al., 2016; Sarkar et al., 2012). This electrophysiological variability also affects the response of simulated cardiomyocytes to channel blockade (Paci et al., 2016). At a tissue level, it has also been reported that an excitable biosynthetic model with inherent variability can simulate variability observed experimentally (Gokhale et al., 2017). In this chapter, I demonstrate the utility of heterogeneous populations of simulated hiPSC-CMs in drug testing. The simulations are

first conducted as an independent population of heterogeneous cells, where population variability in electrophysiology and its response to channel blockade are investigated. In addition, a heterogeneous monolayer is constructed computationally to simulate the electrophysiological heterogeneity found in human heart. The drug response is then studied in a tissue context with this defined heterogeneity.

4.2 Methods

4.2.1 Monolayer culture of Cor.4U cardiomyocyte and drug testing protocol

The Cor.4U cardiomyocytes were obtained from Axiogenesis (Cologne, Germany) along with manufacturer-provided thawing medium and culture medium. Cells were thawed according to the manufacturer's protocol as follows: For each vial containing 4×10^6 cardiomyocytes, 2×T75 tissue culture flasks were used. The tissue culture flasks were coated with fibronectin (Sigma-Aldrich) at 10 μg/mL before plating cells. Cor.4U cardiomyocytes were thawed in manufacturer-provided thawing medium and allowed to attach for 3 hours, and then the medium was changed to manufacturer culture medium. Ciprofloxacin (provided by the manufacturer) was supplemented at 2 μg/mL throughout culture to reduce risk of bacterial contamination. The cells were cultured in T75 flasks for 2 days to allow recovery before re-plating as monolayers.

For cell monolayers, 35 mm cell culture dishes were coated with fibronectin, and the growth area was restricted to a 10 mm diameter circle with PDMS stencil as described in Fig. 2.9A. Cor.4U cardiomyocytes in T75 flasks were dissociated with 0.05% trypsin (ThermoFisher) into single cells, counted and plated at 1.6×10^5 cells/cm^2. Cells were cultured as monolayers for 8-9 days before optical mapping experiments, using the method

described in **Chapters 2 and 3**. Due to the limit in the number of cells available for the CiPA phase 1 study, each drug was tested in only one hiPSC-CM monolayer.

Table 4.1 List of drugs tested and their respective concentrations.

	Drug Name	Target(s)	Conc. 1 (μM)	Conc. 2 (μM)	Conc. 3 (μM)	Conc. 4 (μM)
Specific blockers	E-4031 dihydrochloride	I_{Kr}	0.003	0.01	0.03	0.1
	Nifedipine	I_{CaL}	0.01	0.03	0.1	0.3
	Mexiletine hydrochloride	I_{Na}	1	3	10	30
	JNJ303	I_{Ks}	0.01	0.03	0.1	0.3
Mixed blockers	Flecainide acetate	I_{Na}, also I_{Kr}, I_{Ks}, I_{to}	0.1	0.3	1	3
	Quinidine	I_{Na}, also I_{Kr}, I_{CaL}	0.3	1	3	10
	Ranolazine dihydrochloride	I_{NaL}, also I_{Kr}	1	3	10	30
Off-target effect	Moxifloxacin hydrochloride	Antibiotic, also I_{Kr}	3	10	30	100

As part of the CiPA phase 1 study, all tested drugs were obtained from the CiPA group coordinating experiments among different participating sites. The drug concentrations tested are listed in Table 4.1. A stock solution of each compound that was 1000× the lowest concentration tested was prepared for each set of drug experiments, and different concentrations of drugs were tested serially by adding the necessary amount of stock drug solution to the chamber bath solution to achieve the desired test concentration. Between concentrations the monolayers were allowed 10 min for the drug effect to reach steady-state. Electrical pacing at 1000 ms cycle length was delivered through a pair of platinum electrodes and applied for at least 1 min before recordings of paced action potentials to ensure action potential steady-state.

Data analysis, including pixel inclusion, action potential parameter measurement and variability calculation were performed as described in **Chapters 2 and 3**.

4.2.2 Single cell computational simulation of action potential variability

The computational model of the hiPSC-derived cardiomyocyte by Paci et. al (Paci et al., 2013) was implemented in MATLAB based on the mathematical equations provided in the supplemental information of the original publication, and is referred to as the baseline model. Except for model validation, the ventricular phenotype described in Paci et. al was used for all simulations. Population heterogeneity was simulated by introducing variability to 14 conductances associated with ion currents in the baseline model (summarized in Table 4.1). For a single cell in the population, each of the 14 conductances was scaled by a random variable drawn from a uniform distribution. This process was repeated in a population of 1×10^4 independent cardiomyocytes. The range of the uniform distribution from which the scaling factors were drawn is denoted as the level of variability of the cell population. For 1% variability, the scaling factors were between 0.99 and 1.01; likewise, for 10% variability the scaling factors were between 0.90 and 1.10.

Electrical pacing was simulated by injecting current into the simulated cells at 550 pA for a duration of 5 ms. The steady-state action potential was obtained by simulating 100 action potentials paced at 1000 ms cycle length and then taking the last action potential in the series. Ion channel blockade was simulated by scaling the conductance with another linear factor denoting the level of blockade (for example, 0.5 for 50% blockade). The new steady-state action potential was then obtained by simulating another 100 action potentials paced at 1000 ms cycle length and taking the last action potential in the series. Action potential parameters (APD_{30}, APD_{80} and variability measurement IQR-APD_{80}) were

calculated using the same method used for experimentally obtained action potentials as described in **Chapter 2**.

Table 4.2 List of conductances modified in the Paci 2013 model.

Ion current	Parameter	Description
I_{Na}	gNa	Maximum conductance of the fast Na^+ current
I_{to}	gto	Maximum conductance of transient outward K^+ current
I_{K1}	gK1	Maximum conductance of inward rectifier current
I_{NaK}	PNaK	Maximum conductance of sodium potassium pump
I_{NaCa}	KNaCa	Maximum conductance of sodium calcium exchanger
I_{up}	Vmaxup	Maximum current of Ca^{2+} uptake by SR
I_{CaL}	gCaL	Maximum conductance of L-type calcium current
I_{Kr}	gKr	Maximum conductance of rapid delayed rectifier current
I_{Ks}	gKs	Maximum conductance of slow delayed rectifier current
I_f	gf	Maximum conductance of funny current
I_{rel}	arel, brel, crel	Maximum current of Ca^{2+} release by ryanodine receptors
I_{pCa}	gpCa	Maximum conductance of sarcolemmal Ca^{2+} pump current

4.2.3 Computational monolayer simulation of action potential variability

The monolayer simulation was performed by Joseph Yu in collaboration with Dr. Natalia Trayanova's lab. For these simulations, the ventricular-like hiPSC-CM model described by Paci et al (Paci et al., 2013) was used as the baseline model to create a heterogeneous population of single cells. Different levels of electrophysiological variability were introduced to the individual cells as described in 4.2.2. In ion channel blockade experiments, the effect of the channel blocker was also simulated as described in 4.2.2. The steady state condition of individual cells was achieved by pacing them at 1000

ms cycle length for 50 beats. The cells were then incorporated in a monolayer model containing 100×100 cells that represents a 1 cm × 1 cm square area, with each cell occupying a volume of 100 μm × 100 μm × 100 μm. The dimension of the simulated monolayer is similar to that of the monolayers studied in the optical mapping experiments. Electrical coupling was simulated by an isotropic intercellular conductance of 0.4 μS/mm. Electrical pacing was applied at 1000 ms cycle length at a strength of 60 μA/cm^3 and a duration of 2 ms. It was delivered either to all cells simultaneously, effectively stimulating them all at the same time, or along one edge of the monolayer, simulating a line electrode and initiating a line of propagating action potentials. The monolayer model was solved using the Cardiac Arrhythmias Research Package (**CARP**) as previously described (Vigmond et al., 2003; 2008) for 10 beats at 1000 ms cycle lengths, and the last beat was used for analysis.

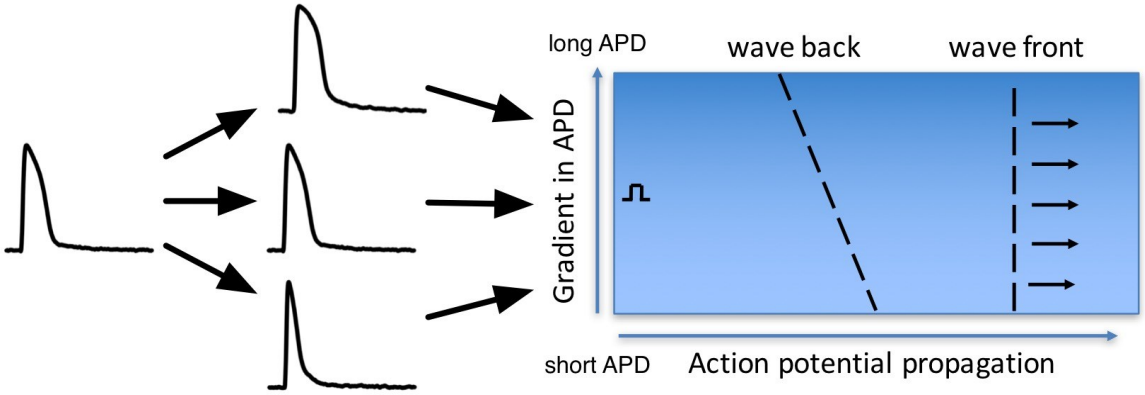

Figure 4.1 Schematic of a monolayer with defined electrophysiological heterogeneity. To create the monolayer, cells with homogeneous electrophysiology (left) are modified through computational methods to generate variability in their ion currents, which is reflected in their APD (middle). This population of heterogeneous cellular electrophysiology is then organized in a 2D monolayer (right) for drug response testing.

Taking advantage of the flexibility in computational simulations, monolayers with defined patterns of heterogeneity can be easily established. Fig. 4.1 shows the schematic

of creating a such a monolayer from the population of individual cells with heterogeneous action potentials. In the example of Fig. 4.1, cells were coupled together and arranged in such a way to create a linear gradient in action potential durations along one dimension of the monolayer, so that cells with longer APDs are placed towards the top edge of the monolayer, while cells with shorter APDs are placed towards the bottom edge of the monolayer. By using this model and stimulating action potential propagation in the perpendicular direction, a spatial gradient in repolarization can be created in a controlled manner, and its response to drug can then be tested. In addition to arranging cells to create a linear APD gradient, single cells were also placed in two other different ways: 1) random placement, where cells were randomly placed into the monolayer; 2) concentric placement, where cells were sorted by their single cell steady-state APD, and those with shorter APD were placed in the center of the monolayer while those with longer APD were placed towards the edges of the monolayer.

4.3 Results

4.3.1 Monolayer response to selective ion channel blockers

The experiments for the CiPA phase 1 study were conducted with the assistance from Dr. Venkatesh Hariharan. The responses of Cor.4U cardiomyocyte monolayers to selective ion channel blockers are summarized in Fig. 4.2.

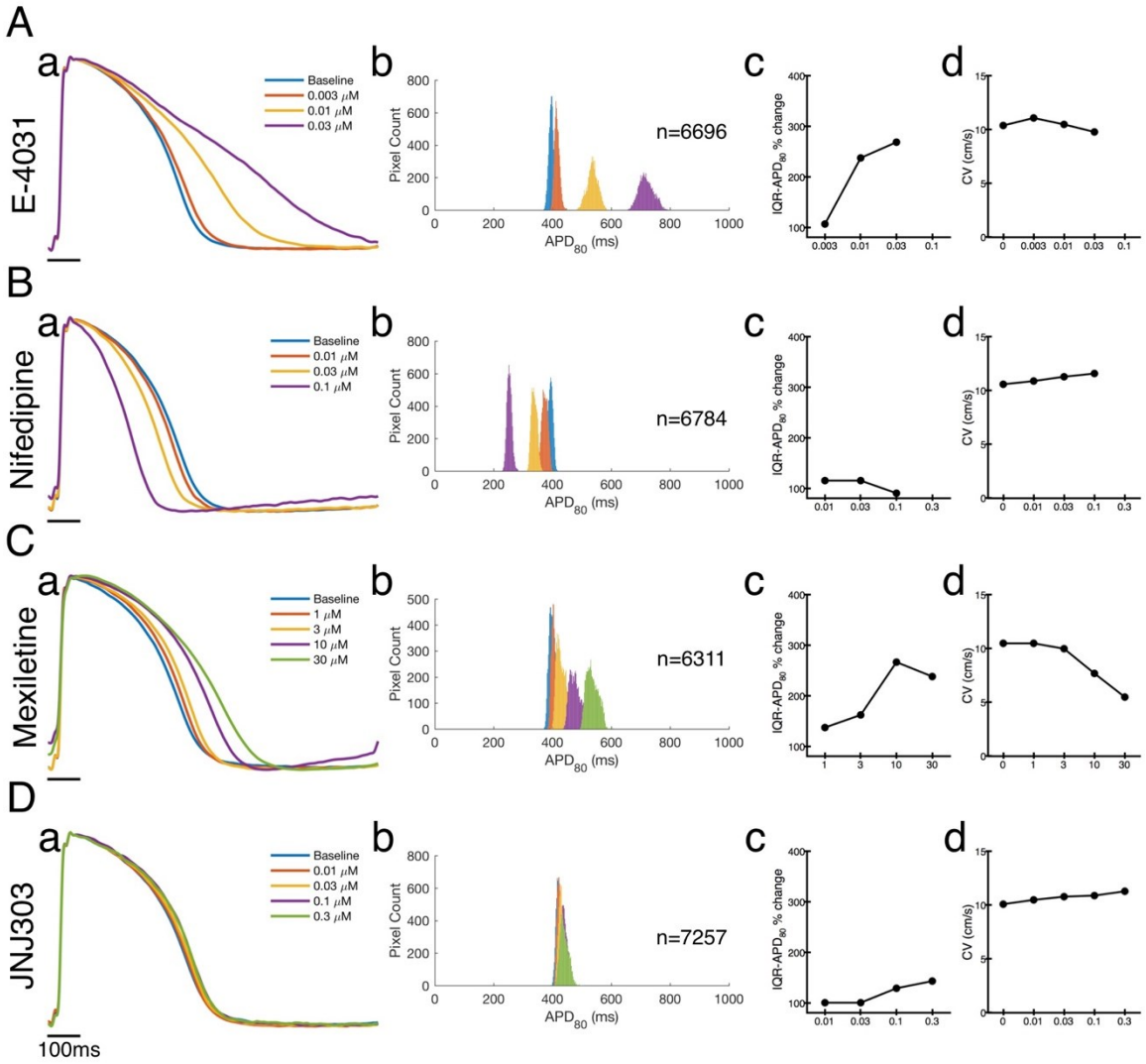

Figure 4.2 Cor.4U monolayer response to selective ion channel blockers. (**A**) E-4031, an I_{Kr} blocker. (**B**) Nifedipine, an I_{CaL} blocker. (**C**) Mexiletine, an I_{Na} blocker. (**D**) JNJ303, an I_{Ks} blocker. For each drug: a. average action potential of the entire monolayer. b. APD_{80} histograms of action potentials from multiple sites (as indicated by the numbers next to the histograms) across the monolayer. Drug concentration is indicated by the same color in (a). c. IQR-APD_{80} for the monolayer at different drug concentrations. d. average conduction velocity for the monolayer at different drug concentrations.

E-4031

E-4031 is a selective blocker of the rapid component of the delayed rectifier potassium current (I_{Kr}), a repolarizing current. It was applied to the monolayer at a concentration of 0.003-0.1 μM. At 0.1 μM, the monolayer lost capture to external pacing

at 1000 ms cycle length. At all other concentrations, E-4031 produced a concentration-dependent prolongation in action potential (Fig. 4.2A-a). The prolongation was mostly during the rapid repolarization phase, resulting a more triangular action potential with drug. APD_{80} histograms widened with E-4031, especially at higher concentrations (Fig. 4.2A-b). indicating an increase in action potential variability, which is also reflected in increased IQR-APD_{80} (Fig. 4.2A-c). The conduction velocity was not affected by E-4031 (Fig. 4.2A-d).

Nifedipine

Nifedipine is a selective blocker of the L-type calcium current (I_{CaL}), a depolarizing current. It was applied at 0.01-0.3 μM. The monolayer became quiescent at 0.3 μM concentration. At all other concentrations, nifedipine shortened the action potential in a concentration-dependent manner (Fig. 4.2B-a). Nifedipine did not change action potential variability in the monolayer, as shown in the APD_{80} histograms and IQR-APD_{80} measurements(Fig. 4.2B-b, c). Conduction velocity was not affected by nifedipine (Fig. 4.2B-d).

Mexiletine

Mexiletine is a selective blocker of the voltage-gated sodium current (I_{Na}), the depolarizing current that initiates the action potential. At concentrations higher than 300 μM it can also inhibit Ca^{2+} and Na^+/K^+ pump currents (Honerjäger et al., 1986). The concentration tested was much lower at 1-30 μM. The monolayer maintained capture at 1000 ms cycle length pacing for all concentrations tested, and the action potentials lengthened in a concentration-dependent manner (Fig. 4.2C-a). Mexiletine also increased action potential variability, as shown in the APD_{80} histograms and IQR-APD_{80} (Fig. 4.2C-

b,c). Conduction velocity was greatly slowed by mexiletine, consistent with its I_{Na} blocking effect (Fig. 4.2C-d).

JNJ303

JNJ303 is a potent blocker of the slow component of the delayed rectifier potassium current (I_{Ks}), another repolarizing current during the cardiac action potential. It was applied at concentrations of 0.01-0.3 μM. Cor.4U monolayers maintained captured at 1000 ms cycle length external pacing at all concentrations. However, JNJ303 did not affect the action potential or its variability (Fig. 4.2D-a-c), or conduction velocity (Fig. 4.2D-d) at the concentrations tested.

4.3.2 Monolayer response to ion channel blockers with mixed or off-target effects

The responses of Cor.4U cardiomyocyte monolayers to ion channel blockers with mixed or off-target effects are summarized in Fig. 4.3.

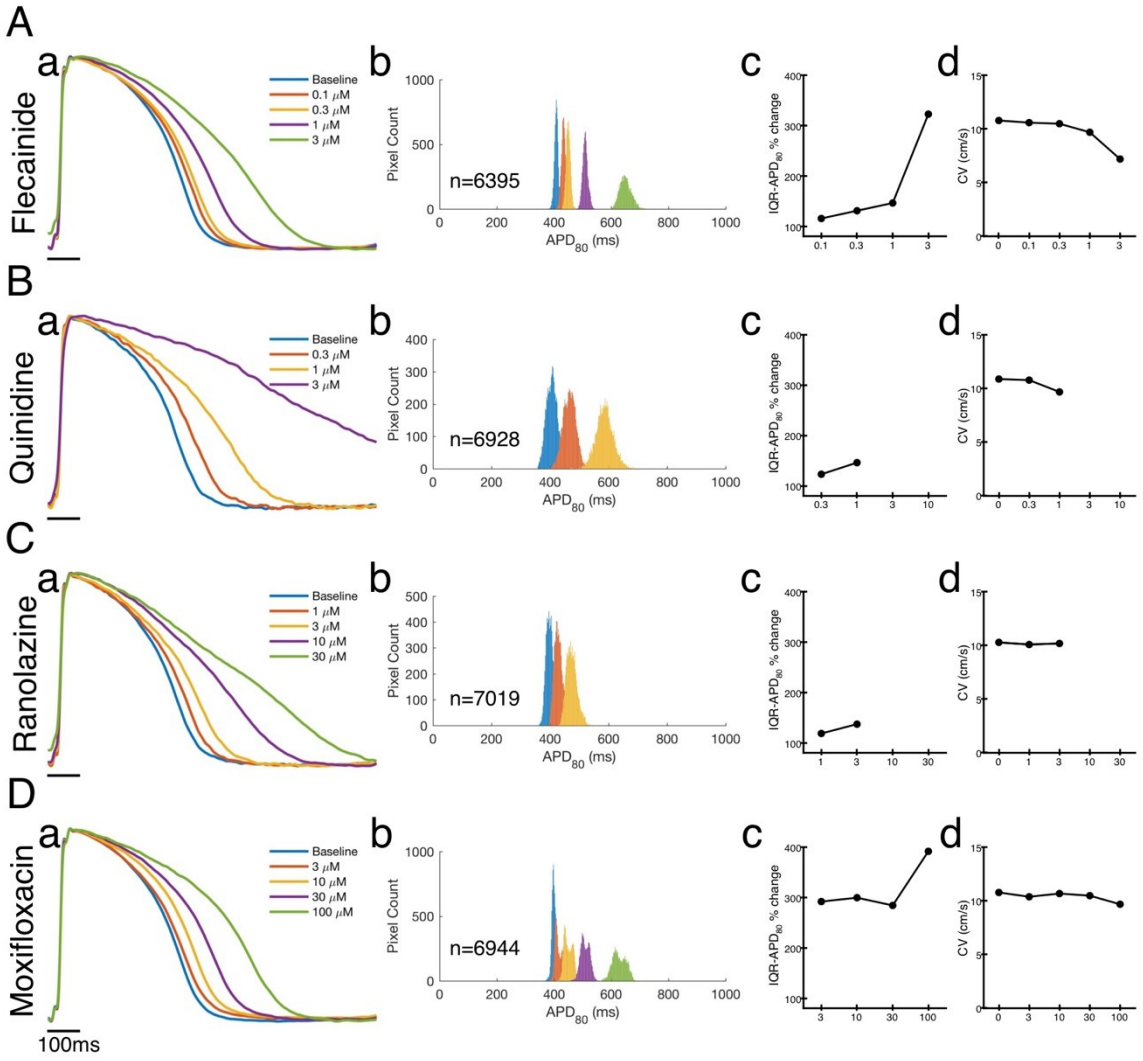

Figure 4.3 Cor.4U monolayer response to cardioactive drugs with mixed ion channel blocking effect. (**A**) Flecainide, a class Ic antiarrhythmia drug. (**B**) Moxifloxacin, an antibacterial agent. (**C**) Quinidine, a class Ia antiarrhythmia drug. (**D**) Ranolazine, an anti-angina drug. For each drug: a. average action potential of the entire monolayer. b. APD_{80} histograms of action potentials from multiple sites (as indicated by the numbers next to the histograms) across the monolayer. Drug concentration is indicated by the same color in (a). c. average conduction velocity for the monolayer at different drug concentrations.

Flecainide

Flecainide is a class Ic antiarrhythmic drug, that mainly blocks I_{Na} and has slow unbinding dynamics but has also been shown to interact with the repolarizing currents I_{Kr}, I_{Ks} and I_{to} (Slawsky and Castle, 1994). Flecainide was applied at concentrations of 0.1-3

μM. The monolayer maintained capture at all concentrations tested, and the action potential was prolonged in a concentration-dependent manner (Fig. 4.3A-a) in both the plateau and repolarization phases, giving the action potentials a slightly more triangular morphology at high concentrations. Flecainide led to an increase in action potential variability at high concentration, as shown in the much wider spread of APD_{80} (Fig. 4.3 A-b) as well as increased IQR-APD_{80} (Fig. 4.3 A-c). Conduction velocity was also decreased by this drug at high concentration (Fig. 4.3 A-d), consistent with its I_{Na} blocking effect.

Quinidine

Quinidine is a class Ia antiarrhythmic agent that primarily blocks I_{Na} but also interacts with I_{Kr} and I_{CaL} (Nenov et al., 1998). Quinidine was tested at concentrations of 0.3-10 μM. At 3 μM, the monolayer could be pace-captured only during every other beat at 1000 ms cycle length pacing (2:1 capture), while at 10 μM it failed to be captured completely. Action potentials were greatly prolonged by quinidine in a concentration-dependent manner (Fig. 4.3B-a), and become very triangular in morphology. Quinidine slightly increased action potential variability as shown in APD_{80} histogram and measured by IQR-APD_{80} (Fig. 4.3B-b,c). Conduction velocity was also decreased by quinidine, as expected for its I_{Na} blockade effect (Fig. 4.3B-d).

Ranolazine

Ranolazine is an anti-angina drug that primarily blocks the late inward sodium current (I_{NaL}). It has also been shown to interact with I_{Kr} (Antzelevitch et al., 2004). The concentration range tested for ranolazine was 1-30 μM. At 10 and 30 μM, the monolayer failed to maintain 1:1 capture at 1000 ms cycle length external pacing. Action potentials were prolonged in a concentration-dependent manner, with prolongation occurring

throughout repolarization. The action potentials also became more triangular with ranolazine (Fig. 4.3C-a). At 1 and 3 μM while the monolayer kept 1:1 capture, the action potential variability was slightly increased (Fig. 4.3C-b,c), while conduction velocity was not affected (Fig. 4.3C-d).

Moxifloxacin

Moxifloxacin is a fluoroquinolone antibacterial agent. However, there is evidence that it also has off-target blockade effect on I_{Kr} (Bischoff et al., 2000; Kang et al., 2001). It was tested at concentrations of 3-100 μM. Moxifloxacin prolonged action potential in a concentration-dependent manner, mainly during the plateau phase and did not lead to a more triangulated AP morphology, which is in contrast to the observation with selective I_{Kr} blocker E-4031 (Fig. 4.3D-a). Action potential variability was markedly increased by this drug, and there was a separation of the APD_{80} histogram into two peaks, possibly suggesting a differential response of two populations of cells to the drug (Fig. 4.3D-b,c). Conduction velocity was not affected by moxifloxacin (Fig 4.3D-d).

4.3.3 Single cell simulation of action potential variability

Numerical simulations using the MATLAB implementation of the 2013 Paci model of hiPSC-derived cardiomyocytes were compared against published simulation data of spontaneous activities and confirmed that the MATLAB implementation generated results identical to those published by Paci et al for both ventricular-like and atrial-like baseline models. Electrical stimulation was able to pace-capture both models, and electrically paced action potentials were obtained at 1000 ms cycle length, and are shown in Fig. 4.4. The action potentials maintained their phenotypic shapes, such as a more prominent plateau phase and longer duration for ventricular-like cells, and a more triangular, shorter duration

action potential for atrial-like cells. The model was paced for 100 beats to reach steady state, which was confirmed by minimal beat-to-beat differences in ion currents as well as intracellular ion concentration transients. The ventricular-like model was used in subsequent simulations.

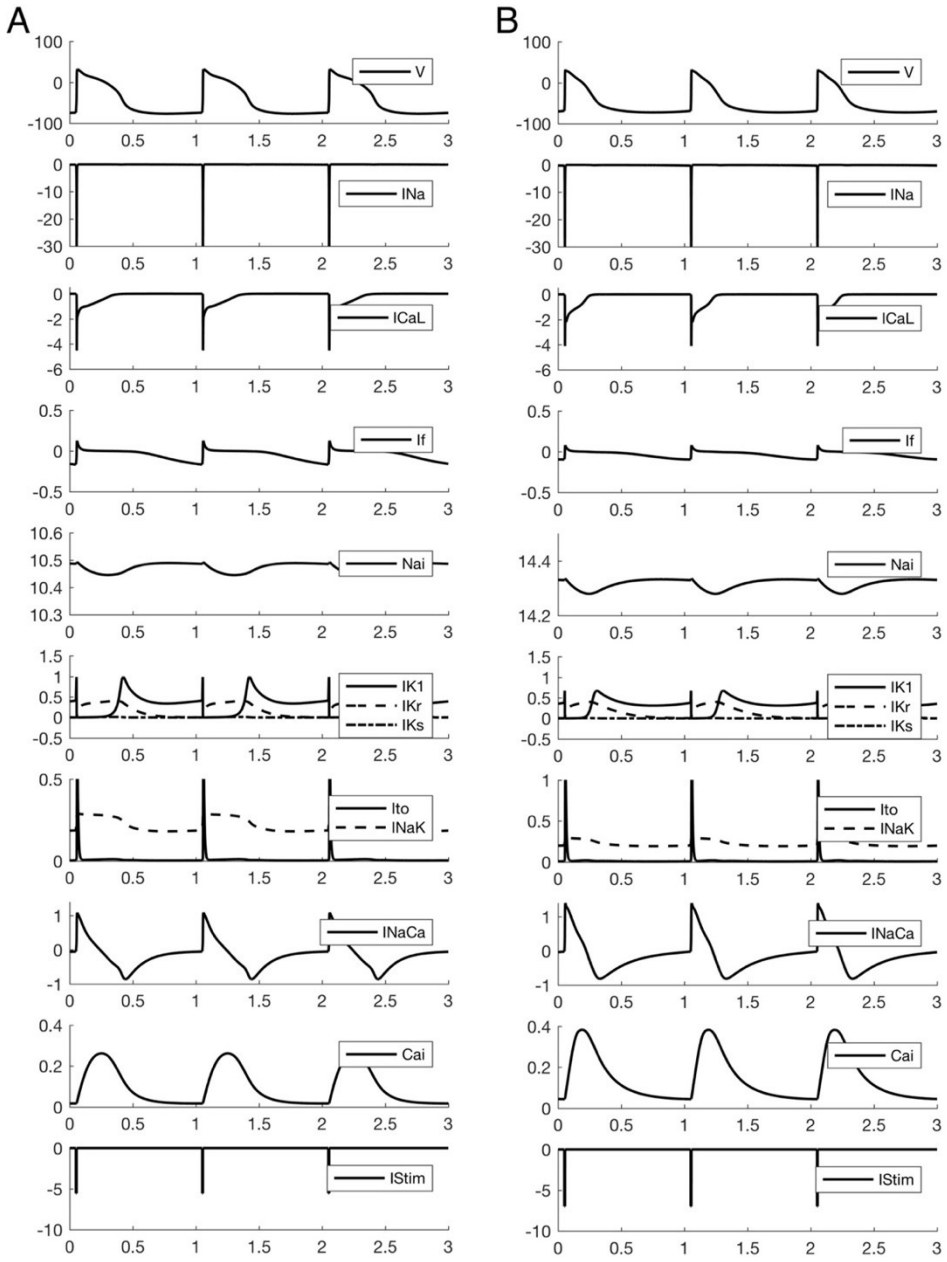

Figure 4.4 Steady state action potential, ion currents, and intracellular ion concentrations of hiPSC-CM computational model. (**A**) Ventricular-like hiPSC-CM, (**B**) Atrial-like hiPSC-CM. External pacing was applied at 1000 ms cycle length.

When variability was introduced to the conductance of each ion current in the baseline model, it led to deviations of steady-state action potentials from the baseline model as expected. Visually, this is demonstrated in Fig. 4.5A, where action potentials simulated from a population of 10000 independent cardiomyocytes with 10% variability in all conductances are shown. The spread in action potential morphology indicates the action potential variability, and can be quantified by IQR-APD_{80} similar to the experimental data. The corresponding histogram is shown in Fig. 4.5B, where a Gaussian-like distribution with a single peak was observed, which is expected since only the ventricular-like phenotype model was used to derive the heterogeneous population. Despite the variability introduced into the simulated cell population, the average action potential characteristics were largely unaffected, as indicated by the virtually unchanged average APD_{80} for the 4 different populations of simulated cells with 1%, 2%, 5% or 10% variability (Fig. 4.5C). However, the spread in APD_{80} increased with increased variability, as shown by the increased IQR-APD_{80} (Fig. 4.5D).

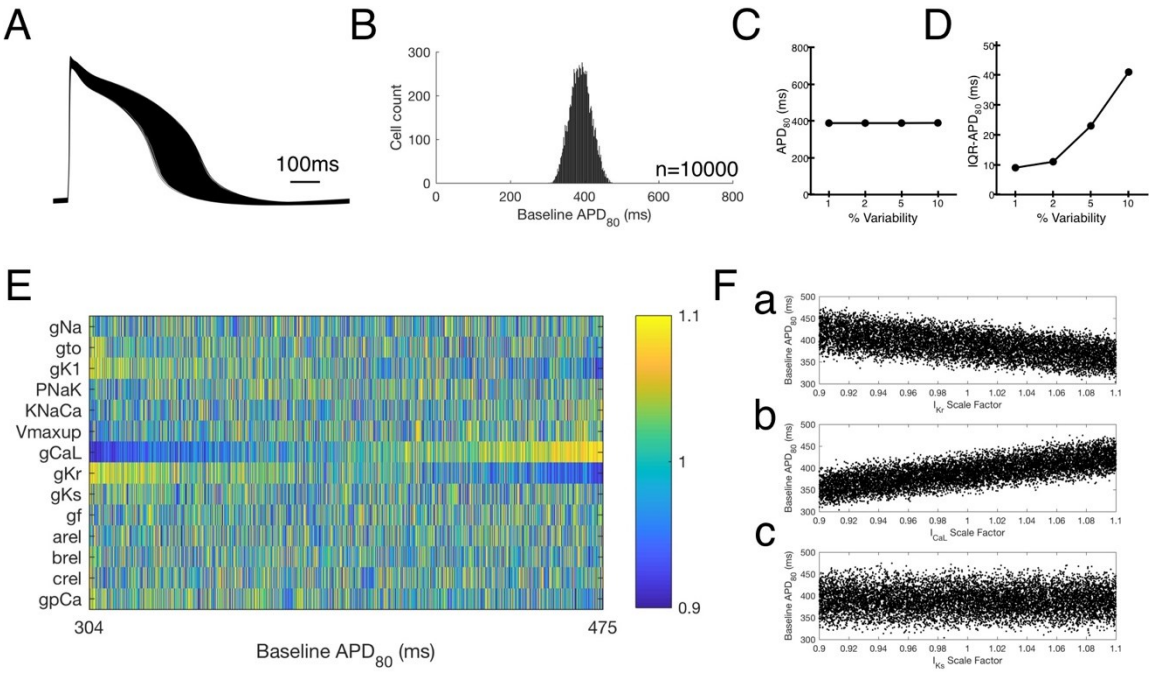

Figure 4.5 Single cell simulation of action potential variability. (**A**) Steady-state simulated action potentials of a population of independent cardiomyocytes with 10% variability paced at 1000 ms cycle length. (**B**) APD_{80} histogram of the population of simulated cardiomyocytes in A. (**C**) Average APD_{80} of 4 different populations of simulated cardiomyocytes with 1%, 2%, 5% or 10% variability. (**D**) IQR-APD_{80} of the 4 different populations of simulated cardiomyocytes in C. (**E**) Baseline APD_{80} and scale factors for all 14 conductances. Each row represents the scale factors for an individual ion current conductance, and each column corresponds to a single simulated cell. The columns were sorted by their baseline APD_{80} values to visually show correlation between baseline APD_{80} and multipliers of conductances. (**F**) Baseline APD_{80} dependency on scaling factors for three ion currents, demonstrating different types of correlations: a. I_{Kr}, showing negative correlation. b. I_{CaL}, showing positive correlation. c. I_{Ks}, showing lack of correlation.

The relative importance of each ion conductance in determining the baseline APD_{80} values is demonstrated in Fig. 4.5E, where each column represents the scale factors used for an individual cell in the heterogeneous population of simulated cells, color-coded by their values, and each row represents the scale factors used for an individual ion current across all 10000 cells. By sorting the columns in the ascending order of the baseline APD_{80} of corresponding cells, the correlation (or lack of correlation) between baseline APD_{80} and

each scale factor can be visualized. Among all conductances, it became apparent that gCaL and gKr are the predominant factors influencing baseline APD_{80}, since cells with reduced gCaL (as indicated by blue in the gCaL row) and with enhanced gKr (as indicated by yellow in the gKr row) are those have shorter baseline APD_{80}, and vice versa. This is also indicated by the negative correlation between baseline APD_{80} and I_{Kr} scale factor (Fig. 4.5F-a) and the positive correlation between baseline APD_{80} and I_{CaL} scale factor (Fig. 4.5F-b). On the other hand, other scale factors did not impact APD_{80} as strongly as for I_{Kr} or I_{CaL}, as indicated by the intermixed pattern of scale factors when sorted by baseline APD_{80} (Fig. 4.5E), and, in the example of I_{Ks}, the lack of correlation between baseline APD_{80} and its scale factor (Fig. 4.5F-c). The R-squared values for linear regression models between baseline APD_{80} and gKr, gCaL and gKs were 0.31, 0.51 and 0.0004, respectively, consistent with the observation of strong correlations with gKr or gCaL, and a weak correlation with gKs.

The effect of ion channel blockade on population heterogeneity was then investigated for I_{CaL} and I_{Kr}, because of their high correlation with baseline APD_{80}. Channel blockade was simulated by reducing the maximum conductances for I_{CaL} or I_{Kr} by 50% respectively, in a population with 10% variability across all ion channels. Overall, I_{CaL} blockade led to shortening of the action potentials (Fig. 4.6A), while I_{Kr} blockade led to prolongation of the action potentials (Fig. 4.6B). At a population level, I_{CaL} blockade caused a left shift in the APD_{80} histogram (Fig. 4.6C, black to blue) that is consistent with the shortening of action potentials, but did not affect the spread of the histogram. On the contrary, I_{Kr} blockade led to a wider spread in the APD_{80} histogram in addition to the overall right shift (Fig. 4.6C, black to red). The response in population variability can be

measured by IQR-APD_{80} as shown in Fig. 4.6D, where little change was observed with I_{CaL} blockade, and a dramatic increase was observed with I_{Kr} blockade. The mechanism of increased APD_{80} variability with I_{Kr} blockade was further investigated. Fig. 4.6E shows the dependency of ΔAPD_{80} on baseline APD_{80}. In general, a positive correlation was observed, where cells with longer baseline APD_{80} responded to I_{Kr} blockade more strongly, as indicated by the larger ΔAPD_{80}. However, there was also notable variability in ΔAPD_{80} even for cells with similar baseline APD_{80}, as evident by the large vertical spread in the scatter plot. Combined, the positive dependency on baseline APD_{80} and the high variability for cells with similar baseline APD_{80} led to the increase in IQR-APD_{80} with I_{Kr} blockade. Further, the correlation of ΔAPD_{80} to ion current scale factors is shown in Fig. 4.6F in a manner similar to Fig. 4.5E, except the columns (representing each cell) are now sorted by ΔAPD_{80}. Interestingly, there is a strong correlation between ΔAPD_{80} and PNaK, the maximum conductance for the Na^+-K^+ pump, while no correlation was apparent between ΔAPD_{80} and other ion current scale factors. This positive correlation is also demonstrated in the ΔAPD_{80} dependency on PNaK scale factor (Fig. 4.6G), where cells with higher PNaK values had longer ΔAPD_{80} when I_{Kr} was blocked by 50%. At the same time, ΔAPD_{80} variability was also greater for cells with larger PNaK scale factors, as indicated by the wider vertical spread in the scatter plot. On the contrary, ΔAPD_{80} did not have a strong correlation with the I_{Kr} scale factor with 50% I_{Kr} blockade (Fig. 4.6H). The R-squared values for linear regression models between ΔAPD_{80} and PNaK and gKr were 0.65 and 0.044, respectively, consistent with the observation of strong correlations with PNaK, and a weak correlation with gKs.

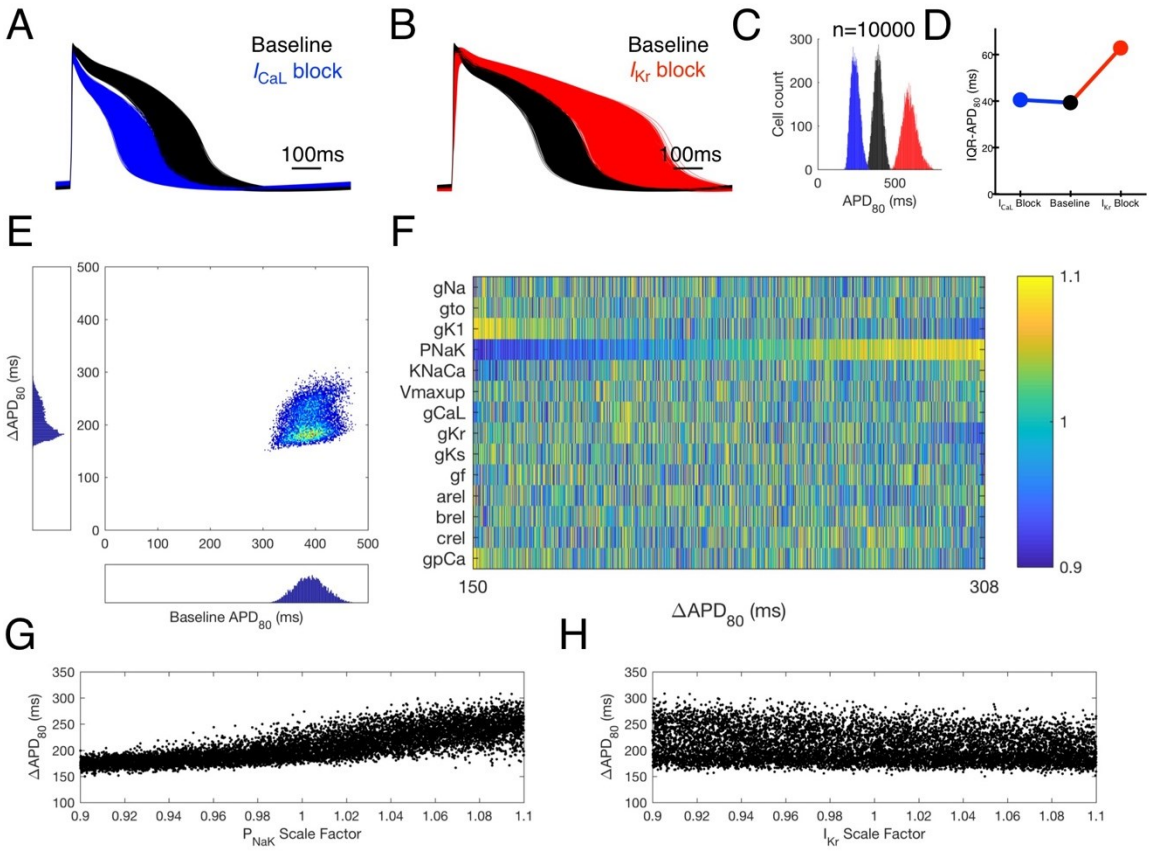

Figure 4.6 Ion channel blockade in heterogeneous population of independent cells. (**A,B**) Responses of a population of 10000 simulated hiPSC-CM populations with 10% variability and either 50% I_{CaL} (A), or I_{Kr} (B) blockade. (**C**) Histograms of APD_{80} at baseline (black), 50% I_{CaL} blockade (blue) or 50% I_{Kr} blockade (red) for the cell population in A, B. (**D**) IQR-APD_{80} changes with 50% I_{CaL} or I_{Kr} blockade. (**E**) ΔAPD_{80} dependency on baseline APD_{80} at 50% I_{Kr} blockade of the population shown in B. (**F**) ΔAPD_{80} dependency on scale factors for ion currents. Each row represents the scale factors for an individual ion current conductance, and each column corresponds to a single simulated cell. The columns were sorted by their responses to 50% I_{Kr} blockade, as measured by ΔAPD_{80}. (**G**) ΔAPD_{80} dependency on PNaK scale factor, showing a positive correlation. (**H**) ΔAPD_{80} dependency on I_{Kr} scale factor, showing a general lack of correlation.

4.3.4 Monolayer simulation of action potential variability

To further investigate the effect of electrophysiological variability on drug response in a syncytial context, a monolayer model was constructed with electrically coupled cells. For this section, 10% variability in ion channel conductance was used. Electrical coupling is expected to affect the observed action potential variability by allowing passive current to flow across neighboring cardiomyocytes and electronically averaging out differences in transmembrane voltage. When there was no electrical coupling among cells, action potentials recorded from individual sites within the simulated monolayer reflect their independent steady-state conditions, regardless of how they were distributed across the monolayer. An example of random distribution is shown in Fig. 4.7A. The intermixed pattern in the spatial APD_{80} map reflects the random distribution of the cells. The APD_{80} distribution shows a single Gaussian-like distribution representing the variability within this cell population. Electrical coupling nearly eliminated the action potential variability in this randomly distributed monolayer, as shown in Fig. 4.7B. The APD_{80} histogram became very narrow, and the action potentials were essentially identical across the monolayer. However, if cells with similar electrophysiological properties were allowed to group together, either radially (Fig. 4.7C), or linearly (Fig. 4.7D), the action potential variability was only slightly reduced by electrical coupling.

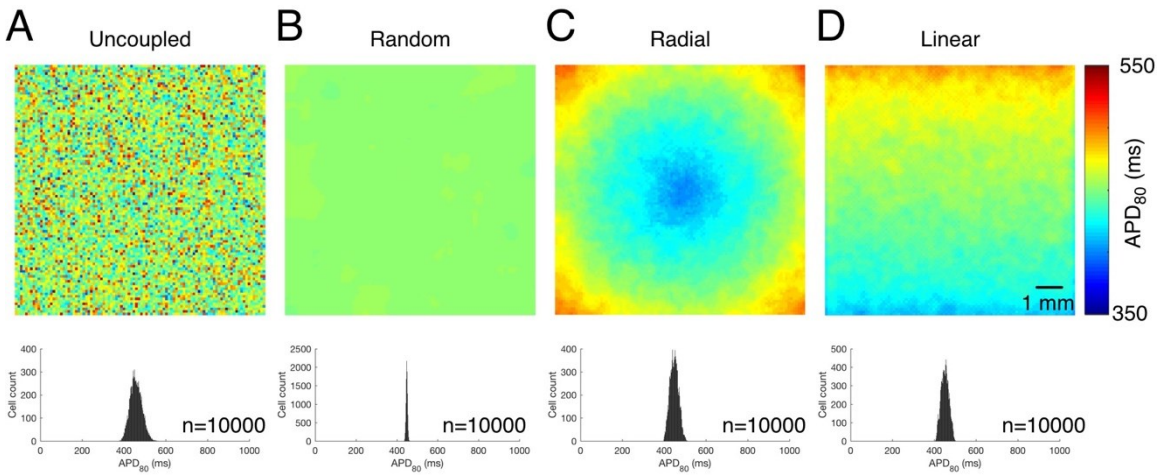

Figure 4.7 APD_{80} in cell monolayer simulations with electrical coupling. For each panel, top map shows APD_{80} across the monolayer, and bottom histogram shows APD_{80} distribution within the monolayer. (**A**) No electrical coupling among cells. (**B-D**) Electrical coupling was introduced across the monolayer. (**B**) Cells were randomly placed across the monolayer. (**C**) Cells were placed in the monolayer so that shorter APD ones are towards the center, while longer APD ones are towards the outside of monolayer. (**D**) Cells were placed in the monolayer so that shorter APD ones are towards the bottom edge of the monolayer while longer APD ones towards the top edge of the monolayer.

The monolayer with linear APD_{80} gradient as shown in Fig. 4.7D was then used to study the effect of I_{Kr} blockade on action potential variability and repolarization heterogeneity (Fig. 4.8). For this simulation, line pacing was applied on the left edge of the monolayer, so that a propagating action potential wave was initiated perpendicular to the APD_{80} gradient from left to right. Overall, 50% I_{Kr} blockade produced a prolongation in action potential, as shown by the right-shift of the APD_{80} histogram in red compared to the histogram in black in Fig. 4.8A. The action potential variability was also increased by the I_{Kr} blockade, indicated by the increased spread in APD_{80} histogram and the increased IQR-APD_{80} shown in Fig. 4.8B. The spatial variability in the APD_{80} is shown in Fig. 4.8C for baseline (a) and for 50% I_{Kr} blockade (b) conditions. With average APD_{80} subtracted across the entire monolayer for each case, these spatial APD_{80} variation maps demonstrate how

APD_{80} values deviate from the average. For both baseline and I_{Kr} blockade conditions, APD_{80} variation roughly followed a linear pattern, with cells towards the top edge of the monolayer having longer APD_{80} while cells towards the bottom row of the monolayer having shorter APD_{80}. In addition, I_{Kr} blockade increased the variation in APD_{80}, as indicated by the deeper red towards the top of monolayer, and the deeper blue towards the bottom of the monolayer. This is consistent with the increased spread in the overall APD_{80} histogram and increased IQR-APD_{80}. To investigate how increased APD_{80} variability affects its spatial gradient, the APD_{80} gradient was quantified along the direction of the line of pacing as shown in Fig. 4.8D. When APD_{80} was measured from cells at the same distance from the line of pacing (for example, along the dashed line in Fig. 4.8C) and plotted against distance from the bottom of the monolayer, the resulting scatter plot roughly follows a linear pattern (red dots in Fig. 4.8D). This linear pattern is reflective of the linear gradient used to construct the monolayer. When a line is fitted to the APD_{80} values, the slope of the line is a measurement of the APD_{80} gradient in the direction of the dashed line in Fig. 4.8C, which is parallel to the line of pacing. This measurement was repeated for different distances from the line pacing (noted by d in Fig. 4.8C-b) to calculate the APD_{80} gradient across the entire monolayer, which is shown in Fig. 4.8 E to be greater under conditions of 50% I_{Kr} blockade. Thus, the increased APD_{80} variation resulting from I_{Kr} blockade led to an increased spatial gradient in APD_{80}.

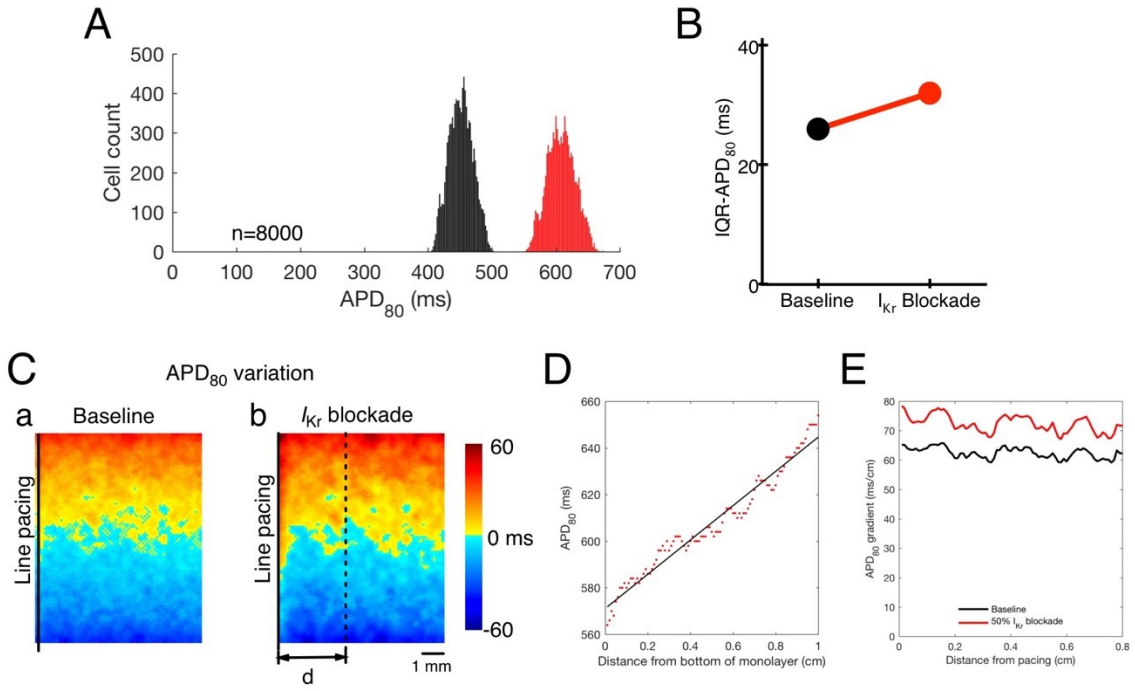

Figure 4.8 APD_{80} response to I_{Kr} blockade in simulated monolayer with defined linear variability. (**A**) APD_{80} histogram at baseline (black) or with 50% I_{Kr} blockade (red). (**B**) IQR-APD_{80} of the monolayer, showing an increase in action potential variability with I_{Kr} blockade. (**C**) APD_{80} variation map of this simulated monolayer at baseline (a) or with I_{Kr} blockade (b). The average APD_{80} was subtracted across the monolayer for each condition to highlight the variability. Orange/red region indicates cells with APD_{80} longer than average, and cyan/blue region indicates cells with APD_{80} shorter than average. Solid line indicates applied line pacing, and dashed line shows the direction along which the spatial gradient of APD_{80} was calculated. (**D**) Example of APD_{80} gradient calculation. Red dots indicate APD_{80} values measured along the dashed line in C-b, which is in parallel with the line of pacing. Solid line indicates linear fit of the APD_{80} data. The slope of the fitted line is the APD_{80} gradient along the direction parallel to the line of pacing. (**E**) APD_{80} gradient measured at different distances from the line of pacing, in the direction parallel to the line of pacing. Blue line indicates baseline condition, red line indicates 50% I_{Kr} blockade condition.

Next, repolarization heterogeneity was quantified as the local gradient of repolarization time, as shown in Fig. 4.9. The heterogeneity in action potentials led to a slight tilt in the activation wavefront, with conduction velocity being slightly faster on the bottom of monolayer where the action potential was shorter than on the top of monolayer

where the action potential was longer. (Fig. 4.9A-a). This was a result of the longer diastolic interval on the bottom than on the top, which gives more time for I_{Na} to recover and provide more excitatory current. This heterogeneity in conduction became greater with 50% I_{Kr} blockade, as shown in the more prominent tilt in the activation wavefronts (Fig. 4.9B-a). The repolarization time, which is the sum of activation time and APD_{80}, is shown in Fig. 4.9A-b for baseline and Fig. 4.9B-b for 50% I_{Kr} blockade condition. The isochone lines for repolarization time were also tilted, as a combined effect of tilted activation and heterogeneous APD_{80}. The spatial gradient of repolarization time was then calculated for each cell within the monolayer, which is a measurement of the difference in repolarization times in the local vicinity of each cell. The magnitude and direction of the local gradients are shown in Fig. 4.9A-c and Fig. 4.9B-c, and the histograms of the magnitude are shown in Fig. 4.9A-d and Fig. 4.9B-d. I_{Kr} blockade led to an increase in the repolarization time gradient across the monolayer, as indicated by the deeper red across the monolayer, as well as the right-shifted histogram. The increased repolarization time gradient indicates an increase in dispersion of repolarization, which is a potentially proarrhythmia marker.

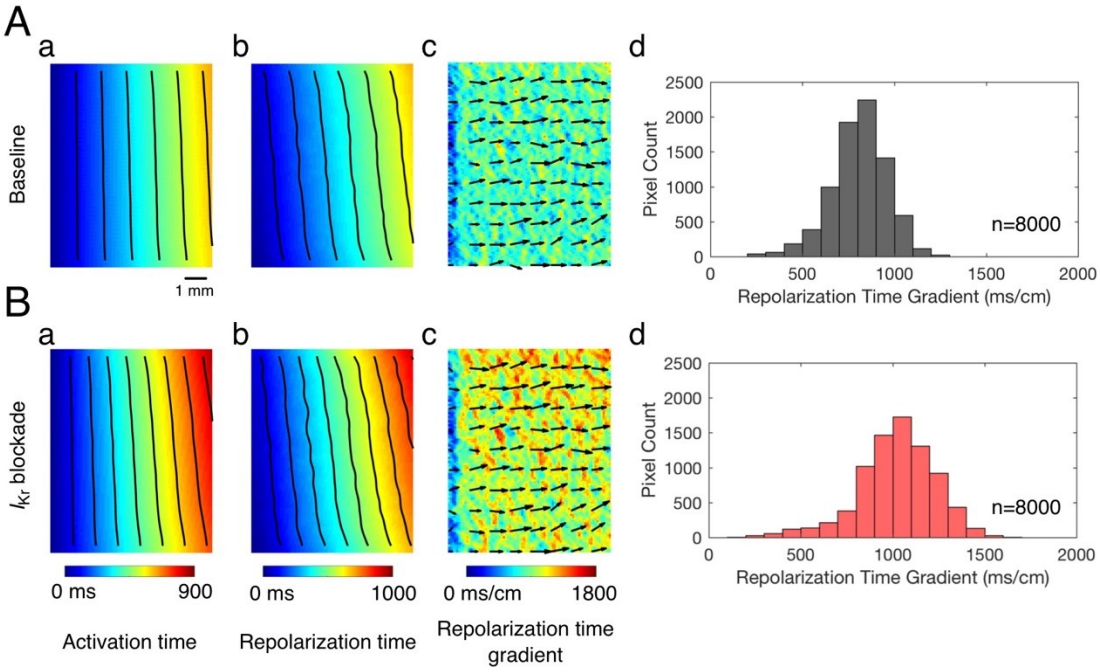

Figure 4.9 Repolarization time gradient response to I_{Kr} blockade. (**A**) Baseline and (**B**) 50% I_{Kr} blockade. In each condition: a. activation time across the monolayer. b. repolarization time across the monolayer. In a and b, isochrones have 100 ms spacing. c. local gradient of repolarization time calculated at the location of each cell in the simulated monolayer. Color map shows the magnitude of the gradient, and quiver plot shows the direction of the gradient. d. histogram of local repolarization time.

The propagating action potential wave also creates a heterogeneity in transmembrane potential (V_m) across the monolayer during repolarization, and the local gradient can be calculated for individual cells as shown in Fig. 4.10A-a. The quiver plot indicates the magnitudes and the directions of the local V_m gradients. For each cell within the monolayer, the V_m gradient was calculated for each time point during a propagating action potential wave, and the magnitude of the V_m gradient is shown in Fig. 4.10A-b for one cell as an example. There are two distinct peaks in the V_m gradient trace. The first, larger peak corresponds to the depolarizing wave front as it propagates across the cell. The second, smaller peak corresponds to the repolarizing wave tail as it propagates across the cell. The maximum V_m gradient during repolarization governs the intercellular current that

can pass during action potential repolarization and generate an ectopic beat, and is therefore a potential proarrhythmia index. Fig. 4.10B and Fig. 4.10C show the maximum V_m gradients calculated across the simulated monolayer at baseline and at 50% I_{Kr} blockade conditions, respectively. I_{Kr} blockade led to an increase in the maximum V_m gradient throughout the monolayer, as indicated by the deeper red regions found in the spatial map (Fig. 4.10B-a,C-a) and right-shift found in the histograms (Fig. 4.10B-b,C-b) for the blockade condition.

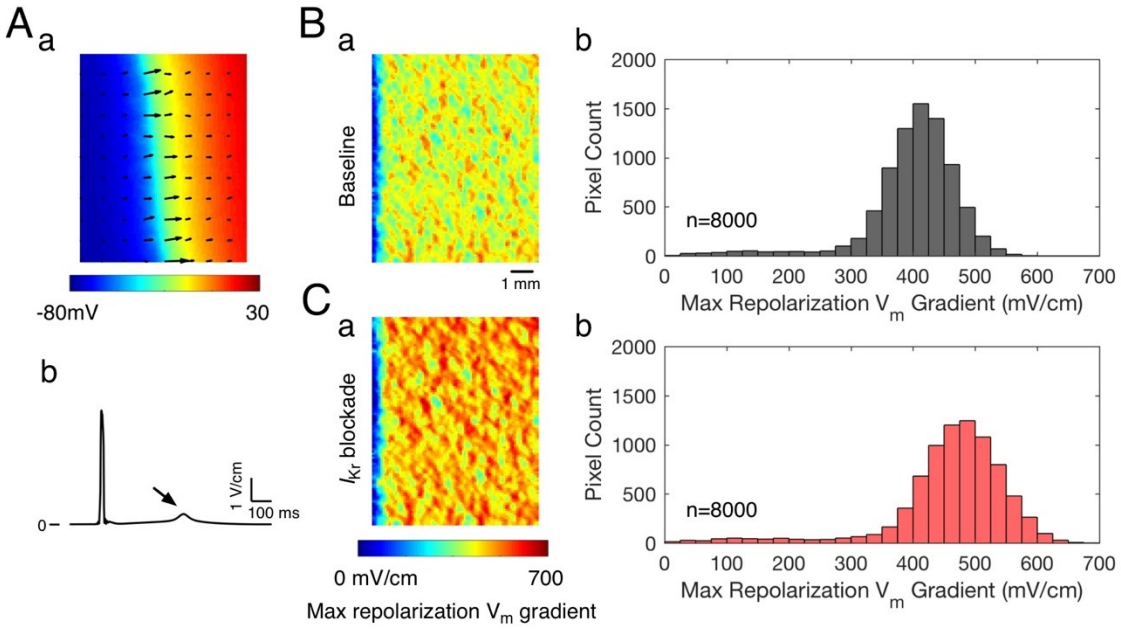

Figure 4.10 Maximum V_m gradient during repolarization. (**A**) Calculation of V_m gradient of a propagating action potential wave. a. snapshot of V_m across the monolayer during a propagating action potential. The wave front has just left the right edge of the monolayer. Quivers shows local V_m gradients and their directions. b. magnitude of V_m gradient calculated at different time points of a propagating action potential wave. Arrow indicate maximum repolarization V_m gradient. (**B**) Maximum repolarization V_m gradient during baseline and (**C**) 50% I_{Kr} blockade. For B and C: a. map of maximum V_m gradient measured during repolarization for each cell within the monolayer. b. histograms of maximum V_m gradient measured during repolarization.

4.4 Discussion

The key to a good in vitro model for drug-induced proarrhythmia is determining the set of biomarkers that best predicts drug effects. Electrophysiological properties measured by optical mapping of cm-sized monolayers of hiPSC-CMs provide the basis for establishing a suitable set of biomarkers. Among these properties, some are similar to those obtained by patch clamp or MEAs, such as action potential duration and EAD occurrence; some are tissue-level properties that cannot be measured with single cells or small clusters, such as conduction velocity; and yet others are population properties that are revealed by the monolayers used in the current study, such as variabilities.

An *in vitro* platform for testing drug-induced proarrhythmia should be validated by showing appropriate responses to cardioactive drugs with relatively selective known effects. Previous studies have shown that hiPSC-CMs are promising in this aspect (Blinova et al., 2017; Dick et al., 2010; Lu et al., 2017), but the results can be confounded by the immaturity and heterogeneity of the cells (Sinnecker et al., 2014). The 4 selective ion channel blockers (E-4031, nifedipine, nexiletine and JNJ303) as provided by the CiPA initiative are designed to test if Axiogenesis Cor.4U cardiomyocyte monolayers respond to specific channel blockers in the expected ways. Of the 4 drugs, E-4031 is generally considered selective to I_{Kr}, without affecting I_{Na} or I_{Ca} in concentrations up to 10 μM (Wettwer et al., 1991). Nifedipine is an L-type calcium channel blocker of the dihydropyridine family and also generally considered to be selective. It can, however, block the T-type calcium current at concentrations above 1 μM (McDonald et al., 1994). Mexiletine is an I_{Na} blocker, although at concentrations higher than 300 μM it can also inhibit Ca^{2+} and Na^{+}/K^{+} pump current (Honerjäger et al., 1986). JNJ303 is a potent I_{Ks}

blocker, with an IC_{50} for I_{Ks} at 0.064 μM and for other major cardiac ion channels much higher than 1 μM (Towart et al., 2009). The concentrations tested for each drug were much lower than the concentrations reported for their respective non-specific blockade effects, and therefore in theory these 4 drugs should serve as specific ion channel blockers. The responses of Axiogenesis Cor.4U cardiomyocyte monolayers generally reflected the expected responses based on drug mechanism: prolongation of action potential with I_{Kr} blockade with E-4031, and shortening of action potential with I_{CaL} blockade with nifedipine. Qualitatively, Cor.4U cardiomyocyte monolayers were more sensitive to E-4031 compared to guinea pig papillary muscles as previously suggested (Wettwer et al., 1991) and as indicated by a more prominent prolongation in APD. This increased sensitivity could arise if hiPSC-CMs have reduced repolarization, as previously demonstrated in a simulation study (Paci et al., 2015). The I_{Na} blocker, mexiletine, also prolonged the action potential but to a much lesser degree than E-4031. The prolongation in repolarization was also observed previously using hPSC-CMs and MEAs, but in those studies it could be a secondary effect of the slowing of spontaneous rate with mexiletine, as when beating rate was corrected for, no significant changes in the corrected FPD (**FPDc**) were observed (Clements and Thomas, 2014; Harris et al., 2013). In this study, pacing rate was fixed at 1000ms cycle length and therefore no correction for APD was necessary. The prolongation in APD_{80} observed here could be an effect secondary to the reduced excitability because of I_{Na} block. Mexiletine is also an example of the utility of the monolayer model, in that the effect of I_{Na} blockade is faithfully captured by the slowing in conduction velocity. On the other hand, I_{Ks} blocker JNJ303 did not produce any meaningful response in Cor.4U monolayers, suggesting either Cor.4U cardiomyocytes lack expression

of I_{Ks}, or I_{Ks} has a limited effect in determining APD in the Cor.4U cardiomyocyte monolayers, as was the case in rabbit ventricular muscle (Lengyel et al., 2001). The increased sensitivity to I_{Kr} blockade suggests reduced repolarization reserve in Cor.4U cardiomyocytes and therefore seems to support the former possibility. On the other hand, expression of I_{Ks} has been reported in hiPSC-CMs, and prolongation of action potentials (Jonsson et al., 2012; Peng et al., 2010) or field potential durations (Honda et al., 2011; Nozaki et al., 2014) was observed using a different I_{Ks} blocker, chromanol 293B. These different observations indicate further work to improve consistency in hiPSC-CM characteristics is still needed.

The unique structure of the hERG protein makes it a likely target of unintentional binding to a wide range of drugs (Mitcheson and Perry, 2003), and also makes it a primary target for drug screening under current guidelines. The drugs with mixed or off-target channel blocking effects tested in this chapter (flecainide, quinidine, ranolazine and moxifloxacin) have all been shown to interact with hERG at concentrations relevant to the concentrations tested in the CiPA phase 1 study (Antzelevitch et al., 2004; Colatsky, 1982; Kang et al., 2001; Slawsky and Castle, 1994). In Cor.4U monolayers this I_{Kr} interaction was manifested as prolongation of the action potential. Further, flecainide and quinidine, the two I_{Na} blockers, also led to a reduction in conduction velocity across the monolayer in addition to the prolongation of APD. The moxifloxacin-induced increase in IQR-APD_{80} and appearance of two peaks in the APD_{80} histogram is rather interesting, as this emerging separation of phenotypes was not observed with any other drugs, including those that increased IQR-APD_{80} (E-4031, mexiletine and flecainide). This could suggest that the I_{Kr} blocking effect associated with moxifloxacin is different from that of E-4031 (which

increased IQR-APD_{80} but did not lead to two peaks in the APD_{80} histogram), and that cellular heterogeneity in monolayer culture can still manifest different observed phenotypes under certain conditions. Overall, these observations demonstrate that the monolayer model can be a promising platform for the integrated evaluation of drugs that affect multiple aspects of cardiac electrophysiology.

The heterogeneity in hiPSC-CM phenotypes can complicate the interpretation of drug response in these cells (Sinnecker et al., 2014), since drugs can have differential effects on the cardiomyocytes. In **Chapter 2**, I have shown that monolayer culture promoted a single phenotype in Cor.4U cardiomyocytes, despite the manufacturer's specification of a mixed population (Kettenhofen et al., 2014). This provides a consistent baseline for drug response testing. Further, even within a single monolayer, the response to drug is evaluated at over 6000 recording sites simultaneously across the monolayer. The uniform response within individual monolayers to all compounds tested further demonstrated the similarity in electrophysiology of cells in monolayer culture. In addition, variability in monolayers is affected strongly by some drugs (E-4031, mexiletine, moxifloxacin and quinidine), slightly by other drugs (quinidine and ranolazine), and little by the remaining drugs (nifedipine and JNJ303). Drug-induced increase in heterogeneity can potentially be a biomarker for proarrhythmia, which can be accentuated further by experimental approximations of in vivo heterogeneity of the myocardium. One limitation to the monolayer approach, however, is that monolayer culture requires a larger number of cells compared to smaller clusters used with MEAs or single cells with patch clamp. In the CiPA phase 1 study, this limitation resulted in only one monolayer being tested for each drug. This limitation is partially compensated for by the large number of APs recorded

within each monolayer, as well as the high consistency in APs within and across monolayers.

Simulations can provide insight on population properties. Both maximum conductance and gating parameters have been altered to model electrophysiological variability in cardiomyocyte models (Romero et al., 2009) and produced variation in APD as a result. Only scaling of conductance, and not changes in kinetics, was used for studies in this chapter to simulate biological variation in channel expression, and the result is consistent with the expectation of creating a heterogeneous population of action potentials. The computational APD_{80} histogram also shares qualitative similarity to that observed with monolayer mapping, resembling a single peak Gaussian-like distribution. One interesting finding in simulations of the single cell population is the increase in variability with blockade of I_{Kr}. The blockade of I_{Kr} was modeled by a reduction in its maximum conductance gKr by a factor of 50%, which simulates the blockade of the current-conducting pore of the channel. Therefore, the blockade also reduces the variability in gKr by 50%. One may expect that this reduction in gKr would reduce the variability in I_{Kr}, which in turn should reduce overall action potential variability. However, the opposite result was observed in simulations, which showed that that prolongation of the action potential by I_{Kr} blockade also extended the duration of the plateau phase, which reflects the precise balance between inward and outward ion currents and is very sensitive to small changes in individual ion currents. Despite reduced variability in gKr, the action potential variability can increase because of the variability in other ion currents. A previous study using human and canine ventricular myocytes demonstrated that the response to I_{Kr} blockade is indeed affected by variability in ion currents to different extents (Sarkar and

Sobie, 2011). In the hiPSC-CM case shown in this chapter, the variability in I_{NaK} (an outward current that repolarizes V_m) turned out to be highly correlated to the response variability to I_{Kr} blockade, suggesting that I_{NaK} is an important reserve current during repolarization in this hiPSC-CM model.

Computational models of electrically coupled monolayers of cardiomyocytes have the flexibility to create arbitrary distributions of heterogeneity. Different distributions of a heterogeneous population of cells in the presence of electrical coupling resulted in large differences in APD variability: electrical coupling nearly abolished variability if cells were randomly distributed, while this variability remained clearly visible if the cells were distributed in an organized manner, either radially or linearly. This observation suggests that an intermixed distribution of cells having heterogeneous electrophysiology is unlikely. Since synchronized electrical activity is capable of causing long term remodeling and maturation in hiPSC-CMs (Chan et al., 2013; Lieu et al., 2013), it could also reduce the differences in their electrophysiology. In either case, the observed variability is reduced compared to the uncoupled state.

The asynchronous repolarization in human heart determines the morphology of the T wave in human ECG. A change in T wave morphology, which reflects a change in repolarization heterogeneity, has been linked to hERG blockade and proarrhythmic risk in human (Hanton, 2014; Vicente et al., 2015). The computational model of an hiPSC-CM monolayer with linear APD gradient described in this chapter provides an *in silico* platform to test this important proarrhythmia biomarker. Similar to observations in isolated hiPSC-CM populations, I_{Kr} blockade also led to an increase in APD_{80} variability, which is manifested as an increase in the spatial gradient of APD_{80} in the monolayer model. At the

tissue level, the increased APD_{80} gradient by I_{Kr} blockade further increased the repolarization gradient in two ways: 1) increase of the repolarization time gradient (Fig. 4.9) and 2) increase of the maximum V_m gradient during repolarization (Fig. 4.10). Both of these metrics of repolarization gradient are potentially proarrhythmic. The increased repolarization time gradient increases the heterogeneity in refractory state across the monolayer, which in turn affects excitability and can potentially lead to proarrhythmic unidirectional conduction block. The increased maximum V_m gradient during repolarization can increase the flow of intercellular current, which, when exceeding a certain threshold, will trigger ectopic activities such as EADs. Taken together, in a monolayer with defined heterogeneity, biomarkers such as repolarization gradient can be measured for assessing drug-induced proarrhythmia risk.

In conclusion, a monolayer model using Cor.4U cardiomyocytes exhibited expected responses to cardioactive drugs. For drugs with mixed channel blocking effects, individual effects can be captured by separate electrophysiological properties. Computational simulations of heterogeneous populations of hiPSC-CMs demonstrated channel blockers can affect action potential variability, and in monolayer models with defined heterogeneity, the repolarization gradient provides another potential biomarker for testing drug-induced proarrhythmia.

Chapter 5

Conclusions

5.1 Summary of findings

In my thesis, I investigated the utility of hPSC-CMs for *in vitro* cardiac electrophysiology studies. Population-based analysis of action potential variability was first investigated in an hEB model and then in a monolayer-based model. It was found that the monolayer model promotes similarity in the electrophysiology of hPSC-CMs, which provides a consistent baseline for downstream studies. Using this idea, an LQT2 disease model with hiPSC-CMs was then studied. Compared to single cell and small cluster models, the monolayer LQT2 model had prolonged action potentials and increased sensitivity to I_{Kr} blockade, but lacked EAD formation, although EADs were observed when the dimension of the monolayer was reduced. Conduction heterogeneity can also be induced either by premature pacing, or by creating local hypoxia in the monolayer model, for assessing disease-enhanced proarrhythmia. Lastly, the utility of the monolayer model

as a platform for testing drug-induced proarrhythmia was investigated. Monolayers of Cor.4U cardiomyocytes were shown to respond to cardioactive drugs with known effects in an expected manner, in both action potential measurements and conduction velocity properties. The monolayers also responded to mixed-effect drugs, with a combination of responses that are consistent with the drug interactions with ion channels. Computational models were used to simulate population variability in hiPSC-CMs, and the effect of I_{Kr} blockade was shown to increase, rather than decrease, the population variability. Monolayer simulations demonstrated electrical coupling will reduce variability observed in a heterogeneous population, but the effect was smaller when cells with similar properties were clustered together. They also demonstrated the utility of monolayers with defined heterogeneity in drug-induced proarrhythmia screening, where gradients in APD_{80} and repolarization time are candidates as proarrhythmia biomarkers.

5.2 Future directions

In **Chapter 2**, I demonstrated phenotype identification using an objective, waveform-based automated algorithm and compared the results with AP parameter-based methods. Advanced methods based on morphological changes have since been used to improve the algorithm (Gorospe et al., 2015). These objective algorithms can be used as a framework for more general studies to identify subgroups in large electrophysiological datasets, and how they evolve over time in a more dynamic setting. For example, during maturation, how does the action potential evolve to a more adult-like phenotype? Do ventricular-, atrial- and nodal-like phenotypes further diversify, or converge under different culture conditions? Drug testing using hiPSC-CMs can also benefit from automated

grouping algorithms. For example, can the responses in action potential to drugs be separated into groups, and how do these groups correspond to the mechanism of action of the drug? Can drug-induced proarrhythmia be stratified based on the grouping results of an automated algorithm?

An immediate question following the observation of monolayer culture promoting a single electrophysiological phenotype is to further investigate its mechanism. In this thesis, I showed that acute treatments, including reduced electrical coupling and blockade of I_{Kr}, did not lead to phenotype separation. However, CBX treatment only reduces, rather than eliminates intercellular electrical coupling, which limits the interpretation of a single phenotype in monolayers. Nevertheless, experiments with acute treatments to reduce electrical cell-cell coupling cannot replace electrophysiological assays of truly independent (separated) hPSC-CMs, and it would be interesting to compare the electrophysiological phenotypes of single cells and monolayers of hPSC-CMs that are otherwise the same. Further, it would also be interesting to study the time course over which the different phenotypes of individual cells converge, which will shed light on the time course over which the electrophysiological phenotype of hPSC-CMs can change. Environmental cues can then be applied to monolayer cultures to investigate their effect on the different phenotypes across the cell population to further investigate the mechanism of the emerging single phenotype. Instead of acute experiments with a voltage-sensitive dye that only allows assessment of short-term responses (typically less than one hour), genetically encoded voltage and/or calcium sensors can be used for multi-time point assessment and the analysis of the dynamics of electrophysiology variability. For example, do cell phenotypes still converge if electrical coupling is prevented or impaired during culture?

How does in-culture electrical stimulation affect the variability in monolayer models? Further, I have also shown evidence that physical dimension affects the electrophysiology of hPSC-CMs in an LQT2 diseased model. It is worth examining its mechanism by applying electrophysiological variability analysis to monolayers of different dimensions and geometry. Population analysis can also be applied to other tissue engineering models with large population of cells grown in different ways, such as with micro- or nano-patterned substrates, decellularized extracellular matrix, 3-dimensional culture systems, etc. The manifestation of cellular variability in each of these models can give insight on cell-cell interactions and phenotype development within each model.

Novel gene editing methods such as CRISPR/Cas9 can introduce precise mutations in cell lines, which can be used to generate isogenic cell lines with specified mutations and further strengthen *in vitro* disease modeling with hiPSCs. The study with LQT2-A422T cardiomyocytes will also benefit from gene editing methods. By correcting the point mutation in the diseased cell line and/or introducing the A422T mutation to a control cell line, the genotype-phenotype relationship can be better investigated. However, despite being an exciting new technology, CRISPR/Cas9 methods still have limitations when applied to specific mutations. For example, the availability of appropriate protospacer adjacent motif (**PAM**) sites around the hERG-A422T mutation site may not be ideal for the current Cas9 endonuclease-based system, and the low efficiency of homology directed repair (**HDR**) may post challenges in selecting successfully edited clones of hiPSCs.

In **Chapter 4**, computational modeling demonstrated that ion channel blockers can affect the repolarization gradient in monolayers. How this relates to arrhythmogenisis requires further investigation. Repolarization gradients lead to differential excitability in

the tissue, which creates a substrate for transient unidirectional conduction block. This can potentially lead to reentrant action potential propagation given the right stimulation conditions. Perhaps the change in repolarization gradient can be related to the time window during which the tissue is vulnerable to transient conduction block. This vulnerable window can be a quantifiable tissue-level biomarker for proarrhythmia risk. It is also worth exploring different predetermined APD gradients, as well as their effect on paced propagating action potentials. One approach, for example, would be to simulate the physiological gradient found across the ventricular wall, where data from canine experiments are available for differences in ion currents that are responsible for action potential heterogeneity, and data from human ventricle wedge preparations can provide a physiological baseline of APD heterogeneity.

5.3 Conclusions

My thesis work introduced a novel method to investigate the electrophysiology of hPSC-CMs by studying their tissue-level properties such as variability in large populations. It was inspired by the orchestrated activities in the human heart, and I have demonstrated that by allowing interactions among hPSC-CMs, similarities in their electrophysiology arise and a single phenotype emerges in a monolayer model. The utility of this monolayer model was then demonstrated in modeling LQT2 disease and studying drug response of hPSC-CMs, where tissue-level properties such as APD-dependency of drug responses and repolarization gradients were used to investigate disease- or drug- induced proarrhythmia. Future work is still needed to expand this framework to more disease models and extend

the library of drugs tested, and new tissue-level proarrhythmia biomarkers may be established as a result.

References

Abdi, H., Williams, L.J., 2010. Principal component analysis. Wiley Interdiscip Rev Comput Stat 2, 433–459.

Anderson, C.L., Delisle, B.P., Anson, B.D., Kilby, J.A., Will, M.L., 2006. Most LQT2 mutations reduce Kv11. 1 (hERG) current by a class 2 (trafficking-deficient) mechanism. Circulation 99, 321–325.

Anderson, C.L., Kuzmicki, C.E., Childs, R.R., Hintz, C.J., Delisle, B.P., January, C.T., 2014. Large-scale mutational analysis of Kv11.1 reveals molecular insights into type 2 long QT syndrome. Nat Commun 5, 5535.

Antzelevitch, C., Belardinelli, L., Zygmunt, A.C., Burashnikov, A., Di Diego, J.M., Fish, J.M., Cordeiro, J.M., Thomas, G., 2004. Electrophysiological effects of ranolazine, a novel antianginal agent with antiarrhythmic properties. Circulation 110, 904–910.

Ardehali, R., Ali, S.R., Inlay, M.A., Abilez, O.J., Chen, M.Q., Blauwkamp, T.A., Yazawa, M., Gong, Y., Nusse, R., Drukker, M., 2013. Prospective isolation of human embryonic stem cell-derived cardiovascular progenitors that integrate into human fetal heart tissue. Proc Natl Acad Sci 110, 3405–3410.

Baró, I., Escande, D., 2008. Basic Physiology of Ion Channel Function, in: Electrical Diseases of the Heart. Springer, London, London, pp. 11–23.

Bauwens, C.L., Peerani, R., Niebruegge, S., Woodhouse, K.A., Kumacheva, E., Husain, M., Zandstra, P.W., 2008. Control of human embryonic stem cell colony and aggregate size heterogeneity influences differentiation trajectories. Stem Cells 26, 2300–2310.

Bellin, M., Casini, S., Davis, R.P., D'Aniello, C., Haas, J., Ward-van Oostwaard, D., Tertoolen, L.G.J., Jung, C.B., Elliott, D.A., Welling, A., Laugwitz, K.-L., Moretti, A., Mummery, C.L., 2013. Isogenic human pluripotent stem cell pairs reveal the role of a KCNH2 mutation in long-QT syndrome. EMBO J 32, 3161–3175.

Ben-Ari, M., Naor, S., Zeevi-Levin, N., Schick, R., Ben Jehuda, R., Reiter, I., Raveh, A., Grijnevitch, I., Barak, O., Rosen, M.R., Weissman, A., Binah, O., 2016. Developmental changes in electrophysiological characteristics of human-induced pluripotent stem cell-derived cardiomyocytes. Heart Rhythm 13, 2379–2387.

Benjamin, E.J., Blaha, M.J., Chiuve, S.E., Cushman, M., Das, S.R., Deo, R., de Ferranti, S.D., Floyd, J., Fornage, M., Gillespie, C., Isasi, C.R., Jiménez, M.C., Jordan, L.C., Judd, S.E., Lackland, D., Lichtman, J.H., Lisabeth, L., Liu, S., Longenecker, C.T., Mackey, R.H., Matsushita, K., Mozaffarian, D., Mussolino, M.E., Nasir, K., Neumar, R.W., Palaniappan, L., Pandey, D.K., Thiagarajan, R.R., Reeves, M.J., Ritchey, M., Rodriguez, C.J., Roth, G.A., Rosamond, W.D., Sasson, C., Towfighi, A., Tsao, C.W., Turner, M.B., Virani, S.S., Voeks, J.H., Willey, J.Z., Wilkins, J.T., Wu, J.H., Alger, H.M., Wong, S.S., Muntner, P., American Heart Association Statistics Committee and Stroke Statistics Subcommittee, 2017. Heart disease and stroke statistics-2017

update: a report from the american heart association. Circulation 135, e146–e603.

Bett, G.C.L., Kaplan, A.D., Lis, A., Cimato, T.R., Tzanakakis, E.S., Zhou, Q., Morales, M.J., Rasmusson, R.L., 2013. Electronic "expression" of the inward rectifier in cardiocytes derived from human-induced pluripotent stem cells. Heart Rhythm 10, 1903–1910.

Bett, G.C.L., Kaplan, A.D., Rasmusson, R.L., 2016. Action potential shape Is a crucial measure of cell type of stem cell-derived cardiocytes. Biophys J 110, 284–286.

Bhattacharya, S., Burridge, P.W., Kropp, E.M., Chuppa, S.L., Kwok, W.-M., Wu, J.C., Boheler, K.R., Gundry, R.L., 2014. High efficiency differentiation of human pluripotent stem cells to cardiomyocytes and characterization by flow cytometry. J Vis Exp 52010.

Bischoff, U., Schmidt, C., Netzer, R., Pongs, O., 2000. Effects of fluoroquinolones on HERG currents. Eur J Pharmacol 406, 341–343.

Bishop, M.J., Gavaghan, D.J., Trayanova, N.A., Rodriguez, B., 2007. Photon scattering effects in optical mapping of propagation and arrhythmogenesis in the heart. J Electrocardiol 40, S75–80.

Blazeski, A., Zhu, R., Hunter, D.W., Weinberg, S.H., Boheler, K.R., Zambidis, E.T., Tung, L., 2012a. Electrophysiological and contractile function of cardiomyocytes derived from human embryonic stem cells. Prog Biophys Mol Biol 110, 178–195.

Blazeski, A., Zhu, R., Hunter, D.W., Weinberg, S.H., Zambidis, E.T., Tung, L., 2012b. Cardiomyocytes derived from human induced pluripotent stem cells as models for normal and diseased cardiac electrophysiology and contractility. Prog Biophys Mol Biol 110, 166–177.

Blinova, K., Stohlman, J., Vicente, J., Chan, D., Johannesen, L., Hortigon-Vinagre, M.P., Zamora, V., Smith, G., Crumb, W.J., Pang, L., Lyn-Cook, B., Ross, J., Brock, M., Chvatal, S., Millard, D., Galeotti, L., Stockbridge, N., Strauss, D.G., 2017. Comprehensive translational assessment of human-induced pluripotent stem cell derived cardiomyocytes for evaluating drug-induced arrhythmias. Toxicol Sci 155, 234–247.

Boheler, K.R., Bhattacharya, S., Kropp, E.M., Chuppa, S., Riordon, D.R., Bausch-Fluck, D., Burridge, P.W., Wu, J.C., Wersto, R.P., Chan, G.C.F., Rao, S., Wollscheid, B., Gundry, R.L., 2014. A human pluripotent stem cell surface N-glycoproteome resource reveals markers, extracellular epitopes, and drug targets. Stem Cell Reports 3, 185–203.

Boukens, B.J., Sulkin, M.S., Gloschat, C.R., Ng, F.S., Vigmond, E.J., Efimov, I.R., 2015. Transmural APD gradient synchronizes repolarization in the human left ventricular wall. Cardiovasc Res 108, 188–196.

Boukens, B.J., Walton, R., Meijborg, V.M., Coronel, R., 2016. Transmural electrophysiological heterogeneity, the T-wave and ventricular arrhythmias. Prog Biophys Mol Biol 122, 202–214.

Braam, S.R., Mummery, C.L., 2010. Human stem cell models for predictive cardiac safety pharmacology. Stem Cell Res 4, 155–156.

Braam, S.R., Tertoolen, L., van de Stolpe, A., Meyer, T., Passier, R., Mummery, C.L., 2010. Prediction of drug-induced cardiotoxicity using human embryonic stem cell-derived cardiomyocytes. Stem Cell Res 4, 107–116.

Britton, O.J., Bueno-Orovio, A., Van Ammel, K., Lu, H.R., Towart, R., Gallacher, D.J.,

Rodriguez, B., 2013. Experimentally calibrated population of models predicts and explains intersubject variability in cardiac cellular electrophysiology. Proc Natl Acad Sci 110, E2098–105.

Burridge, P.W., Holmström, A., Wu, J.C., 2015. Chemically defined culture and cardiomyocyte differentiation of human pluripotent stem cells. Curr Protoc Hum Genet 87, 21.3.1–21.3.15.

Burridge, P.W., Thompson, S., Millrod, M.A., Weinberg, S., Yuan, X., Peters, A., Mahairaki, V., Koliatsos, V.E., Tung, L., Zambidis, E.T., 2011. A universal system for highly efficient cardiac differentiation of human induced pluripotent stem cells that eliminates interline variability. PLoS ONE 6, e18293.

Burridge, P.W., Zambidis, E.T., 2013. Highly efficient directed differentiation of human induced pluripotent stem cells into cardiomyocytes. Methods Mol Biol 997, 149–161.

Carvajal-Vergara, X., Sevilla, A., D'Souza, S.L., Ang, Y.-S., Schaniel, C., Lee, D.-F., Yang, L., Kaplan, A.D., Adler, E.D., Rozov, R., Ge, Y., Cohen, N., Edelmann, L.J., Chang, B., Waghray, A., Su, J., Pardo, S., Lichtenbelt, K.D., Tartaglia, M., Gelb, B.D., Lemischka, I.R., 2010. Patient-specific induced pluripotent stem-cell-derived models of LEOPARD syndrome. Nature 465, 808–812.

Caspi, O., Itzhaki, I., Kehat, I., Gepstein, A., Arbel, G., Huber, I., Satin, J., Gepstein, L., 2009. In vitro electrophysiological drug testing using human embryonic stem cell derived cardiomyocytes. Stem Cells Dev 18, 161–172.

Cerignoli, F., Charlot, D., Whittaker, R., Ingermanson, R., Gehalot, P., Savchenko, A., Gallacher, D.J., Towart, R., Price, J.H., McDonough, P.M., Mercola, M., 2012. High throughput measurement of Ca^{2+} dynamics for drug risk assessment in human stem

cell-derived cardiomyocytes by kinetic image cytometry. J Pharmacol Toxicol 66, 246–256.

Chan, Y.-C., Ting, S., Lee, Y.-K., Ng, K.-M., Zhang, J., Chen, Z., Siu, C.-W., Oh, S.K.W., Tse, H.-F., 2013. Electrical stimulation promotes maturation of cardiomyocytes derived from human embryonic stem cells. J of Cardiovasc Trans Res 6, 989–999.

Chartrand, R., 2011. Numerical differentiation of noisy, nonsmooth data. ISRN Appl Math 2011, 1–11.

Chen, G., Gulbranson, D.R., Hou, Z., Bolin, J.M., Ruotti, V., Probasco, M.D., Smuga-Otto, K., Howden, S.E., Diol, N.R., Propson, N.E., Wagner, R., Lee, G.O., Antosiewicz-Bourget, J., Teng, J.M.C., Thomson, J.A., 2011. Chemically defined conditions for human iPSC derivation and culture. Nat Methods 8, 424–429.

Chen, Z., Xian, W., Bellin, M., Dorn, T., Tian, Q., Goedel, A., Dreizehnter, L., Schneider, C.M., Ward-van Oostwaard, D., Ng, J.K.M., Hinkel, R., Pane, L.S., Mummery, C.L., Lipp, P., Moretti, A., Laugwitz, K.-L., Sinnecker, D., 2017. Subtype-specific promoter-driven action potential imaging for precise disease modelling and drug testing in hiPSC-derived cardiomyocytes. Eur Heart J 38, 292–301.

Clements, M., Thomas, N., 2014. High-throughput multi-parameter profiling of electrophysiological drug effects in human embryonic stem cell derived cardiomyocytes using multi-electrode arrays. Toxicol Sci 140, 445–461.

Colatsky, T., Fermini, B., Gintant, G., Pierson, J.B., Sager, P., Sekino, Y., Strauss, D.G., Stockbridge, N., 2016. The comprehensive in vitro proarrhythmia Assay (CiPA)

initiative - update on progress. J Pharmacol Toxicol 81, 15–20.

Colatsky, T.J., 1982. Mechanisms of action of lidocaine and quinidine on action potential duration in rabbit cardiac Purkinje fibers. An effect on steady state sodium currents? Circ Res 50, 17–27.

Davies, D.L., Bouldin, D.W., 1979. A cluster separation measure. IEEE Trans Pattern Anal Mach Intell PAMI-1, 224–227.

de Diego, C., Pai, R.K., Chen, F., Xie, L.-H., De Leeuw, J., Weiss, J.N., Valderrábano, M., 2008. Electrophysiological consequences of acute regional ischemia/reperfusion in neonatal rat ventricular myocyte monolayers. Circulation 118, 2330–2337.

Dick, E., Rajamohan, D., Ronksley, J., Denning, C., 2010. Evaluating the utility of cardiomyocytes from human pluripotent stem cells for drug screening. Biochem Soc Trans 38, 1037–1045.

DiMasi, J.A., Hansen, R.W., Grabowski, H.G., 2003. The price of innovation: new estimates of drug development costs. J Health Econ.

Dimos, J.T., Rodolfa, K.T., Niakan, K.K., Weisenthal, L.M., Mitsumoto, H., Chung, W., Croft, G.F., Saphier, G., Leibel, R., Goland, R., Wichterle, H., Henderson, C.E., Eggan, K., 2008. Induced pluripotent stem cells generated from patients with ALS can be differentiated into motor neurons. Science 321, 1218–1221.

Ding, L., Splinter, R., Knisley, S.B., 2001. Quantifying spatial localization of optical mapping using Monte Carlo simulations. IEEE Trans Biomed Eng 48, 1098–1107.

Doss, M.X., Di Diego, J.M., Goodrow, R.J., Wu, Y., Cordeiro, J.M., Nesterenko, V.V., Barajas-Martínez, H., Hu, D., Urrutia, J., Desai, M., Treat, J.A., Sachinidis, A., Antzelevitch, C., 2012. Maximum diastolic potential of human induced pluripotent

stem cell-derived cardiomyocytes depends critically on I(Kr). PLoS ONE 7, e40288.

Du, D.T.M., Hellen, N., Kane, C., Terracciano, C.M.N., 2015. Action potential morphology of human induced pluripotent stem cell-derived cardiomyocytes does not predict cardiac chamber specificity and is dependent on cell density. Biophys J 108, 1–4.

Entcheva, E., Bien, H., 2006. Macroscopic optical mapping of excitation in cardiac cell networks with ultra-high spatiotemporal resolution. Prog Biophys Mol Biol 92, 232–257.

Fan, Y., Wu, J., Ashok, P., Hsiung, M., Tzanakakis, E.S., 2014. Production of human pluripotent stem cell therapeutics under defined xeno-free conditions: progress and challenges. Stem Cell Rev and Rep 11, 96–109.

Fast, V.G., 2005. Recording action potentials using voltage-sensitive dyes, in: Dhein, S., Mohr, F.W., Delmar, M. (Eds.), Practical Methods in Cardiovascular Research. Springer, Berlin, Heidelberg, pp. 233–255.

Fast, V.G., Kléber, A.G., 1997. Role of wavefront curvature in propagation of cardiac impulse. Cardiovasc Res.

Fu, J.-D., Rushing, S.N., Lieu, D.K., Chan, C.W., Kong, C.-W., Geng, L., Wilson, K.D., Chiamvimonvat, N., Boheler, K.R., Wu, J.C., Keller, G., Hajjar, R.J., Li, R.A., 2011. Distinct roles of microRNA-1 and -499 in ventricular specification and functional maturation of human embryonic stem cell-derived cardiomyocytes. PLoS ONE 6, e27417.

Fung, M., Thornton, A., Mybeck, K., Wu, J.H.H., Hornbuckle, K., Muniz, E., 2001. Evaluation of the characteristics of safety withdrawal of prescription drugs from

worldwide pharmaceutical markets-1960 to 1999. Ther Innov Regul Sci 35, 293–317.

Gaze, D.C., Collinson, P.O., 2005. Cardiac troponins as biomarkers of drug- and toxin-induced cardiac toxicity and cardioprotection. Expert Opin Drug Metab Toxicol 1, 715–725.

Giles, W.R., Noble, D., 2016. Rigorous phenotyping of cardiac iPSC preparations requires knowledge of their resting potential(s). Biophys J 110, 278–280.

Gintant, G., 2011. An evaluation of hERG current assay performance: Translating preclinical safety studies to clinical QT prolongation. Pharmacol Ther 129, 109–119.

Gintant, G.A., Su, Z., Martin, R.L., Cox, B.F., 2006. Utility of hERG assays as surrogate markers of delayed cardiac repolarization and QT safety. Toxicologic pathology.

Girouard, S., Laurita, K., Rosenbaum, D., 1996. Unique properties of cardiac action potentials recorded with voltage-sensitive dyes. J Cardiovasc Electrophysiol 7, 1024–1038.

Glukhov, A.V., Fedorov, V.V., Lou, Q., Ravikumar, V.K., Kalish, P.W., Schuessler, R.B., Moazami, N., Efimov, I.R., 2010. Transmural dispersion of repolarization in failing and nonfailing human ventricle. Circ Res 106, 981–991.

Gokhale, T.A., Kim, J.M., Kirkton, R.D., Bursac, N., Henriquez, C.S., 2017. Modeling an excitable biosynthetic tissue with inherent variability for paired computational-experimental studies. PLoS Comp Biol 13, e1005342.

Gorospe, G., Zhu, R., He, J.Q., Tung, L., Younes, L., Vidal, R., 2015. Efficient metamorphosis computation for classifying embryonic cardiac action potentials, in:. Presented at the Proceedings of the fifth international workshop on Mathematical Foundations of Computational Anatomy (MFCA 2015), p. 119.

Gorospe, G., Zhu, R., Millrod, M.A., Zambidis, E.T., Tung, L., Vidal, R., 2014. Automated grouping of action potentials of human embryonic stem cell-derived cardiomyocytes. IEEE Trans Biomed Eng 61, 2389–2395.

Guo, J., Zhang, X., Hu, Z., Zhuang, Z., Zhu, Z., Chen, Z., Chen, W., Zhao, Z., Zhang, C., Zhang, Z., 2012. A422T mutation in HERG potassium channel retained in ER is rescurable by pharmacologic or molecular chaperones. Biochem Biophys Res Commun 422, 305–310.

Halbach, M., Egert, U., Hescheler, J., Banach, K., 2003. Estimation of action potential changes from field potential recordings in multicellular mouse cardiac myocyte cultures. Cell Physiol Biochem 13, 271–284.

Hanton, G., 2014. Improvement of QT analysis for evaluating the proarrhythmic risk of drug: the importance of spatial and temporal dispersion of repolarization. J Clin Toxicol.

Harris, K., Aylott, M., Cui, Y., Louttit, J.B., McMahon, N.C., Sridhar, A., 2013. Comparison of electrophysiological data from human-induced pluripotent stem cell-derived cardiomyocytes to functional preclinical safety assays. Toxicol Sci 134, 412–426.

He, J.-Q., Ma, Y., Lee, Y., Thomson, J.A., Kamp, T.J., 2003. Human embryonic stem cells develop into multiple types of cardiac myocytes: action potential characterization. Circ Res 93, 32–39.

Hirt, M.N., Boeddinghaus, J., Mitchell, A., Schaaf, S., Börnchen, C., Müller, C., Schulz, H., Hubner, N., Stenzig, J., Stoehr, A., Neuber, C., Eder, A., Luther, P.K., Hansen, A., Eschenhagen, T., 2014. Functional improvement and maturation of rat and human

engineered heart tissue by chronic electrical stimulation. J Mol Cell Cardiol 74C, 151–161.

Honda, M., Kiyokawa, J., Tabo, M., Inoue, T., 2011. Electrophysiological characterization of cardiomyocytes derived from human induced pluripotent stem cells. J Pharmacol Sci 117, 149–159.

Hondeghem, L.M., Carlsson, L., Duker, G., 2001. Instability and triangulation of the action potential predict serious proarrhythmia, but action potential duration prolongation is antiarrhythmic. Circulation 103, 2004–2013.

Honerjäger, P., Loibl, E., Steidl, I., Schönsteiner, G., Ulm, K., 1986. Negative inotropic effects of tetrodotoxin and seven class 1 antiarrhythmic drugs in relation to sodium channel blockade. Naunyn Schmiedebergs Arch Pharmacol 332, 184–195.

Hortigon-Vinagre, M.P., Zamora, V., Burton, F.L., Green, J., Gintant, G.A., Smith, G.L., 2016. The use of ratiometric fluorescence measurements of the voltage sensitive dye Di-4-ANEPPS to examine action potential characteristics and drug effects on human induced pluripotent stem cell-derived cardiomyocytes. Toxicol Sci 154, 320–331.

Itzhaki, I., Maizels, L., Huber, I., Zwi-Dantsis, L., Caspi, O., Winterstern, A., Feldman, O., Gepstein, A., Arbel, G., Hammerman, H., Boulos, M., Gepstein, L., 2011a. Modelling the long QT syndrome with induced pluripotent stem cells. Nature 471, 225–229.

Itzhaki, I., Rapoport, S., Huber, I., Mizrahi, I., Zwi-Dantsis, L., Arbel, G., Schiller, J., Gepstein, L., 2011b. Calcium handling in human induced pluripotent stem cell derived cardiomyocytes. PLoS ONE 6, e18037.

Jenkins, M.J., Farid, S.S., 2015. Human pluripotent stem cell-derived products: advances

towards robust, scalable and cost-effective manufacturing strategies. Biotechnol J 10, 83–95.

Johnstone, R.H., Chang, E.T.Y., Bardenet, R., de Boer, T.P., Gavaghan, D.J., Pathmanathan, P., Clayton, R.H., Mirams, G.R., 2016. Uncertainty and variability in models of the cardiac action potential: Can we build trustworthy models? J Mol Cell Cardiol 96, 49–62.

Jonsson, M.K.B., Duker, G., Tropp, C., Andersson, B., Sartipy, P., Vos, M.A., van Veen, T.A.B., 2010. Quantified proarrhythmic potential of selected human embryonic stem cell-derived cardiomyocytes. Stem Cell Res 4, 189–200.

Jonsson, M.K.B., Vos, M.A., Mirams, G.R., Duker, G., Sartipy, P., de Boer, T.P., van Veen, T.A.B., 2012. Application of human stem cell-derived cardiomyocytes in safety pharmacology requires caution beyond hERG. J Mol Cell Cardiol 52, 998–1008.

Kane, C., Du, D.T.M., Hellen, N., Terracciano, C.M., 2016. The fallacy of assigning chamber specificity to iPSC cardiac myocytes from action potential morphology. Biophys J 110, 281–283.

Kane, C., Terracciano, C.M.N., 2017. Concise Review: Criteria for Chamber-Specific Categorization of Human Cardiac Myocytes Derived from Pluripotent Stem Cells. Stem Cells 35, 1881–1897.

Kang, C., Qiao, Y., Li, G., Baechle, K., Camelliti, P., Rentschler, S., Efimov, I.R., 2016. Human Organotypic Cultured Cardiac Slices: New Platform For High Throughput Preclinical Human Trials. Sci Rep 6, 28798.

Kang, J., Wang, L., Chen, X.-L., Triggle, D.J., Rampe, D., 2001. Interactions of a series

of fluoroquinolone antibacterial drugs with the human cardiac K+ channel HERG. Mol Pharmacol 59, 122–126.

Karakikes, I., Senyei, G.D., Hansen, J., Kong, C.-W., Azeloglu, E.U., Stillitano, F., Lieu, D.K., Wang, J., Ren, L., Hulot, J.-S., Iyengar, R., Li, R.A., Hajjar, R.J., 2014. Small molecule-mediated directed differentiation of human embryonic stem cells toward ventricular cardiomyocytes. Stem Cells Transl Med 3, 18–31.

Kehat, I., Gepstein, A., Spira, A., Itskovitz-Eldor, J., Gepstein, L., 2002. High-resolution electrophysiological assessment of human embryonic stem cell-derived cardiomyocytes a novel in vitro model for the study of conduction. Circ Res 91, 659–661.

Kehat, I., Kenyagin-Karsenti, D., Snir, M., Segev, H., Amit, M., Gepstein, A., Livne, E., Binah, O., Itskovitz-Eldor, J., Gepstein, L., 2001. Human embryonic stem cells can differentiate into myocytes with structural and functional properties of cardiomyocytes. 108, 407–414.

Kettenhofen, R., Duenbostell, A., Grossmann, M., Bertram, B., Luerman, G., Rascher-Eggstein, G., Artmann, G., 2014. The newcomer is getting up and running: human iPS cell-derived cardiomyocyte implementation in multiple cardiac safety assessment assays, in:. Presented at the Safety Pharmacology Society, Washington, DC.

Kim, C., Majdi, M., Xia, P., Wei, K.A., Talantova, M., Spiering, S., Nelson, B., Mercola, M., Chen, H.-S.V., 2010a. Non-cardiomyocytes influence the electrophysiological maturation of human embryonic stem cell-derived cardiomyocytes during differentiation. Stem Cells Dev 19, 783–795.

Kim, C., Wong, J., Wen, J., Wang, S., Wang, C., Spiering, S., Kan, N.G., Forcales, S.,

Puri, P.L., Leone, T.C., Marine, J.E., Calkins, H., Kelly, D.P., Judge, D.P., Chen, H.-S.V., 2013. Studying arrhythmogenic right ventricular dysplasia with patient-specific iPSCs. Nature 494, 105–110.

Kim, J.A., Lopes, C.M., Moss, A.J., McNitt, S., Barsheshet, A., Robinson, J.L., Zareba, W., Ackerman, M.J., Kaufman, E.S., Towbin, J.A., Vincent, M., Goldenberg, I., 2010b. Trigger-specific risk factors and response to therapy in long QT syndrome type 2. Heart Rhythm 7, 1797–1805.

Kim, J.J., Yang, L., Lin, B., Zhu, X., Sun, B., Kaplan, A.D., Bett, G.C.L., Rasmusson, R.L., London, B., Salama, G., 2015. Mechanism of automaticity in cardiomyocytes derived from human induced pluripotent stem cells. J Mol Cell Cardiol 81, 81–93.

Kléber, A.G., Rudy, Y., 2004. Basic mechanisms of cardiac impulse propagation and associated arrhythmias. Physiol Rev 84, 431–488.

Lahti, A.L., Kujala, V.J., Chapman, H., Koivisto, A.P., Pekkanen-Mattila, M., Kerkela, E., Hyttinen, J., Kontula, K., Swan, H., Conklin, B.R., Yamanaka, S., Silvennoinen, O., Aalto-Setala, K., 2012. Model for long QT syndrome type 2 using human iPS cells demonstrates arrhythmogenic characteristics in cell culture. Dis Model Mech 5, 220–230.

Lan, F., Lee, A.S., Liang, P., Sanchez-Freire, V., Nguyen, P.K., Wang, L., Han, L., Yen, M., Wang, Y., Sun, N., Abilez, O.J., Hu, S., Ebert, A.D., Navarrete, E.G., Simmons, C.S., Wheeler, M., Pruitt, B., Lewis, R., Yamaguchi, Y., Ashley, E.A., Bers, D.M., Robbins, R.C., Longaker, M.T., Wu, J.C., 2013. Abnormal calcium handling properties underlie familial hypertrophic cardiomyopathy pathology in patient-specific induced pluripotent stem cells. Cell Stem Cell 12, 101–113.

Lee, Y.-K., Ng, K.-M., Lai, W.-H., Chan, Y.-C., Lau, Y.-M., Lian, Q., Tse, H.-F., Siu, C.-W., 2011. Calcium homeostasis in human induced pluripotent stem cell-derived cardiomyocytes. Stem Cell Rev 7, 976–986.

Lengyel, C., Iost, N., Virag, L., Varró, A., Lathrop, D.A., Papp, J.G., 2001. Pharmacological block of the slow component of the outward delayed rectifier current (IKs) fails to lengthen rabbit ventricular muscle QTc and action potential duration. Br J Pharmacol 132, 101–110.

Leyton-Mange, J.S., Mills, R.W., Macri, V.S., Jang, M.Y., Butte, F.N., Ellinor, P.T., Milan, D.J., 2014. Rapid cellular phenotyping of human pluripotent stem cell-derived cardiomyocytes using a genetically encoded fluorescent voltage sensor. Stem Cell Reports 2, 163–170.

Lian, X., Hsiao, C., Wilson, G., Zhu, K., Hazeltine, L.B., Azarin, S.M., Raval, K.K., Zhang, J., Kamp, T.J., Palecek, S.P., 2012. Robust cardiomyocyte differentiation from human pluripotent stem cells via temporal modulation of canonical Wnt signaling. Proc Natl Acad Sci 109, E1848–E1857.

Lieu, D.K., Fu, J.-D., Chiamvimonvat, N., Tung, K.C., McNerney, G.P., Huser, T., Keller, G., Kong, C.-W., Li, R.A., 2013. Mechanism-based facilitated maturation of human pluripotent stem cell-derived cardiomyocytes. Circ Arrhythm Electrophysiol 6, 191–201.

Lim, Z.Y., Maskara, B., Aguel, F., Emokpae, R., Tung, L., 2006. Spiral wave attachment to millimeter-sized obstacles. Circulation 114, 2113–2121.

Little, M.A., Jones, N.S., 2010. Sparse Bayesian step-filtering for high-throughput analysis of molecular machine dynamics. Proc IEEE Int Conf Acoust Speech Signal

Process.

Liu, J., Laksman, Z., Backx, P.H., 2016. The electrophysiological development of cardiomyocytes. Adv Drug Deliv Rev.

López-Redondo, F., Kurokawa, J., Nomura, F., Kaneko, T., Hamada, T., Furukawa, T., Yasuda, K., 2016. A distribution analysis of action potential parameters obtained from patch-clamped human stem cell-derived cardiomyocytes. J Pharmacol Sci 1–5.

Lu, H.R., Hortigon-Vinagre, M.P., Zamora, V., Kopljar, I., De Bondt, A., Gallacher, D.J., Smith, G., 2017. Application of optical action potentials in human induced pluripotent stem cells-derived cardiomyocytes to predict drug-induced cardiac arrhythmias. J Pharmacol Toxicol.

Lundy, S.D., Zhu, W.-Z., Regnier, M., Laflamme, M.A., 2013. Structural and functional maturation of cardiomyocytes derived from human pluripotent stem cells. Stem Cells Dev 22, 1991–2002.

Ma, J., Guo, L., Fiene, S.J., Anson, B.D., Thomson, J.A., Kamp, T.J., Kolaja, K.L., Swanson, B.J., January, C.T., 2011. High purity human-induced pluripotent stem cell-derived cardiomyocytes: electrophysiological properties of action potentials and ionic currents. Am J Physiol Heart Circ Physiol 301, H2006–H2017.

Malik, N., Rao, M.S., 2013. A review of the methods for human iPSC derivation. Methods Mol Biol 997, 23–33.

Mathur, A., Loskill, P., Shao, K., Huebsch, N., Hong, S., Marcus, S.G., Marks, N., Mandegar, M., Conklin, B.R., Lee, L.P., Healy, K.E., 2015. Human iPSC-based cardiac microphysiological system for drug screening applications. Sci Rep 5, 8883.

Matsa, E., Burridge, P.W., Wu, J.C., 2014. Human stem cells for modeling heart disease

and for drug discovery. Sci Transl Med 6, 239ps6–239ps6.

Matsa, E., Rajamohan, D., Dick, E., Young, L., Mellor, I., Staniforth, A., Denning, C., 2011. Drug evaluation in cardiomyocytes derived from human induced pluripotent stem cells carrying a long QT syndrome type 2 mutation. Eur Heart J 32, 952–962.

McDonald, T.F., Pelzer, S., Trautwein, W., Pelzer, D.J., 1994. Regulation and modulation of calcium channels in cardiac, skeletal, and smooth muscle cells. Physiol Rev 74, 365–507.

Mehta, A., Ramachandra, C.J.A., Sequiera, G.L., Sudibyo, Y., Nandihalli, M., Yong, P.J.A., Koh, C.H., Shim, W., 2014a. Phasic modulation of wnt signaling enhances cardiac differentiation in human pluripotent stem cells by recapitulating developmental ontogeny. Biochimica et biophysica acta.

Mehta, A., Sequiera, G.L., Ramachandra, C.J.A., Sudibyo, Y., Chung, Y., Sheng, J., Wong, K.Y., Tan, T.H., Wong, P., Liew, R., Shim, W., 2014b. Re-trafficking of hERG reverses long QT syndrome 2 phenotype in human iPS-derived cardiomyocytes. Cardiovasc Res 102, 497–506.

Mitcheson, J.S., Perry, M.D., 2003. Molecular determinants of high-affinity drug binding to HERG channels. Current opinion in drug discovery & ….

Mohr, J.C., Zhang, J., Azarin, S.M., Soerens, A.G., de Pablo, J.J., Thomson, J.A., Lyons, G.E., Palecek, S.P., Kamp, T.J., 2010. The microwell control of embryoid body size in order to regulate cardiac differentiation of human embryonic stem cells. Biomaterials 31, 1885–1893.

Moore, J.C., Tsang, S.-Y., Rushing, S.N., Lin, D., Tse, H.-F., Chan, C.W.Y., Li, R.A., 2008. Functional consequences of overexpressing the gap junction Cx43 in the

cardiogenic potential of pluripotent human embryonic stem cells. Biochem Biophys Res Commun 377, 46–51.

Moretti, A., Bellin, M., Welling, A., Jung, C.B., Lam, J.T., Bott-Flügel, L., Dorn, T., Goedel, A., Höhnke, C., Hofmann, F., Seyfarth, M., Sinnecker, D., Schömig, A., Laugwitz, K.-L., 2010. Patient-specific induced pluripotent stem-cell models for long-QT syndrome. N Engl J Med 363, 1397–1409.

Mummery, C., Ward-van Oostwaard, D., Doevendans, P., Spijker, R., van den Brink, S., Hassink, R., van der Heyden, M., Opthof, T., Pera, M., la Riviere, de, A.B., Passier, R., Tertoolen, L., 2003. Differentiation of human embryonic stem cells to cardiomyocytes: role of coculture with visceral endoderm-like cells. Circulation 107, 2733–2740.

Mummery, C.L., Ward, D., Passier, R., 2007. Differentiation of human embryonic stem cells to cardiomyocytes by coculture with endoderm in serum-free medium. John Wiley & Sons, Inc., Hoboken, NJ, USA.

Mummery, C.L., Zhang, J., Ng, E.S., Elliott, D.A., Elefanty, A.G., Kamp, T.J., 2012. Differentiation of human embryonic stem cells and induced pluripotent stem cells to cardiomyocytes: a methods overview. Circ Res 111, 344–358.

Nenov, N.I., Crumb, W.J., Pigott, J.D., Harrison, L.H., Clarkson, C.W., 1998. Quinidine interactions with human atrial potassium channels. Circ Res 83, 1224–1231.

Nichols, C.G., Ripoll, C., Lederer, W.J., 1991. ATP-sensitive potassium channel modulation of the guinea pig ventricular action potential and contraction. Circ Res.

Novak, A., Barad, L., Zeevi-Levin, N., Shick, R., Shtrichman, R., Lorber, A., Itskovitz-Eldor, J., Binah, O., 2012. Cardiomyocytes generated from CPVTD307H patients are

arrhythmogenic in response to β-adrenergic stimulation. J Cell Mol Med 16, 468–482.

Nozaki, Y., Honda, Y., Tsujimoto, S., Watanabe, H., Kunimatsu, T., Funabashi, H., 2014. Availability of human induced pluripotent stem cell-derived cardiomyocytes in assessment of drug potential for QT prolongation. Toxicol Appl Pharmacol 278, 72–77.

Otsuji, T.G., Minami, I., Kurose, Y., Yamauchi, K., Tada, M., Nakatsuji, N., 2010. Progressive maturation in contracting cardiomyocytes derived from human embryonic stem cells: Qualitative effects on electrophysiological responses to drugs. Stem Cell Res 4, 201–213.

Paci, M., Hyttinen, J., Aalto-Setälä, K., Severi, S., 2013. Computational models of ventricular- and atrial-Like human induced pluripotent stem cell derived cardiomyocytes. Ann Biomed Eng.

Paci, M., Hyttinen, J., Rodriguez, B., Severi, S., 2015. Human induced pluripotent stem cell-derived versus adult cardiomyocytes: an in silico electrophysiological study on effects of ionic current block. Br J Pharmacol 172, 5147–5160.

Paci, M., Passini, E., Severi, S., Hyttinen, J., 2016. A population of in silico models to face the variability of human induced pluripotent stem cell-derived cardiomyocytes: The hERG block case study. Comput Cardiol.

Page, G., Ratchada, P., Miron, Y., Steiner, G., Ghetti, A., Miller, P.E., Reynolds, J.A., Wang, K., Greiter-Wilke, A., Polonchuk, L., Traebert, M., Gintant, G.A., Abi-Gerges, N., 2016. Human ex-vivo action potential model for pro-arrhythmia risk assessment. J Pharmacol Toxicol 81, 183–195.

Peeters, G.A., Sanguinetti, M.C., Eki, Y., Konarzewska, H., Renlund, D.G., Karwande, S.V., Barry, W.H., 1995. Method for isolation of human ventricular myocytes from single endocardial and epicardial biopsies. Am J Physiol 268, H1757–64.

Peng, S., Lacerda, A.E., Kirsch, G.E., Brown, A.M., Bruening-Wright, A., 2010. The action potential and comparative pharmacology of stem cell-derived human cardiomyocytes. J Pharmacol Toxicol 61, 277–286.

Peters, M.F., Lamore, S.D., Guo, L., Scott, C.W., Kolaja, K.L., 2015. Human stem cell-derived cardiomyocytes in cellular impedance assays: bringing cardiotoxicity screening to the front line. Cardiovasc Toxicol 15, 127–139.

Piccini, I., Rao, J., Seebohm, G., Greber, B., 2015. Human pluripotent stem cell-derived cardiomyocytes: Genome-wide expression profiling of long-term in vitro maturation in comparison to human heart tissue. Genom Data 4, 69–72.

Piccini, J.P., Whellan, D.J., Berridge, B.R., Finkle, J.K., Pettit, S.D., Stockbridge, N., Valentin, J.-P., Vargas, H.M., Krucoff, M.W., CSRC/HESI Writing Group, 2009. Current challenges in the evaluation of cardiac safety during drug development: translational medicine meets the Critical Path Initiative. Am Heart J 158, 317–326.

Pitts, K.R., Toombs, C.F., 2004. Coverslip hypoxia: a novel method for studying cardiac myocyte hypoxia and ischemia in vitro. Am J Physiol Heart Circ Physiol 287, H1801–H1812.

Poon, E., Yan, B., Zhang, S., Rushing, S., Keung, W., Ren, L., Lieu, D.K., Geng, L., Kong, C.-W., Wang, J., Wong, H.S., Boheler, K.R., Li, R.A., 2013. Transcriptome-guided functional analyses reveal novel biological properties and regulatory hierarchy of human embryonic stem cell-derived ventricular cardiomyocytes crucial

for maturation. PLoS ONE 8, e77784.

Priest, B.T., Bell, I.M., Garcia, M.L., 2008. Role of hERG potassium channel assays in drug development. Channels (Austin) 2, 87–93.

Quan, W., Rudy, Y., 1990. Unidirectional block and reentry of cardiac excitation: a model study. Circ Res 66, 367–382.

Redfern, W.S., Carlsson, L., Davis, A.S., Lynch, W.G., MacKenzie, I., Palethorpe, S., Siegl, P.K.S., Strang, I., Sullivan, A.T., Wallis, R., Camm, A.J., Hammond, T.G., 2003. Relationships between preclinical cardiac electrophysiology, clinical QT interval prolongation and torsade de pointes for a broad range of drugs: evidence for a provisional safety margin in drug development. Cardiovasc Res 58, 32–45.

Robertson, C., Tran, D.D., George, S.C., 2013. Concise review: maturation phases of human pluripotent stem cell-derived cardiomyocytes. Stem Cells 31, 829–837.

Romero, L., Pueyo, E., Fink, M., Rodriguez, B., 2009. Impact of ionic current variability on human ventricular cellular electrophysiology. Am J Physiol Heart Circ Physiol 297, H1436–H1445.

Ruan, Y., Liu, N., Napolitano, C., Priori, S.G., 2008. Therapeutic strategies for long-QT syndrome. Circ Arrhythm Electrophysiol 1, 290–297.

Sarkar, A.X., Christini, D.J., Sobie, E.A., 2012. Exploiting mathematical models to illuminate electrophysiological variability between individuals. J Physiol (Lond) 590, 2555–2567.

Sarkar, A.X., Sobie, E.A., 2011. Quantification of repolarization reserve to understand interpatient variability in the response to proarrhythmic drugs: A computational analysis. HRTHM 8, 1749–1755.

Shah, M., Akar, F.G., Tomaselli, G.F., 2005. Molecular basis of arrhythmias. Circulation 112, 2517–2529.

Shaheen, N., Shiti, A., Gepstein, L., 2017. Pluripotent stem cell-based platforms in cardiac disease modeling and drug testing. Clin Pharmacol Ther 102, 203–208.

Shamblott, M.J., Axelman, J., Wang, S., Bugg, E.M., Littlefield, J.W., Donovan, P.J., Blumenthal, P.D., Huggins, G.R., Gearhart, J.D., 1998. Derivation of pluripotent stem cells from cultured human primordial germ cells. Proc Natl Acad Sci 95, 13726–13731.

Sharma, D., Glatter, K.A., Timofeyev, V., Tuteja, D., Zhang, Z., Rodriguez, J., Tester, D.J., Low, R., Scheinman, M.M., Ackerman, M.J., Chiamvimonvat, N., 2004. Characterization of a KCNQ1/KVLQT1 polymorphism in Asian families with LQT2: implications for genetic testing. J Mol Cell Cardiol 37, 79–89.

Sigg, D.C., Iaizzo, P.A., Xiao, Y.F., He, B., 2010. Cardiac electrophysiology methods and models. Springer.

Sinnecker, D., Laugwitz, K.-L., Moretti, A., 2014. Induced pluripotent stem cell-derived cardiomyocytes for drug development and toxicity testing. Pharmacol Ther 143, 246–252.

Slawsky, M.T., Castle, N.A., 1994. K+ channel blocking actions of flecainide compared with those of propafenone and quinidine in adult rat ventricular myocytes. J Pharmacol Exp Ther 269, 66–74.

Smith, J.L., Anderson, C.L., Burgess, D.E., Elayi, C.S., January, C.T., Delisle, B.P., 2016. Molecular pathogenesis of long QT syndrome type 2. J Arrhythm 32, 373–380.

Spector, P.S., Curran, M.E., Keating, M.T., 1996. Class III antiarrhythmic drugs block

HERG, a human cardiac delayed rectifier K+ channel. Circulation.

Spencer, C.I., Baba, S., Nakamura, K., Hua, E.A., Sears, M.A.F., Fu, C.-C., Zhang, J., Balijepalli, S., Tomoda, K., Hayashi, Y., Lizarraga, P., Wojciak, J., Scheinman, M.M., Aalto-Setälä, K., Makielski, J.C., January, C.T., Healy, K.E., Kamp, T.J., Yamanaka, S., Conklin, B.R., 2014. Calcium transients closely reflect prolonged action potentials in iPSC models of inherited cardiac arrhythmia. Stem Cell Reports 3, 269–281.

Splawski, I., Shen, J., Timothy, K.W., Lehmann, M.H., Priori, S., Robinson, J.L., Moss, A.J., Schwartz, P.J., Towbin, J.A., Vincent, G.M., Keating, M.T., 2000. Spectrum of mutations in long-QT syndrome genes. KVLQT1, HERG, SCN5A, KCNE1, and KCNE2. Circulation 102, 1178–1185.

Sun, N., Yazawa, M., Liu, J., Han, L., Sanchez-Freire, V., Abilez, O.J., Navarrete, E.G., Hu, S., Wang, L., Lee, A., Pavlovic, A., Lin, S., Chen, R., Hajjar, R.J., Snyder, M.P., Dolmetsch, R.E., Butte, M.J., Ashley, E.A., Longaker, M.T., Robbins, R.C., Wu, J.C., 2012. Patient-specific induced pluripotent stem cells as a model for familial dilated cardiomyopathy. Sci Transl Med 4, 130ra47.

Taglialatela, M., 2003. Heterologous expression systems and screening technologies in ion channel drug discovery, in: Pugsley, M.K. (Ed.), Cardiac Drug Development Guide. Cardiac Drug Development Guide.

Takahashi, K., Tanabe, K., Ohnuki, M., Narita, M., Ichisaka, T., Tomoda, K., Yamanaka, S., 2007. Induction of pluripotent stem cells from adult human fibroblasts by defined factors. Cell 131, 861–872.

Tanaka, T., Tohyama, S., Murata, M., Chen, H., Hattori, F., Egashira, T., Seki, T., Ohno,

Y., Koshimizu, U., Yuasa, S., Ogawa, S., Yamanaka, S., Fukuda, K., 2009. In vitro pharmacologic testing using human induced pluripotent stem cell-derived cardiomyocytes. Biochem Biophys Res Commun 385, 497–502.

Tertoolen, L.G.J., Braam, S.R., van Meer, B.J., Passier, R., Mummery, C.L., 2017. Interpretation of field potentials measured on a multi electrode array in pharmacological toxicity screening on primary and human pluripotent stem cell-derived cardiomyocytes. Biochem Biophys Res Commun.

Tester, D.J., Ackerman, M.J., 2014. Genetics of long QT syndrome. Methodist Debakey Cardiovasc J 10, 29–33.

Thomson, J.A., Itskovitz-Eldor, J., Shapiro, S.S., Waknitz, M.A., Swiergiel, J.J., Marshall, V.S., Jones, J.M., 1998. Embryonic stem cell lines derived from human blastocysts. Science 282, 1145–1147.

Tohyama, S., Hattori, F., Sano, M., Hishiki, T., Nagahata, Y., Matsuura, T., Hashimoto, H., Suzuki, T., Yamashita, H., Satoh, Y., Egashira, T., Seki, T., Muraoka, N., Yamakawa, H., Ohgino, Y., Tanaka, T., Yoichi, M., Yuasa, S., Murata, M., Suematsu, M., Fukuda, K., 2013. Distinct metabolic flow enables large-scale purification of mouse and human pluripotent stem cell-derived cardiomyocytes. Cell Stem Cell 12, 127–137.

Towart, R., Linders, J.T.M., Hermans, A.N., Rohrbacher, J., van der Linde, H.J., Ercken, M., Cik, M., Roevens, P., Teisman, A., Gallacher, D.J., 2009. Blockade of the I(Ks) potassium channel: an overlooked cardiovascular liability in drug safety screening? J Pharmacol Toxicol 60, 1–10.

Trautwein, W., Kassebaum, D.G., Nelson, R.M., Hecht, H.H., 1962. Electrophysiological

study of human heart muscle. Circ Res 10, 306–312.

Tritthart, H.A., 2005. Optical techniques for the recording of action potentials, in: Dhein, S., Mohr, F.W., Delmar, M. (Eds.), Practical Methods in Cardiovascular Research. Springer, Berlin, Heidelberg, pp. 215–232.

van den Heuvel, N.H.L., van Veen, T.A.B., Lim, B., Jonsson, M.K.B., 2014. Lessons from the heart: mirroring electrophysiological characteristics during cardiac development to in vitro differentiation of stem cell derived cardiomyocytes. J Mol Cell Cardiol 67, 12–25.

van der Linde, D., Konings, E.E.M., Slager, M.A., Witsenburg, M., Helbing, W.A., Takkenberg, J.J.M., Roos-Hesselink, J.W., 2011. Birth prevalence of congenital heart disease worldwide. J Am Coll Cardiol 58, 2241–2247.

van Rijen, H.V.M., van Veen, T.A.B., Gros, D., Wilders, R., de Bakker, J.M.T., 2006. Connexins and cardiac arrhythmias. Adv Cardiol 42, 150–160.

Verlinsky, Y., Strelchenko, N., Kukharenko, V., Rechitsky, S., Verlinsky, O., Galat, V., Kuliev, A., 2005. Human embryonic stem cell lines with genetic disorders. Reprod Biomed Online 10, 105–110.

Vicente, J., Johannesen, L., Mason, J.W., Crumb, W.J., Pueyo, E., Stockbridge, N., Strauss, D.G., 2015. Comprehensive T wave morphology assessment in a randomized clinical study of dofetilide, quinidine, ranolazine, and verapamil. J Am Heart Assoc 4.

Vigmond, E.J., Hughes, M., Plank, G., Leon, L.J., 2003. Computational tools for modeling electrical activity in cardiac tissue. J Electrocardiol 36, 69–74.

Vigmond, E.J., Weber dos Santos, R., Prassl, A.J., Deo, M., Plank, G., 2008. Solvers for

the cardiac bidomain equations. Prog Biophys Mol Biol 96, 3–18.

Wang, K., Terrenoire, C., Sampson, K.J., Iyer, V., Osteen, J.D., Lu, J., Keller, G., Kotton, D.N., Kass, R.S., 2011. Biophysical properties of slow potassium channels in human embryonic stem cell derived cardiomyocytes implicate subunit stoichiometry. J Physiol (Lond) 589, 6093–6104.

Wang, Y., Li, Z.C., Zhang, P., Poon, E., Kong, C.W., Boheler, K.R., Huang, Y., Li, R.A., Yao, X., 2015. Nitric oxide-cGMP-PKG pathway acts on Orai1 to inhibit the hypertrophy of human embryonic stem cell-derived cardiomyocytes. Stem Cells 33, 2973–2984.

Werley, C.A., Chien, M.-P., Gaublomme, J., Shekhar, K., Butty, V., Yi, B.A., Kralj, J.M., Bloxham, W., Boyer, L.A., Regev, A., Cohen, A.E., 2017. Geometry-dependent functional changes in iPSC-derived cardiomyocytes probed by functional imaging and RNA sequencing. PLoS ONE 12, e0172671.

Wettwer, E., Scholtysik, G., Schaad, A., Himmel, H., Ravens, U., 1991. Effects of the new class III antiarrhythmic drug E-4031 on myocardial contractility and electrophysiological parameters. J Cardiovasc Pharmacol 17, 480–487.

Yamamoto, Y., Makiyama, T., Harita, T., Sasaki, K., Wuriyanghai, Y., Hayano, M., Nishiuchi, S., Kohjitani, H., Hirose, S., Chen, J., Yokoi, F., Ishikawa, T., Ohno, S., Chonabayashi, K., Motomura, H., Yoshida, Y., Horie, M., Makita, N., Kimura, T., 2017. Allele-specific ablation rescues electrophysiological abnormalities in a human iPS cell model of long-QT syndrome with a CALM2 mutation. Hum Mol Gen 26, 1670–1677.

Yang, C., Aama, Al, J., Stojkovic, M., Keavney, B., Trafford, A., Lako, M., Armstrong,

L., 2015. Concise review: cardiac disease modeling using induced pluripotent stem cells. Stem Cells 33, 2643–2651.

Yang, X., Pabon, L., Murry, C.E., 2014. Engineering adolescence: maturation of human pluripotent stem cell-derived cardiomyocytes. Circ Res 114, 511–523.

Zhang, H., Zou, B., Yu, H., Moretti, A., Wang, X., Yan, W., Babcock, J.J., Bellin, M., McManus, O.B., Tomaselli, G., Nan, F., Laugwitz, K.-L., Li, M., 2012. Modulation of hERG potassium channel gating normalizes action potential duration prolonged by dysfunctional KCNQ1 potassium channel. Proc Natl Acad Sci 109, 11866–11871.

Zhang, J., Wilson, G.F., Soerens, A.G., Koonce, C.H., Yu, J., Palecek, S.P., Thomson, J.A., Kamp, T.J., 2009. Functional cardiomyocytes derived from human induced pluripotent stem cells. Circ Res 104, e30–e41.

Zhang, Q., Jiang, J., Han, P., Yuan, Q., Zhang, J., Zhang, X., Xu, Y., Cao, H., Meng, Q., Chen, L., Tian, T., Wang, X., Li, P., Hescheler, J., Ji, G., Ma, Y., 2011. Direct differentiation of atrial and ventricular myocytes from human embryonic stem cells by alternating retinoid signals. Cell Res 21, 579–587.

Zhu, R., Blazeski, A., Poon, E., Costa, K.D., Tung, L., Boheler, K.R., 2014. Physical developmental cues for the maturation of human pluripotent stem cell-derived cardiomyocytes. Stem Cell Res Ther 5, 117.

Zhu, R., Millrod, M.A., Zambidis, E.T., Tung, L., 2016. Variability of action potentials within and among cardiac cell clusters derived from human embryonic stem cells. Sci Rep 6, 18544.

Vita

Renjun Zhu

Born June 8, 1987 in Wuhan, Hubei, China

Education

The Johns Hopkins University, Baltimore, MD

- Ph.D. in Biomedical Engineering, 2017
- Dissertation title: “Syncytial model of human pluripotent stem cell-derived cardiomyocytes for electrophysiology studies”

Tsinghua University, Beijing, China

- Bachelor’s degree in Biomedical Engineering, 2009

Teaching experience

- Bioelectricity, The Jonhs Hopkins University, 2013
- Systems Bioengineering I, 2011

Publications

- Oh, Y, Cho, G-S, Li, Z, Hong, I, **Zhu, R**, Kim, M-J, et al. (2016). Functional Coupling with Cardiac Muscle Promotes Maturation of hPSC-Derived Sympathetic Neurons. Cell Stem Cell.

- **Zhu, R**, Millrod, MA, Zambidis, ET, & Tung, L (2016). Variability of Action Potentials Within and Among Cardiac Cell Clusters Derived from Human Embryonic Stem Cells. Scientific Reports, 6, 18544.

- **Zhu, R**, Blazeski, A, Poon, E, Costa, KD, Tung, L, & Boheler, KR (2014). Physical developmental cues for the maturation of human pluripotent stem cell-derived cardiomyocytes. Stem Cell Research, 5(5), 117.

- Gorospe, G, **Zhu, R**, Millrod, MA, Zambidis, ET, Tung, L, & Vidal, R (2014). Automated grouping of action potentials of human embryonic stem cell-derived cardiomyocytes. IEEE Transactions on Biomedical Engineering, 61(9), 2389–2395.

- Weinberg, SH, Chang, KC, **Zhu, R**, Tandri, H, Berger, RD, Trayanova, NA, & Tung, L (2013). Defibrillation success with high frequency electric fields is related to degree and location of conduction block. Heart Rhythm : the Official Journal of the Heart Rhythm Society, 10(5), 740–748.

- Blazeski, A, **Zhu, R**, Hunter, DW, Weinberg, SH, Zambidis, ET, & Tung, L (2012). Cardiomyocytes derived from human induced pluripotent stem cells as models for normal and diseased cardiac electrophysiology and contractility. Progress in Biophysics and Molecular Biology, 110(2-3), 166–177.

- Blazeski, A, **Zhu, R**, Hunter, DW, Weinberg, SH, Boheler, KR, Zambidis, ET, & Tung, L (2012). Electrophysiological and contractile function of cardiomyocytes derived from human embryonic stem cells. Progress in Biophysics and Molecular Biology, 110(2-3), 178–195.

- Lim, KM, Constantino, J, Gurev, V, **Zhu, R**, Shim, EB, & Trayanova, NA (2012). Comparison of the effects of continuous and pulsatile left ventricular-assist devices on ventricular unloading using a cardiac electromechanics model. The Journal of Physiological Sciences : JPS, 62(1), 11–19.

- Tandri, H, Weinberg, SH, Chang, KC, **Zhu, R**, Trayanova, NA, Tung, L, & Berger, RD (2011). Reversible Cardiac Conduction Block and Defibrillation with High-Frequency Electric Field. Science Translational Medicine, 3(102), 102ra96–102ra96.

Conference Proceedings

- **Zhu R**, Hariharan V, Tung L, Monolayer Cultures of Human iPSC-Derived Cardiomyocytes Promote Single Electrophysiological Phenotype. *Northeast Bioengineering Conference*. 2017

- **Zhu R**, Blazeski A, Boheler KR, Tung L, Heterogeneity of Action Potentials in a Human iPSC-Derived Cardiomyocyte Syncytial Model. Gordon Research Conference: Cardiac Arrhythmia Mechanisms. 2015

- Gorospe, G, **Zhu, R**, He, JQ, Tung, L, Younes, L, Vidal, R, 2015. Efficient metamorphosis computation for classifying embryonic cardiac action potentials, *The fifth international workshop on Mathematical Foundations of Computational Anatomy (MFCA 2015)*

- **Zhu R**, Joshi-Mukherjee R, Blazeski A, Boheler KR, Tomaselli GF, Tung L. Syncytial Model of Type 2 Long QT Syndrome Derived from Human iPS Cells can be Paced and Responds to I_{Kr} block and Activation. *AHA Scientific Sessions*. 2014.

- **Zhu R**, Blazeski A, Boheler KR, Tung L. Stable Human Induced Pluripotent Stem Cell- Derived Cardiomyocyte Syncytium that Supports Paced Electrical Activities and Responds to I_{Kr} Blockade. *Biomedical Engineering Society Annual Meeting*. 2014.

- **Zhu R**, Gorospe G, Millrod MA, Zambidis ET, Vidal R, Tung L. Variability and Automated Analysis of Action Potentials from Human Embryonic Stem Cell Derived Cardiac Cell Clusters. *Gordon Research Conference: Cardiac Arrhythmia Mechanisms*. 2013

- Gorospe G, **Zhu R**, Millrod MA, Zambidis ET, Tung L, Vidal R. Automated Analysis of Action Potentials from Cardiac Cell Clusters Derived from Human Embryonic Stem Cells. *AHA Scientific Sessions*. 2012.

- **Zhu R**, Millrod MA, Zambidis ET, Tung L. Variability of Action Potentials Within and Among Cardiac Cell Clusters Derived from Human Embryonic Stem Cells. *Biomedical Engineering Society Annual Meeting*. 2012.